# Parametric Analyses of Suspension Plasma Spraying Coating Buildup Using a Computationally Efficient Numerical Model

**Arindam Mor**

A Thesis in
the Department of
Mechanical, Industrial, and Aerospace Engineering

Presented in Partial Fulfilment of
the Requirements for the Degree of
Magisteriate in Applied Science
(Mechanical Engineering)

at Concordia University
Montreal, Quebec, CA

July 2025

CONCORDIA UNIVERSITY

SCHOOL OF GRADUATE STUDIES

This is to certify that this thesis prepared

By: **Arindam Mor**

Entitled: **Parametric Analyses of Suspension Plasma Spraying Coating Buildup Using a Computationally Efficient Numerical Model**

and submitted in partial fulfilment of the requirements for the degree of

Magisteriate in Applied Science (Mechanical Engineering)

complies with the regulations of the University and meets the accepted standards with respect to originality, and quality.

Signed by the final examining committee:

_____ Chair, & Examiner
Dr Moussa Tembely

_____ Examiner
Dr Marius Paraschivoiu

_____ External Examiner
Dr Pantcho P. Stoyanov

_____ Thesis Supervisor
Dr Marius Paraschivoiu

Approved by

_____
Dr Lyes Kadem, Graduate Program Director

July 24, 2025

_____
Dr Mourad Debbabi, Dean of Faculty

ABSTRACT

**Parametric Analyses of Suspension Plasma Spraying Coating Buildup Using a Computationally Efficient Numerical Model**

**Arindam Mor**

Suspension Plasma Spraying (SPS) has emerged as a promising coating technique for producing nano-structured, and fine-grained surfaces in the aerospace, and energy sectors. However, predicting the final coating morphology remains a challenge due to the complex interplay of parameters, such as particle velocity, temperature, injection configuration, substrate geometry, and plasma dynamics. Experiments have contributed valuable insights, but remain resource-intensive, time-consuming, and limited in scope.

This thesis presents a comprehensive numerical model, developed in MATLAB, for simulating coating buildup in SPS processes. The model is designed as a flexible computational tool to support researchers, and engineers in exploring process-structure relationships, and optimising spray parameters. It simulates particle motion, temperature-dependent flattening, spray gun motion, and surface evolution over time. The framework accommodates injection schemes, incorporates plasma jet fluctuations, and integrates a broader set of particle distribution datasets to enhance generalisation.

Compared to prior models, this work expands the design space by enabling simulations across multiple substrate geometries, and injection configurations. Model outputs include deposition coverage, and morphological growth trends that align with observed experimental behaviours, such as columnar structures, and shadowing effects. The model is used to analyse the effects of interpeak distances of asperities, particle velocity distributions, spray gun traverse velocities, and database representative times on the final coating microstructures, thus better informing users on the impact of parameters on microstructural features such as porosity, density, and column formation.

Overall, the simulation framework provides a cost-effective and scalable alternative to experimentation. It contributes to the digitalisation of SPS process development and lays the groundwork for future integration with data-driven optimisation techniques, CFD-based plasma torch simulations, and intelligent control strategies for optimisation.

ACKNOWLEDGEMENTS

I thank Professors (Dr) **Marius Paraschivoiu**, (Dr) **Moussa Tembely**, and (Dr) **Christian Moreau** for their unwavering support during my time at the university. I thank my PhD counterpart, **Ashkan Ghafari**, for providing requisite input data to complete this study. Also, I thank my MEng contemporary, **Gayathridevan Bindu**, for her valuable contributions during her short stint at the lab. I acknowledge the alumni, **Behrad Kashfi Ashtiani** and the late **Siavash Ghafouri Azar**, for their foundational work on the initial developments of this numerical model. Further, I thank **Concordia University**, Natural Sciences and Engineering Research Council of Canada (**NSERC**), and **Mitacs** for their financial support of my research endeavours.

I express my utmost gratitude to my father, Prof (Dr) **Dharam Pal Singh**; my mother, (Dr) **Ritu**; and my sister, **Arhana**, for standing by me through thick and thin, and supporting me through all my struggles. I also extend my thanks to my friends, **Sanket** and **Sachin**, for giving me valuable counsel on matters of love and life. Lastly, I thank **my 22-year-old self**, who took the plunge, landed in Montréal in the cold winter of December, and not just survived – but thrived!

Dedicated to

the **Mor**s, **Punia**s, **Chahal**s, and **Malik**s

of Hindustan –

I am because they were!

LIST OF CONTENTS

LIST OF FIGURES

LIST OF TABLES

# Chapter 1: **INTRODUCTION**

Today, Thermal Spray (TS) processes are becoming increasingly popular across the globe, primarily for their ability to enhance the surface characteristics of a substrate, for e.g. heat resistance, wear resistance, corrosion resistance, thermal insulation, and so forth. However, it is not always easy to get to these desired effects, given the sheer number of process parameters involved. Furthermore, powder characteristics, substrate preparation methods, and post-treatment techniques, among other things, also play a crucial role to ensure desired microstructure, coating adhesion, and overall performance.

TS processes, generally, involve the heating of the feedstock, followed by accelerating the molten (and semi-molten) particles towards the substrate, by means of injecting them into a high-velocity, high-temperature spray plume emitting from a spray gun. As the gun is constantly moving, due to the immediate drop in temperature, the particles solidify on the surface of the substrate and form a coating (Singh et al. 2025; Singh et al. 2019; Dorfman 2018). Fig. 1.1 illustrates a schematic diagram of the process (Singh et al. 2025).

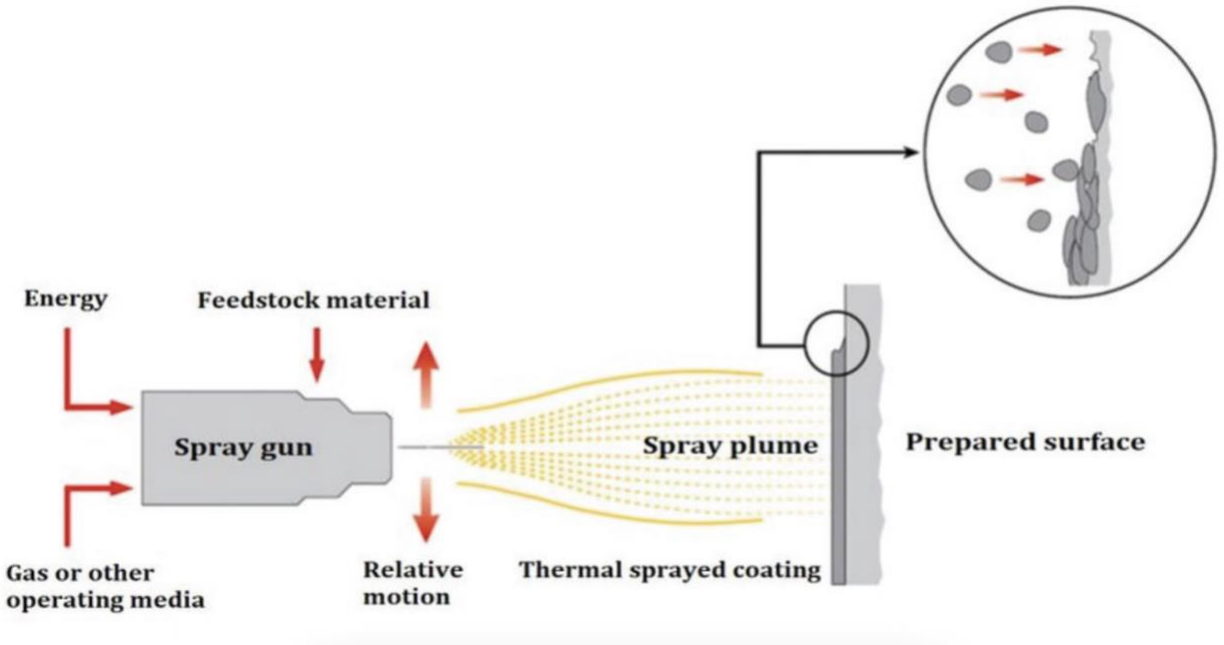


Fig. 1.1 Schema for a typical TS process

The overall setup of the process is critical to the coating properties. In this regard, a few pertinent parameters include the standoff distance, the number of passes, average velocity, and temperature of the nanoparticles, and injection gas statistics. Substrate preparation is, usually, the first step in any TS process. Methods to prepare any given substrate include surface cleaning, roughening, as well as preheating. Specific techniques include machining, grinding, surface refinement, and heat treatment (Singh et al. 2025; Hashmi et al. 2023; Narayanan et al. 2020). These steps are critical for they dictate the adhesion between the substrate, and the coating; and, thus, the latter's long-term performance in terms of mechanical, and metallurgical bonding (Singh et al. 2025; Jiang et al. 2023; Li et al. 2022; Song and Li 2022; Pathanatecha 2019).

As of 2025, TS coatings play an imperative role in key sectors, such as aerospace, automotive, energy, and manufacturing, not only for their thermo-mechanical properties, but also for their visual appeal. For example, bronze or brass are sprayed onto substrates to give them a decorative finish (Singh et al. 2025; Gilder-sleeve and Vaßen 2023; Tejero-Martin et al. 2019; Dorfman 2005). Among their other uses, TS coats are used extensively on turbine blades, and oil drills (Singh et al. 2025; Viswanathan et al. 2021).

## 1.1 Types of Thermal Spray Processes

As the use of thermal spray processes has grown, so have their types, each meeting unique sets of industrial needs. For instance, we now have Arc Spraying (AS), Flame Spraying (FS), High Velocity Oxygen Fuel Spraying (HVOF), Plasma Spraying (PS), and even Cold Spraying (CS). Each of the aforementioned procedures slightly vary from one-another, typically in terms of how they produce heat, or transfer the feedstock onto the substrate. Broadly, though, they work on the same principle, i.e. applying heat to melt the feedstock material, accelerating the molten, and semi-molten particles towards the substrate at high speeds, which then solidify to form a coating (Singh et al. 2025; Czupryński 2019; Elewa et al. 2019; Arboleda et al. 2018; Brossard 2010).

### *1.1.1 Arc Spraying*

As the term implies, AS employs an electric arc. Consumable wires create this arc, which, then, melts the particles of a given feedstock (Singh et al. 2025; Nurisna et al. 2022; Horner et al. 2015). Naturally, the parturitional wires are made up of the coating material. There's also a sacrificial lamb-wire that fulfils the greater good of being the bonding agent. The molten, and semi-molten particles atomise, and go with the flow alongside compressed air, thus forming a thick coating. This thickness, and the rapid deposition rates make AS popular, particularly for restoration purposes (Singh et al. 2025; DePalma et al. 2022; Alkathafi and Younis 2021; Kant et al. 2020; Fauchais and Vardelle 2007; Gedzevicius and Valiulis 2006). Fig. 1.2 illustrates a schematic diagram of the process (Boulos et al. 2021).

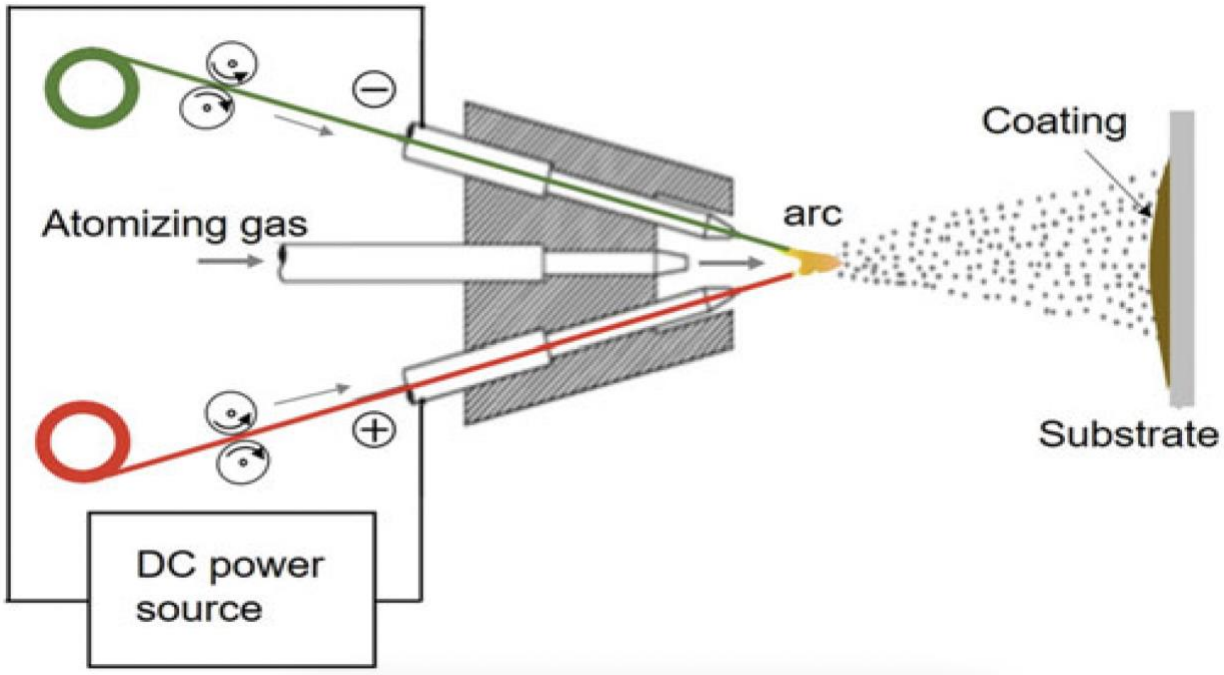


Fig. 1.2 Schema for a typical AS process

### *1.1.2 Flame Spraying*

As the name suggests, FS involves a flame, which is engendered by burning propane or acetylene in air. Either compressed air or some inert gas is used to deliver the molten or semi-molten particles from the feedstock to the surface of the substrate. Upon impact, the particles deform, and compress, thus causing the formation of a coating (Singh et al. 2025; Czupryński 2019; Arboleda et al. 2018; Kumar and Kumar 2018; Hardwicke and Lau 2013). FS is widely acknowledged for its adaptability, given how many different materials it can be used with. Hence, it can be used in disparate applications. Provided that it burns fuel gasses for the mighty flame, it's not very sustainable (Singh et al. 2025; Panchal and Amin 2016; Bensebaa 2013; Voisey 2010; Rodriguez et al. 2007). Fig. 1.3 offers a schema of the process (Courtesy of Oerlikon-Metco).

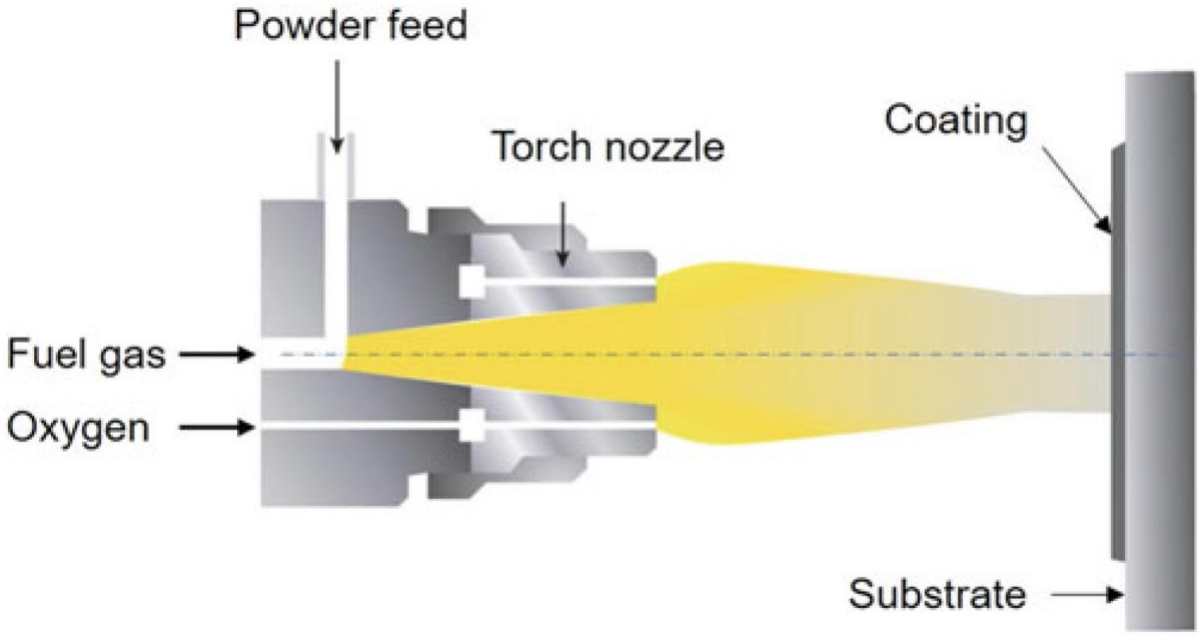


Fig. 1.3 Schema for a typical FS process

### *1.1.3 High Velocity Oxygen Fuel Spraying*

HVOF uses the pumping of streams of fuel, and oxygen into a combustion chamber with a concomitant injection of feedstock material, usually in powder form (Singh et al. 2025; Zhao et al. 2023; Tillmann et al. 2008). The gases accelerate the particles at very high speeds as they are deposited onto the substrate. The velocities are such that as the gases exit the nozzle, they form a supersonic gas jet (Singh et al. 2025; Hu et al. 2023; Lal and Sampath 2023). The high kinetic energy calls for remarkable coatings with very good adhesion. HVOF coatings are characterised by their thickness, low levels of porosity, exceptional metallurgical properties, and resistance against corrosion, and wear (Singh et al. 2025; Babu et al. 2023; Yang et al. 2022; Fu et al. 2020; Li et al. 2017). Fig. 1.4 depicts a schematic representation (Courtesy of Oerlikon-Metco). Fig. 1.4(a) shows axial injection of the powder into a water-cooled pressurized combustion chamber, powered by gaseous fuels; while Fig. 1.4(b) shows radial injection of the powder with liquid fuel, such as kerosene, instead of combustible gases, thus allowing for higher dissipated powers. In both cases, cooling water is used to improve torch robustness, and its thermal efficiency (Boulos et al. 2021).

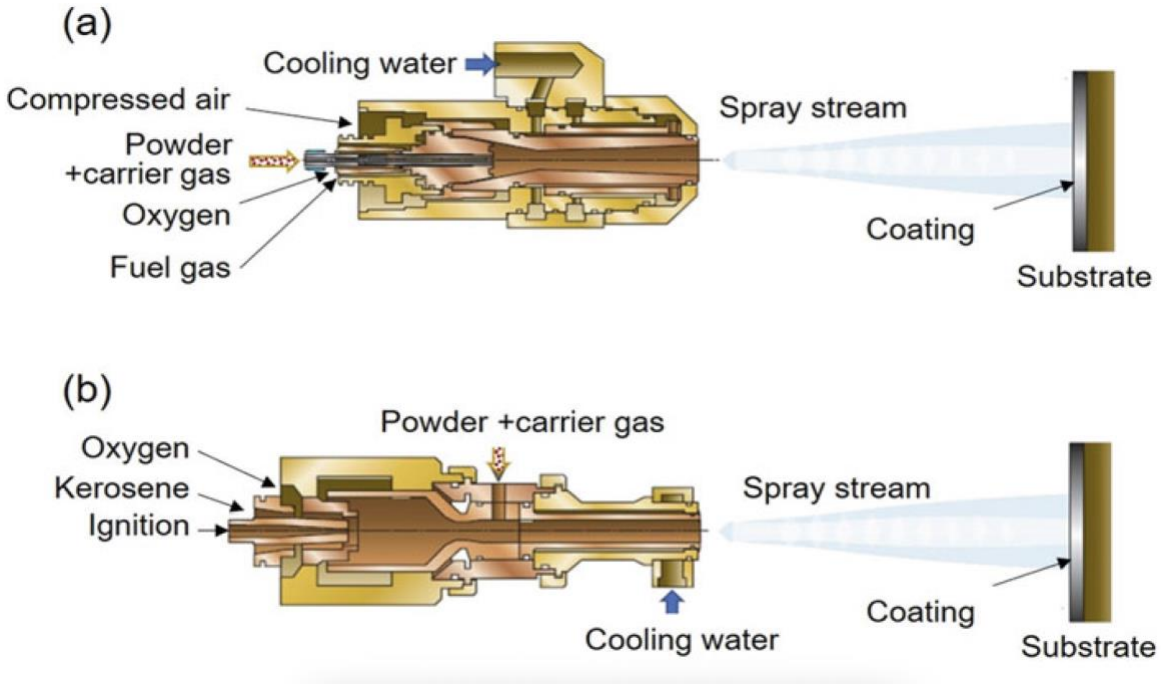


Fig. 1.4 Schema for a typical HVOF process with (a) water-cooled, gaseous fuel gun; and (b) water-cooled, liquid-fueled gun

### *1.1.4 Plasma Spraying*

As the noun declares, PS utilises a high-temperature plasma spray. Commonly used plasma gases to generate the plasma jet include Argon, Hydrogen, Helium, Nitrogen, or their mixtures. With core temperatures reaching up to 20,000°C, the feedstock particles experience rapid heating and melt instantly. As a compressed gas propels the molten, and semi-molten particles onto the substrate, they subsequently cool down, thus forming a dense bond coat. PS coats can be deposited to many surfaces, like metals, alloys, and even ceramics (Singh et al. 2025; Zhou and Vassen 2023; Ma and Ruggiero 2018). It is widely used in aerospace manufacturing for its ability to produce coatings with high thickness, and density, and enhanced bonding strength (Singh et al. 2025; Su et al. 2016; Chen et al. 2015; Lima and Marple 2005; Remesh et al. 2003). Further, it allows for different microstructures with varying properties. However, special care must be given to ensure low levels of porosity (Singh et al. 2025; Martin et al. 2023; Satish et al. 2023; Yuan et al. 2023; Hui et al. 2007). Fig. 1.5 gives a visual depiction of the procedure (Singh et al. 2025).

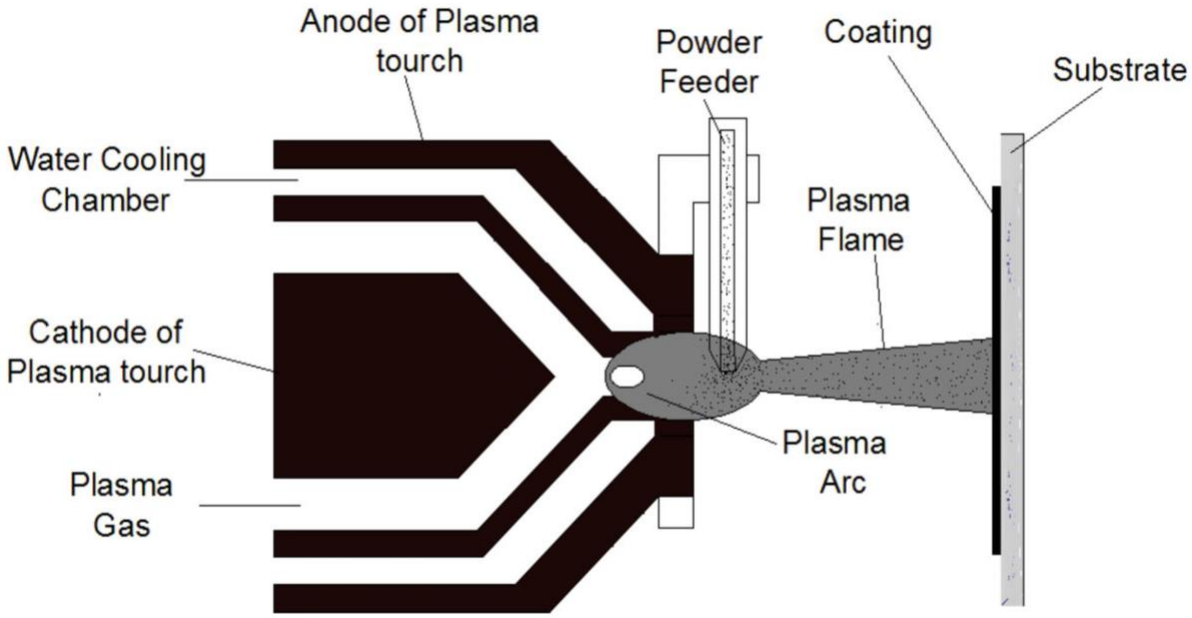


Fig. 1.5 Schema for a typical PS process

### *1.1.5 Cold Spraying*

Also called kinetic metallisation, CS is a rather unique TS process in a way that it can be carried out at lower temperatures, usually up to a maximum of 900°C, because the feedstock need not be heated (Singh et al. 2025; Poza and Garrido-Maneiro 2022; Schmidt et al. 2006). In these settings, a supersonic jet accelerates the solid powder to very high velocities using compressed air (Singh et al. 2025; Dykhuizen and Smith 1998). The subsequent with-substrate collisions cause the particles to deform plastically. The cold welding that thus happens gives us a cohesive coating. It is excellent for applications where high temperatures altering the particles' properties is undesirable. Moreover, it seeks minimal heat input (Singh et al. 2025; Basak et al. 2024a, b; Ashokkumar et al. 2022a, b). CS stands out in the way in which it operates at very low temperatures and thereby produces coatings without any thermal breakdown (Singh et al. 2025; Della Gatta et al. 2022; Villafuerte 2011; Schmidt et al. 2009; Li et al. 2006). CS process gives us dense coatings with little changes to the properties of particles. CS coatings are also versatile with an enhanced bonding strength. There do, however, exist limitations when it comes to coating thickness, adhesion, porosity, and roughness (Singh et al. 2025; Saharkhiz et al. 2023; Kumar 2022; Karthikeyan 2007; Champagne et al. 2005). Fig. 1.6 gives a visual depiction of the procedure (Champagne et al. 2005).

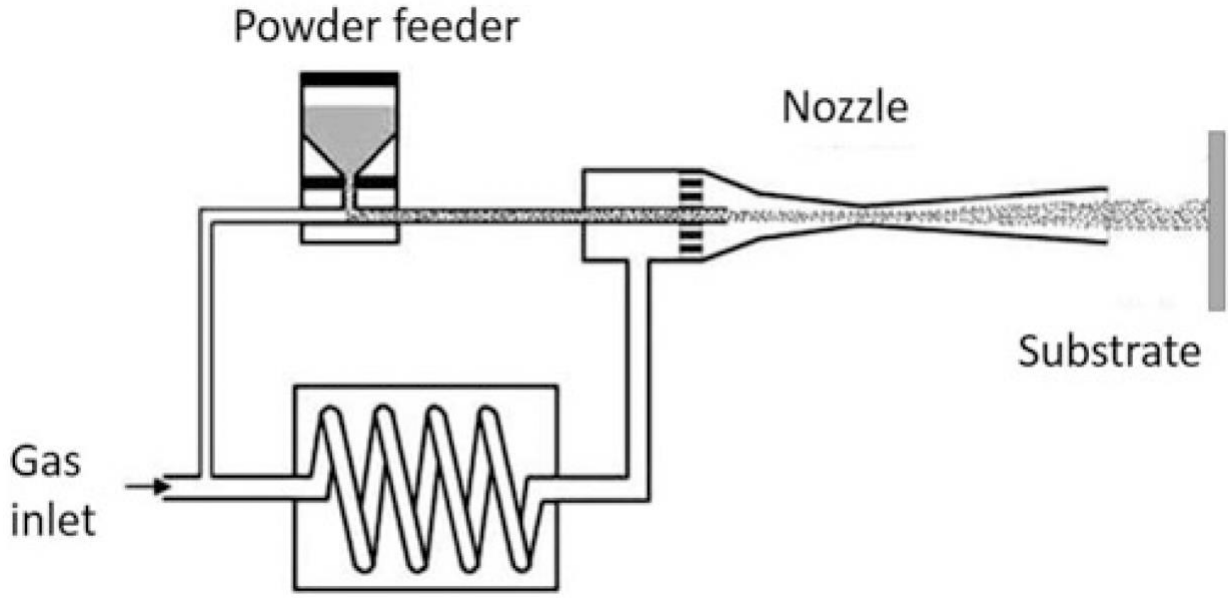


Fig. 1.6 Schema for a typical CS process

## 1.2 Plasma Spraying

In PS, an electric arc between a cathode, and an anode nozzle is used to produce plasma within a spray gun. The plasma gas enters the base of the cathode and exits the nozzle at very high temperatures, and velocities. Depending on the operating conditions, peak temperatures at the nozzle can be 15,000 – 20,000°C and peak velocities can be 500 – 2,500 $m.s^{-1}$. Feedstock powders can either be injected radially, or axially, which are then accelerated, and propelled by the plasma onto the substrate, where they subsequently solidify to form splats and produce a coating. A free-moving torch allows for the application of coatings on substrates of virtually any shape, or size. It is an iterative process, i.e. the coating is built over multiple passes. PS is a versatile technique because of its wide-ranging benefits; including, but not limited to, thermal protection; corrosion, and wear resistance; and tribological, and oxidation resistance. However, arc instabilities, plasma fluctuations, and fluid dynamic instabilities result in decreased process reproducibility. Control strategies must also factor in very broad time scales associated with the procedure, ranging from splat formation in a few microseconds to plasma torch 'burn-in time' of about an hour (Fauchais et al. 2013).

In PS, the key equipment is the torch. A control console enables tweaking of process parameters, such as arc current, plasma flow rate, carrier gas flow rate, and powder mass flow rate. It also houses safety interlocks that prevent arc initiation sans cooling water. Other pertinent systems are a high frequency starter unit, plasma gas supply, powder feed, power supply, and a high pressure cooling water system. The primary gas must be heavy, so Argon (Ar) is commonly used for its low energy density. To increase gas velocity, raise power density, and improve heat transfer rates to powders, a secondary gas could be used, such as Hydrogen ($H_2$), Helium (He), Nitrogen ($N_2$), or Carbon dioxide ($CO_2$). Nowadays, the usage of ternary mixtures is also widespread with Ar–$N_2$–$H_2$, and Ar–He–$H_2$ mixtures as popular choices. The power supply is typically managed by a current-controlled rectifier. The cooling water is supplied using deionised water, pressurised to an excess of 1 MPa. The high pressure prevents film boiling in regions of maximum heating (Fauchais et al. 2013).

In this section, we shall talk about different configurations of the PS process, particularly Atmospheric Plasma Spraying (APS), Suspension Plasma Spraying (SPS), and Vacuum Plasma Spraying (VPS).

### *1.2.1 Atmospheric Plasma Spraying*

APS is the simplest PS configuration, wherein the plasma torch is operated in an open discharge mode, engendering a high-temperature, high-velocity jet, into which the feedstock is injected. An open discharge operation makes the process a little more complex by virtue of the mixing of ambient air with the jet. The entrained air quenches the jet, modifies its structure, and alters its temperature field. While the stated effects are hardly of any consequence to oxide ceramics, they can partially oxidise metallic particles. Nonetheless, APS is economically advantageous, given its lack of limitations regarding the shape, and size of the substrate (Boulos et al. 2021; Fauchais 2004; Fauchais and Vardelle 2003; Janisson et al. 1998). Fig. 1.7 shows the underlying mechanism in a diagrammatic form (Boulos et al. 2021).

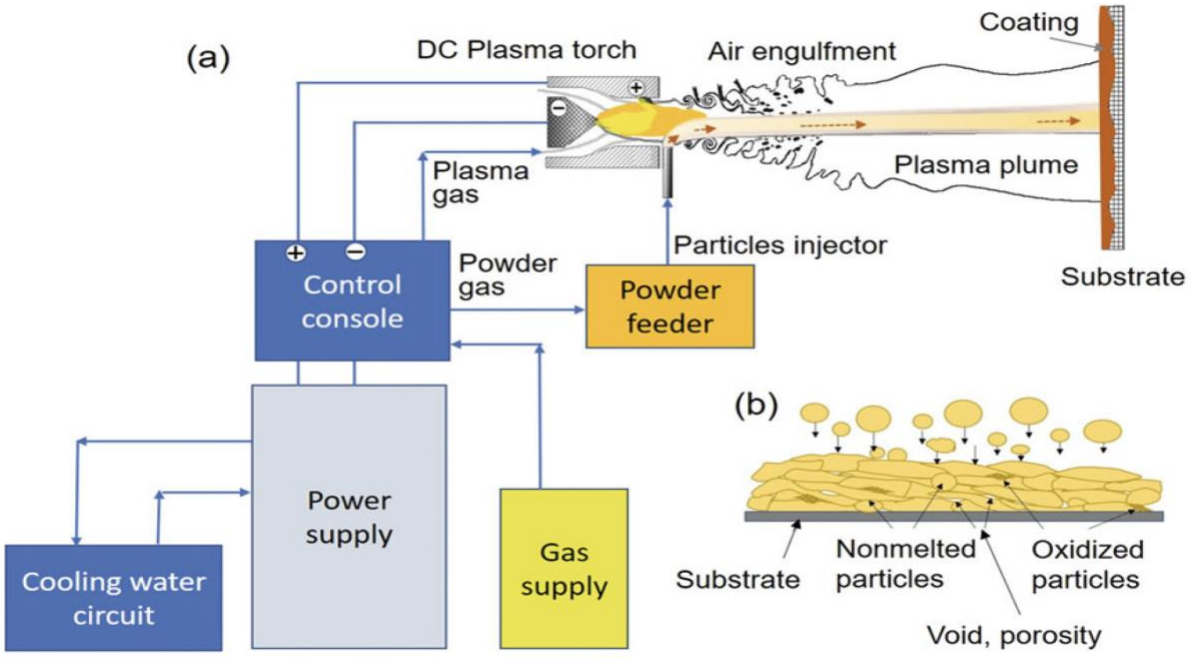


Fig. 1.7 Schema for a typical APS process

### *1.2.2 Suspension Plasma Spraying*

Typically used to produce advance Thermal Barrier Coatings (TBCs), SPS is a relatively new TS process that is compatible with very fine particles with diameters in the range of 100 nanometres to 5 micrometres. Because of their low masses, the carrier gas for these particles is replaced by a liquid to give them the requisite momentum to penetrate into the plasma stream. The feedstock consists of a fine-grained powder suspension (or slurry) that is injected into the jet, wherein the slurry's liquid component evaporates rapidly, leaving behind particles to atomise, and subsequently impact the substrate to form a porous coating. SPS gives us high strength, and durable coatings with smaller pores. Moreover, TBCs produced with SPS have a low thermal conductivity, high thermal shock resistance, and greater segmentation crack densities. Segmentation cracks are vertical cracks running almost perpendicular to the substrate, typically forming between adjacent columns. These cracks act as stress-relief features, thereby improving strain tolerance. However, given SPS' low deposition rates, it is inconvenient when spraying thicker coatings (Ashtiani 2020; Azar 2018; Ganvir et al. 2014; Kassner et al. 2007). Fig. 1.8 outlines a schematic of the operation (Bai et al. 2018).

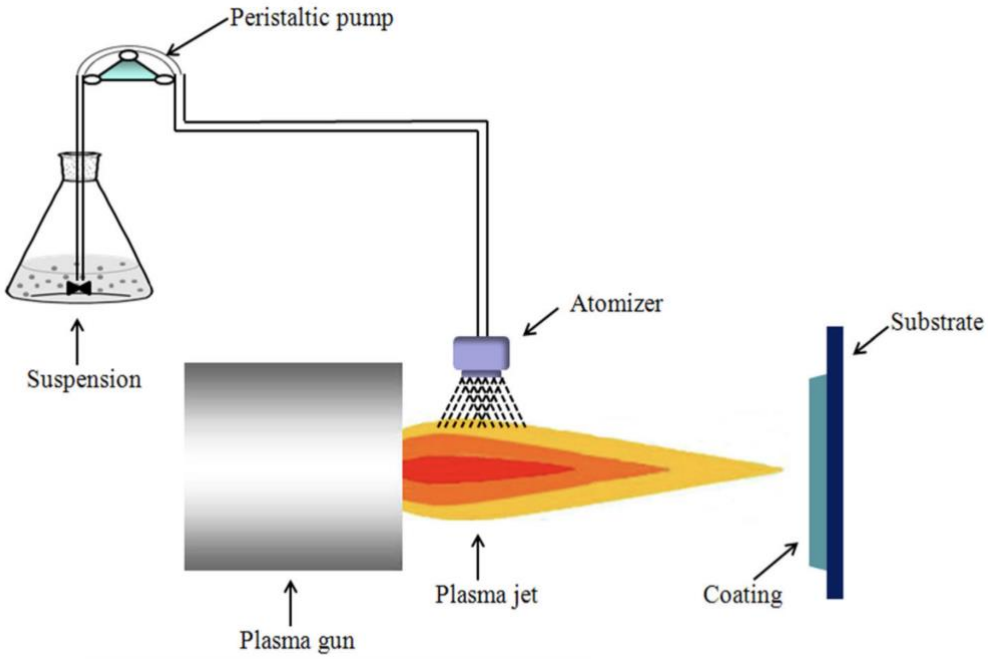


Fig. 1.8 Schema for a typical SPS process

### *1.2.3 Vacuum Plasma Spraying*

Developed in 1974 by Öerlikon Metco, VPS is also called Low-Pressure Plasma Spraying (LPPS). As the term indicates, VPS is undertaken in a vacuum chamber with pressures ranging from 5 kPa to 70 kPa. Carrying out PS in such a fashion prevents oxidation of the feedstock particles; allows for the coating of high-temperature substrates; promotes interdiffusion, and adhesion; stabilises plasma jets by lowering density gradients between the jet, and ambient atmosphere; provides more uniform particle acceleration, and less diverging particle trajectories; and reduces superheating of particles. Though VPS is excellent for coating complex shapes, it is best-suited for small- to medium-sized parts. The requisite capital for installing VPS infrastructure is another limitation of the process (Boulos et al. 2021; Meyer and Hawley 1991). Fig. 1.9 provides a conceptual layout of the process (Boulos et al. 2021).

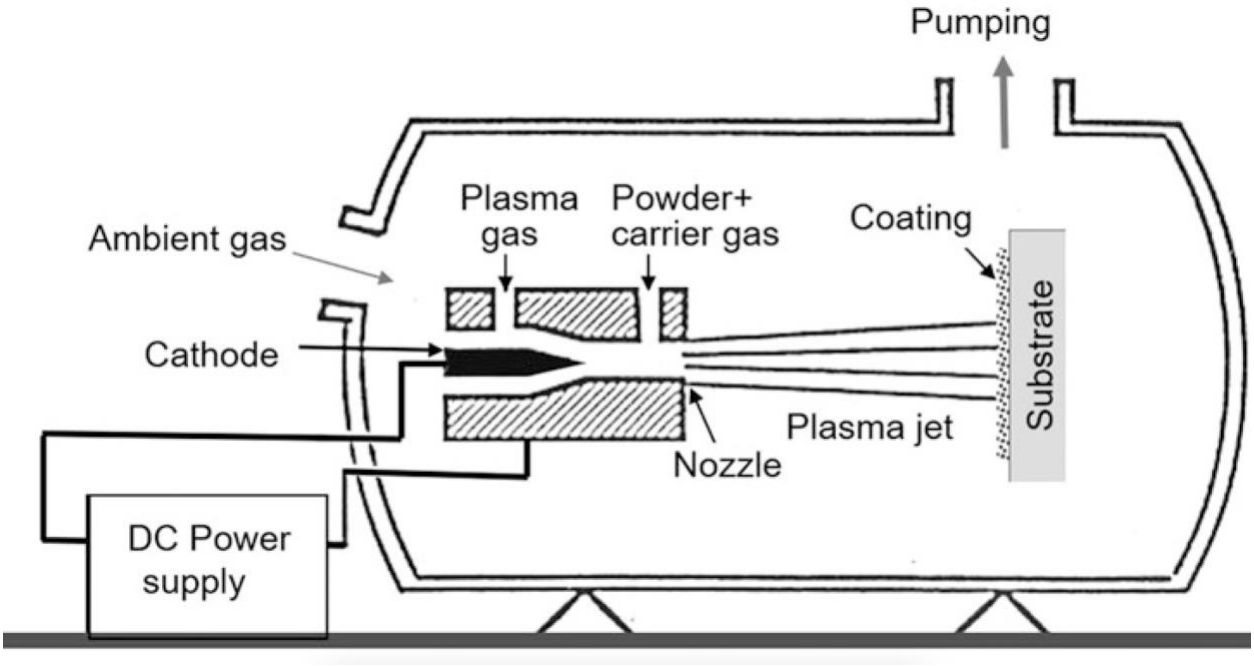


Fig. 1.9 Schema for a typical VPS process

## 1.3 Parameter-Driven Variability in Coating Outcomes

The previous sections talked about the TS family of processes with their individual pictorial impressions. In the bigger picture, this study aims to identify process parameters that most affect the coating performance, and to toggle the former to optimise the latter. Three parameters were seen to be especially influential in this regard, namely stand-off distance, spray rate, and particle temperatures. To reduce porosity, for instance, one could reduce the spray distance, and discharge velocity. This section looks at important process elements and their effects on the quality of coatings, which could be quantified by its adhesion, density, porosity, and roughness (Singh et al. 2025; Menasri et al. 2022). The microstructure of any coating is also imperative. Among the variables that influence the coating microstructure include spray angle, particles' velocities, torch speed, heat transfer, and gas flow rate (Singh et al. 2025; Neo et al. 2022; Wentz 2009).

### *1.3.1 Parameters*

#### *1.3.1.1 Standoff Distance*

Standoff distance is the distance between the torch nozzle, and the substrate. Typically, as the standoff distance goes up, the coating thickness goes down because of the dispersion of particles before they could land on the substrate surface. Evidently then, as the standoff distance is brought down, the coating thickness grows (Singh et al. 2025; Phiri et al. 2018; Bar-Hen and Etsion 2017; Kim et al. 2013). Also, the standoff distance can influence voids, and particle concentration. Subsequently, a relatively higher standoff distance would cause a decline in cohesion and the coating's uniformity would take a hit. In contrast, a relatively lower standoff distance increases the probabilities of particles' flattening, and fusion, giving us thicker coatings with fewer pores (Singh et al. 2025; Odhiambo et al. 2019).

Further, an optimal standoff distance ensures that particles retain sufficient velocity upon impact, enabling deep penetration and mechanical interlocking with the substrate surface. This interlocking enhances adhesive strength. In contrast, a suboptimal standoff distance—either too short or too long—can result in inadequate particle embedding and weak adhesion (Singh et al. 2025; Poza and Garrido-Maneiro 2022). These effects are governed by the existence of a critical velocity, below which particles fail to adhere and may even erode the substrate instead of forming a coating (Singh et al. 2025; Li et al. 2008). The cooling rates of particles upon contact with the surface are influenced by the standoff distance. A shorter standoff distance reduces the in-flight time, thereby limiting the extent of convective heat loss to the surrounding atmosphere. As a result, particles retain more

thermal energy and impinge on the substrate at higher temperatures. Conversely, a higher standoff distance increases the in-flight duration, exposing the particles to more ambient cooling. This prolonged exposure leads to greater heat dissipation, causing the particles to impinge at comparatively lower temperatures (Singh et al. 2025; Habib et al. 2022). Furthermore, a longer standoff distance is linked to higher probabilities for the particles to rebound or overspray, leading to reduced coating effectiveness. On the contrary, a shorter distance calls for the deposition of more particles with greater coating efficacy (Singh et al. 2025; Gaur et al. 2023). Finally, the choice of substrate, the selection of feedstock, and the particle size distribution are some variables that can help with the determination of an ideal standoff distance. Laser sensors, and standoff gauges are some of the diagnostic instruments that can aid in the process (Singh et al. 2025; Mauer and Moreau 2022; Zhang et al. 2021).

#### *1.3.1.2Spray Rate*

Spray rate (the rate at which the feedstock is expelled through the nozzle) also proves to be critical in most TS processes, with direct implications to the coating buildup and, hence, to the resultant microstructure. The spray rate affects the kinetic energies of particles on impact, and the volume injected to the substrate during the coating process (Singh et al. 2025; Meeß et al. 2022; Klinkov et al. 2019). Spray rate can be quantified in terms of both mass flow rate, and volumetric flow rate in $g/s$, and $cm^3/m$ respectively. Generally, spray rates can be seen as proportional to the coating thickness, i.e. lower spray rates lead to thinner coatings and higher spray rates lead to thicker coatings. Thus, an optimal spray rate is necessary for a uniform coating, and quality finishing (Singh et al. 2025; Irissou et al. 2022; Fauchais et al. 2010).

#### *1.3.1.3Particle Velocity*

Particle velocity is the rate at which the particles travel, or the individual velocities of the particles, most notably denoted in feet per second, or metre per second. Each particle may have a different velocity, thus complicating the optimisation problem. This is also the case with the input datasets used for this code. Particle velocity influences many factors, such as the particles' trajectory, and their velocities on impact. Both these factors contribute to the kinetic energies of those particles. Subsequently, upon hitting a surface, they form "splats" (Singh et al. 2025; Holmberg and Matthews 1994). In theory, splat formation improves packaging of material particles, which bolsters adhesion. Too high of particle velocities could cause production errors, increase rebounding, or simply make the substrate too hot. To ensure desired properties, particle velocity must be accounted for,

along with the consequent splat formation (more on it in section 3.3). Several other variables also influence particle velocity, such as the gun itself, standoff distance, the feedstock material, the gas pressure, et cetera (Singh et al. 2025; Gaur et al. 2023; Fan et al. 2020; Morales et al. 2019; Armada et al. 2015).

#### *1.3.1.4 Particle Size Distribution*

The powder's particle size distribution gives us the range of sizes its constituent particles encompass. It can be represented in terms of the average particle size, or the D-values (D10, D50, & D90). The particle size distribution directly affects the coating microstructure (more on it in section 4.2). Literature shows that smaller particles form smoother coatings, and larger particles form coarser bondcoats. Coating thickness, and surface roughness are also pertinent parameters here (Singh et al. 2025; Xue et al. 2023; DebRoy et al. 2018; Sharma et al. 2017a).

#### *1.3.1.5 Chemical Composition*

Clearly, the powder's chemical composition would have a rather direct impact on the coating's properties. Ensuring the feedstock particles bind well with the substrate, precision in powder composition allows for formation of coatings as intended. To prolong the coating's life, and to increase its durability, corrosion-resistant alloys, and wear-resistant carbides could also be fed to the torch (Singh et al. 2025; Ahmady R et al. 2023; Jose et al. 2022). Especially, alloys with a similar chemical makeup as the powder improve metallurgical bonding (Singh et al. 2025; Pathanatecha 2019). Abrupt changes in composition could catalyse changes in hardness, toughness, porosity, and thermal stability (Singh et al. 2025; Kumar 2022; Kumar and Kumar 2021). Such changes could all further hamper adhesion, oxidation resistance, surface chemistry, and chemical reactivity (Singh et al. 2025; Al-Turaif and Bousfield 2004). Size analyses, flowability tests, and imaging technologies aid the regulation of the chemical composition (Singh et al. 2025; Warcaba et al. 2021; Salama et al. 2019).

#### *1.3.1.6 Heat Input (Power)*

The heat input, particularly in terms of power, affects melting, atomisation, and inter-particle bonding (Singh et al. 2025; Bobzin et al. 2021). While heat input gives us the total heat provided to the system during operation, power is a measure of the energy needed to supply that heat to the system. The former is commonly expressed as joules per centimetre-squared, or calories per square centimetres, and the latter is done as Watts, or kilowatts (Singh et al. 2025; Espallargas 2015). This thermal energy, in the form of heat, is

used for melting the feedstock (Singh et al. 2025; Sankaran 2015). Greater the input of heat, greater are the amounts of melting, atomisation, and inter-particle bonding (Singh et al. 2025; Hauer et al. 2019; Oksa et al. 2011). Prominent power sources include plasma generators, combustion chambers, or simply electrical supplies (Singh et al. 2025; Curry et al. 2020; Feuerstein et al. 2008).

### *1.3.2 Effects on Coating Quality*

The microstructure of a coating ultimately decides a coating's characteristics, and performance. The key to analysing a microstructure lies in its porosity, and density. Porosity measures the empty spaces (or pores) within a bondcoat, while density is a measure for the mass of the bondcoat per unit of its volume (Singh et al. 2025; Odhiambo et al. 2019). Particle velocity can be seen as inversely proportional to porosity. Thus, among the various TS processes, FS, and AS bondcoats exhibit higher levels of porosity, whereas PS, and HVOF bondcoats exhibit lower levels of porosity (Singh et al. 2025; Li et al. 2022). Any powder agglomerates, however, can increase porosity (Singh et al. 2025; Huang et al. 2022). Standoff distance, spray angle, and powder feed rate could be adjusted to control porosity. Apart from particles' velocities, their shapes, sizes, compositions, and potential to form splats determine the coating's packing density, and porosity. The smaller the particles, the denser are the bondcoats due to the ability of tiny particles to pack themselves closely. Also, higher impact energies, splat formation, and mechanical bonding increase density. Preheating the substrate could also allow for denser bondcoats. Both effects can become more pronounced with increased coating thickness, and the subsequent accumulation of layers, and production defects. Less number of layers could potentially minimise porosity and maximise density (Singh et al. 2025; Curry et al. 2020; Ghosh 2020; Abedini et al. 2006).

## 1.4 Numerical Modelling Techniques for Optimisation

Recent years have witnessed efforts to optimise process parameters, and powder characteristics to achieve higher-performance coatings via conventional experimental methods as well as contemporary numerical studies. Computer models simulate the spraying process, particle interactions with the substrate, and coating buildup. This section would look at a few modelling approaches available in literature (Singh et al. 2025; Mehta et al. 2024; Zhu et al. 2022; Vignesh et al. 2017).

### *1.4.1 Particle Trajectory Modelling*

This modelling approach tracks the in-flight motions, temperatures, and behaviours of particles from the nozzle to the substrate surface. Employing an Eulerian-Lagrangian framework, particles are treated as discrete entities within a continuous high-velocity gas phase. As these droplets undergo atomisation, vaporisation, and acceleration, their velocities and temperature histories are tracked post-breakup to evaluate deposition efficiency, and coating structure. The model accounts for varying injection angles, suspension properties, and chamber geometries, showing that both particle residence time and torch configuration critically affect final impact conditions. This trajectory analysis serves as a foundational tool to optimize feedstock design, injector layout, and substrate placement in suspension-based thermal spray systems. It simulates particle behaviour on impact and predicts the coating microstructure (Singh et al. 2025; Jadidi et al. 2015).

### *1.4.2 Solidification and Phase Transformation Modelling*

Solidification, and phase transformation models simulate how molten or semi-molten particles cool, and evolve post-impact, influencing splat morphology, grain structure, and coating integrity. These models are crucial for predicting microstructural outcomes such as porosity, residual stress, and the columnar-to-equiaxed transition (CET), which is often linked to crack formation. Contemporary approaches couple thermodynamic phase diagrams with kinetic interface models to capture solidification under rapid, non-equilibrium conditions. Parameters such as undercooling, dendritic growth rate, partition coefficients, and nucleation thresholds are incorporated to model grain refinement and phase stability. These simulations support the optimisation of process parameters and alloy compositions, particularly in additive manufacturing, and thermal barrier coating applications, where microstructural control is essential. By resolving transient thermal fields, and phase transitions, such models enhance predictive capability in coating design and performance evaluation (Singh et al. 2025; Du et al. 2024).

### *1.4.3 Heat Transfer Modelling*

This approach models the thermal behaviour of particles in the context of the Powder Bed Fusion (PBF) process. PBF simulations are widely used to predict and analyse melt pool geometry during deposition. While Computational Fluid Dynamics (CFD) models offer high accuracy by capturing convective effects, they are computationally intensive and depend on extensive thermophysical data. In contrast, industrial users often prefer heat conduction models for their simplicity and efficiency, though they typically lack the ability to capture melt pool convection—particularly Marangoni flow. To address this, some models artificially increase thermal conductivity to approximate convective effects, though

this method lacks consistency. In this study, the heat conduction model was improved by applying directional correction factors to an orthotropic description of thermal conductivity in the liquid phase. These corrections are calibrated against experimental melt pool geometries. The model also considers factors such as cooling rate and substrate temperature to predict thermal histories (Singh et al. 2025; Nikam et al. 2022).

## 1.5 Previous Work

The present work builds upon an in-house simulation framework initially developed by Azar SG (2018) and subsequently refined by Ashtiani BK (2020). This section briefly outlines the key contributions and limitations of the latter, which form the basis for this study.

| **Arc Current (A)** | **Arc Voltage (V)** | **Ar – $H_2$ mass flow rate (g/s)** | |
|---|---|---|---|
| 500 | 65 | 1.48 (10% volume fraction) | |
| | **Units** | **Molten zirconia** | **Ethanol** |
| *Density* | $Kg/m^3$ | 5680 | 789 |
| *Specific heat* | J/kg.K | 1387 | 2470 |
| *Surface tension* | N/m | 1.5000 | 0.0223 |
| *Melting point* | K | 2988 | - |
| *Boiling point* | K | 5273 | 351 |
| *Viscosity* | $mm^2/s$ | 6.5000 | 1200 |
| *Melting latent heat* | kJ/kg | 707 | - |
| *Boiling latent heat* | kJ/kg | 9000 | 855.2370 |

Table 2.1 Injection conditions, and material properties as used by Pourang et al.

Ashtiani utilised particle distribution data generated by Pourang et al. (2016), based on CFD simulations of the 3MB Oerlikon-Metco plasma torch, as illustrated by Fig. 1.10, operating under predefined injection and torch conditions, as summarised in Table 2.1. The dataset provided particle trajectories, velocity components, and diameters, recorded at a standoff distance of 100 μm from the substrate surface. Beyond a hundred microns, Ashtiani assumed these droplets follow linear paths, determined by their respective velocity vectors, until impacting either the substrate or another particle.

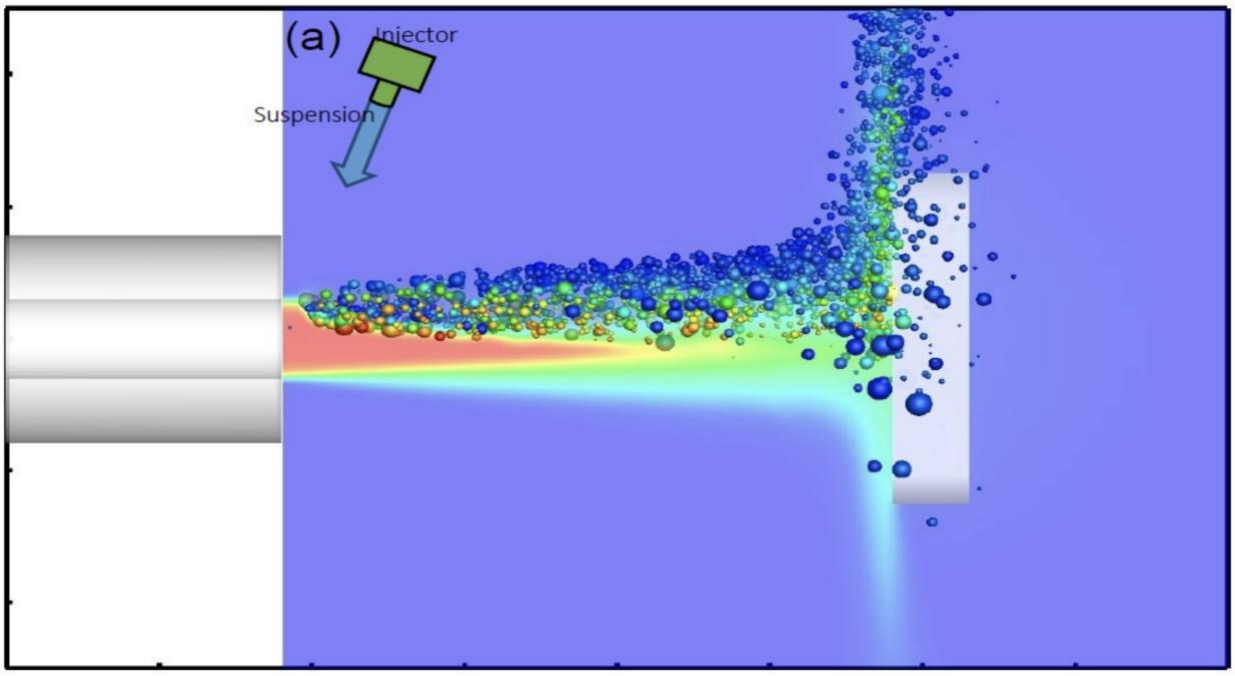


Fig. 1.10 Pictorial representation of the simulation as run by Pourang et al.

In reality, not all particles adhere upon impact — some rebound or splash off. However, Ashtiani's model neglects these secondary effects. Since Pourang's simulations assumed a steady-state plasma jet, the model also does not account for the effect of plasma fluctuations. Furthermore, Ashtiani introduced two different simulation strategies, namely the "frozen", and "flattened" models, that work on the same computational approach. While the former neglects the formation of any splats, the latter does not. However, a key limitation here is that both models are mutually exclusive, i.e. the code enforces a binary choice whereby either all particles flatten, or none do.

The **frozen model** assumes that particles retain their spherical shape upon impact. This is justified by scenarios involving small droplets, which due to their low thermal inertia, solidify rapidly upon contact. Moreover, such particles tend to follow plasma streamlines closely and have minimal perpendicular momentum, reducing the likelihood of deformation. This model is best suited to conditions involving high injection rates, increased standoff distances, and low torch power, where particle-substrate interactions are minimal.

The **flattened model** presumes that each particle spreads on impact to form a splat. This approach assumes the particle's temperature exceeds its melting point and that the temperature difference between particle and substrate has negligible effect on spreading. The splat is modelled as a kite consisting of smaller spheres of a user-specified diameter, as depicted by Fig. 1.11 (Ashtiani 2020).

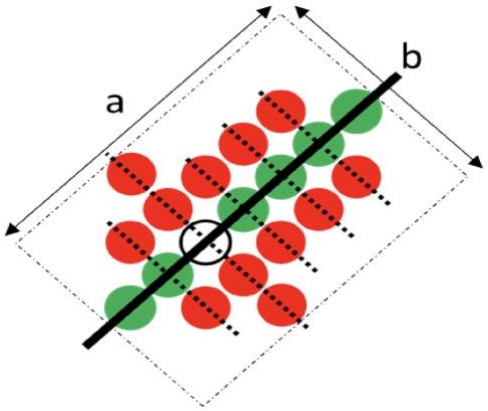


Fig. 1.11 A kite-shaped splat as formed by smaller constituent spheres

Based on the conservation of mass, the kite takes up the same volume as that of the sphere before impact. However, this method leaves voids between particles, thus overestimating porosity. To tackle this, three approaches were considered, namely Raining idea, Carpet idea, and Adaptive idea, as shown by Fig. 1.12 (Ashtiani 2020). To preserve the integrity of splat, and reduce the levels of porosity, the model implements the adaptive idea. Yet, due to the overestimation of interspace between deposited particles, the levels of porosity remain relatively high.

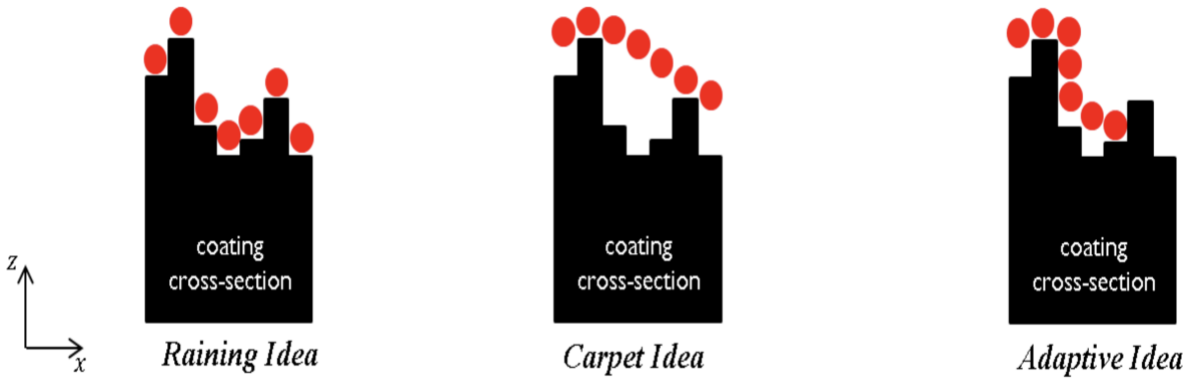


Fig. 1.12 Three approaches to model splat deposition on the substrate

The particle distribution data from Pourang et al. (2016) transmitted information in packets (called parcels) of particles with identical properties, as illustrated in Table 2.2.

| | $x_p$ | $y_p$ | $z_p$ | $v_x$ | $v_y$ | $v_z$ | $d_p$ | $N_p$ |
|---|---|---|---|---|---|---|---|---|
| *Parcel 1* | $x_1$ | $y_1$ | $z_1$ | $v_1$ | $v_1$ | $v_1$ | $d_1$ | $N_1$ |
| *Parcel 2* | $x_2$ | $y_2$ | $z_2$ | $v_2$ | $v_2$ | $v_2$ | $d_2$ | $N_2$ |
| ... | ... | ... | ... | ... | ... | ... | ... | ... |
| *Parcel n* | $x_n$ | $y_n$ | $z_n$ | $v_n$ | $v_n$ | $v_n$ | $d_n$ | $N_n$ |

Table 2.2 Tabular representation of particle distribution data by Pourang K

Here, $x_p$, $y_p$, and $z_p$ are x, y, and z coordinates of the particles in a given parcel;
$v_x$, $v_y$, and $v_z$ are velocity vectors of the particles in x, y, and z directions;
$d_p$ is the diameter of a given particle; and
$N_p$ is the number of particles in any parcel.

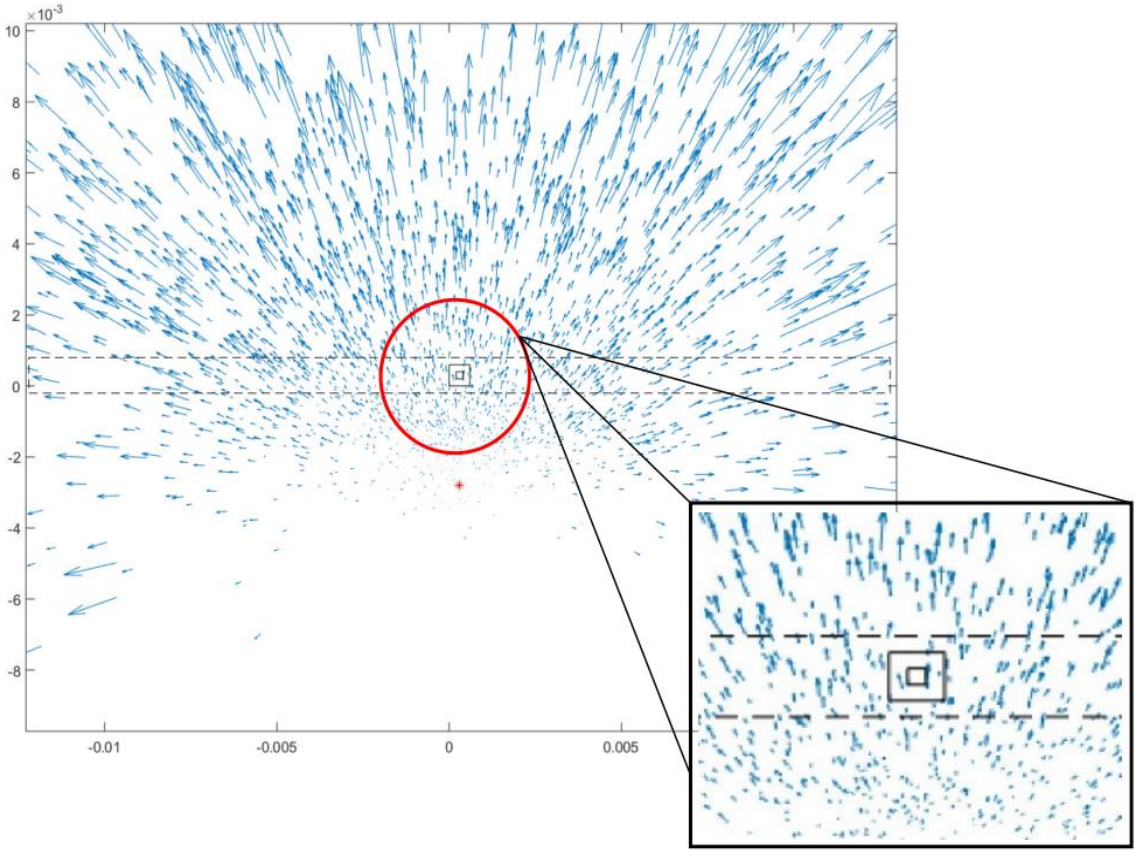


Fig. 1.13 Particle distribution of the input data from Pourang et al.

The substrate is a square of 200×200 μm$^2$, enclosed within a larger 600×600 μm$^2$ square to minimise edge effects. To simulate the motion of torch, its velocity is set to 1 μm/μs (=1m/s). Ashtiani modelled three configurations for the torch, namely linear, perpendicular-linear, and full-raster, as shown in Fig. 1.14 (Ashtiani 2020), depicted in red, green, and black respectively. As the green line delineates, the perpendicular-linear raster cuts through the middle of the modelled area along the X-axis. As the red line outlines, the linear raster runs three millimetres below the modelled area, also along the X-axis. Finally, as the black lines showcase, the full raster sweeps across both X, and Y axes with a spacing of three millimetres between successive X-axis passes.

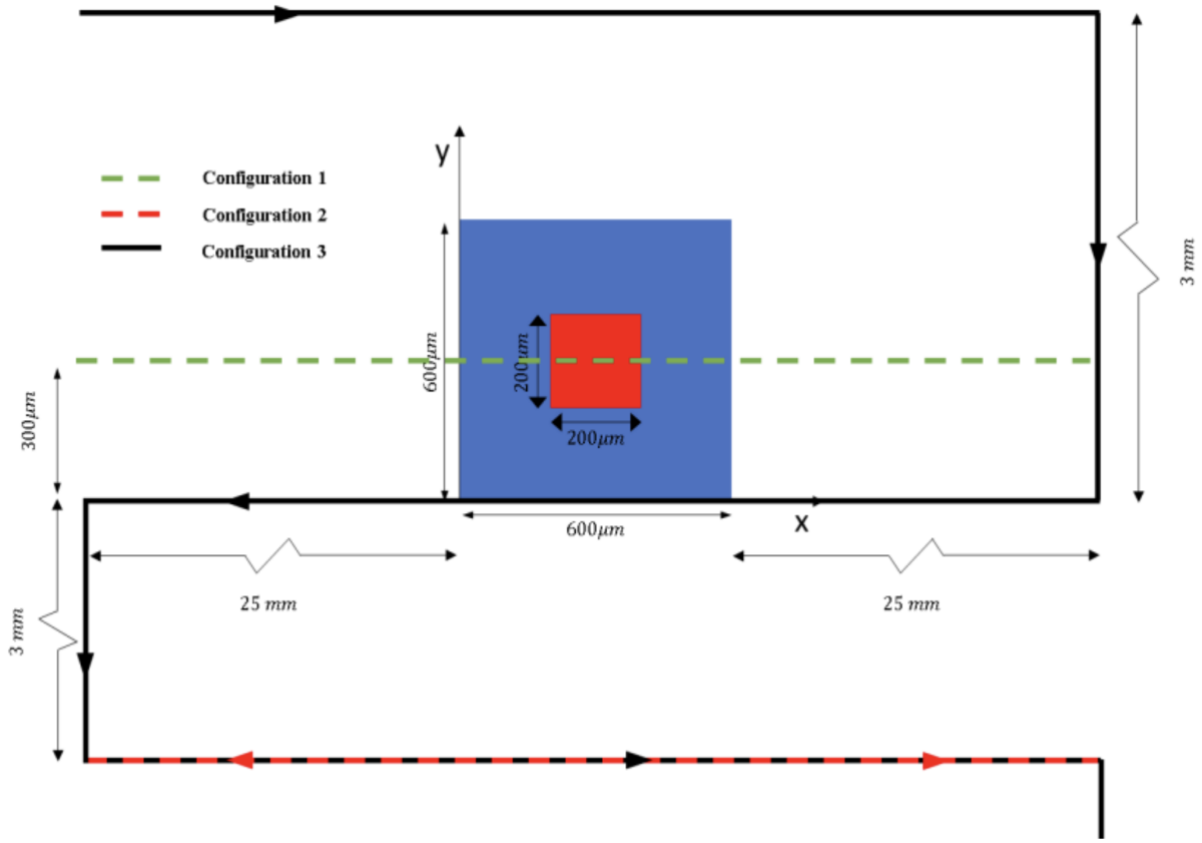


Fig. 1.14 Substrate dimensions and gun sweeping patterns

## 1.6 Objectives of the thesis

This thesis aims to improve and exploit an in-house numerical model that simulates coating build-up in SPS with the broader goal of supporting process optimisation, and design in both research, and industrial contexts. By enabling virtual experimentation across a wide range of spray configurations, particle distributions, and substrate geometries, the model provides a cost-effective, and time-efficient alternative to extensive physical trials. It is intended as a predictive tool that allows users to study the effects of key parameters—such as injection orientation, particle temperature, and plasma fluctuations—on coating morphology, and deposition efficiency.

Specifically, this study investigates two datasets (A and B) derived from numerical simulations using ANSYS Fluent of the Mettech Axial III plasma torch. These datasets are employed to explore how (a) interpeak distances of asperities, (b) particle velocity distributions, (c) spray gun traverse velocities, and (d) database representative times influence the resulting coating morphologies and their microstructural characteristics, including column formation, columnar density, and vertical cracking. Based on these findings, the thesis also offers recommendations on which parameter configurations are best suited for achieving specific coating outcomes.

Ultimately, the model contributes to a deeper understanding of the SPS process, enabling researchers to explore hypotheses regarding coating formation mechanisms and assisting engineers in tailoring spray conditions to meet targeted application requirements. The framework further lays the groundwork for future integration with data-driven optimisation tools and real-time process control systems.

# Chapter 2: **METHODOLOGY**

## 2.1 Introduction

This chapter details the numerical simulation methodology used to model particle deposition from a spray gun onto a substrate, typical of not just Suspension Plasma Spraying processes but also other thermal spraying processes. The methodology was originally developed by Azar SG (2018) and later refined by Ashtiani BK (2020). It encompasses particle trajectory prediction, impact diagnosis, and coating evolution through multi-pass spray deposition. The simulation models the motion, impact, and bonding of sprayed particles using a structured computational approach. The algorithm incorporates:

- Particle transport equations to predict velocity and position;
- Spray gun dynamics to simulate multi-pass deposition;
- Substrate interaction models for adhesion and spreading behaviour;
- Dynamic surface evolution for realistic layer-by-layer deposition.

## 2.2 Initial Conditions and Input Data

The simulation begins with an initialisation phase where particle properties, substrate geometry, and spray gun characteristics are defined.

### *2.2.1 CFD Data*

A dataset containing particle parameters is imported from relevant CSV files. The pertinent properties extracted include:

- Particles' initial positions: $X_p$, $Y_p$, and $Z_p$
- Particles' velocity components: $U_p$, $V_p$, and $W_p$
- Droplets' sizes: $d_p$
- Droplets' temperatures: $T_p$
- Number of particles per computational parcel: $N_p$

These properties are stored in an array for further calculations.

| | Dataset A | Dataset B |
|---|---|---|
| *Gun* | Mettech Axial III torch | |
| *Suspension* | YSZ in Ethanol | |
| *Suspension flow rate* | 45 mL/min | |
| *Standoff distance* | 75 mm | 100 mm |
| *Power* | 100 kW | 90 kW |
| *Plasma flow rate* | 245 slpm | 200 slpm |
| *Volume fraction* | 80% Ar – 20% $H_2$ | 75% Ar – 10% $N_2$ – 15% $H_2$ |

Table 2.3 Properties of the datasets used for the purposes of this study.

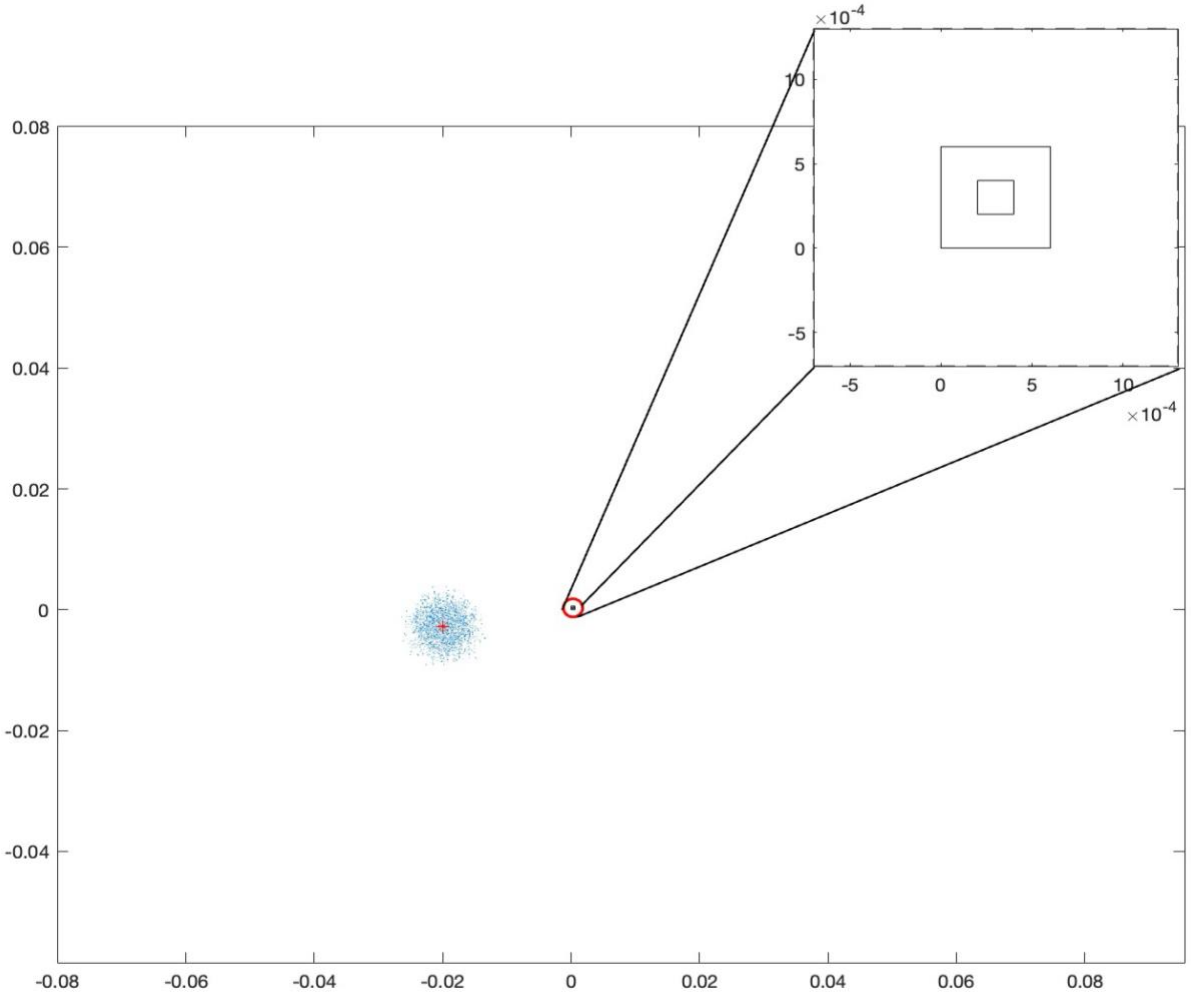


Fig 2.1 Particle distribution of the dataset A

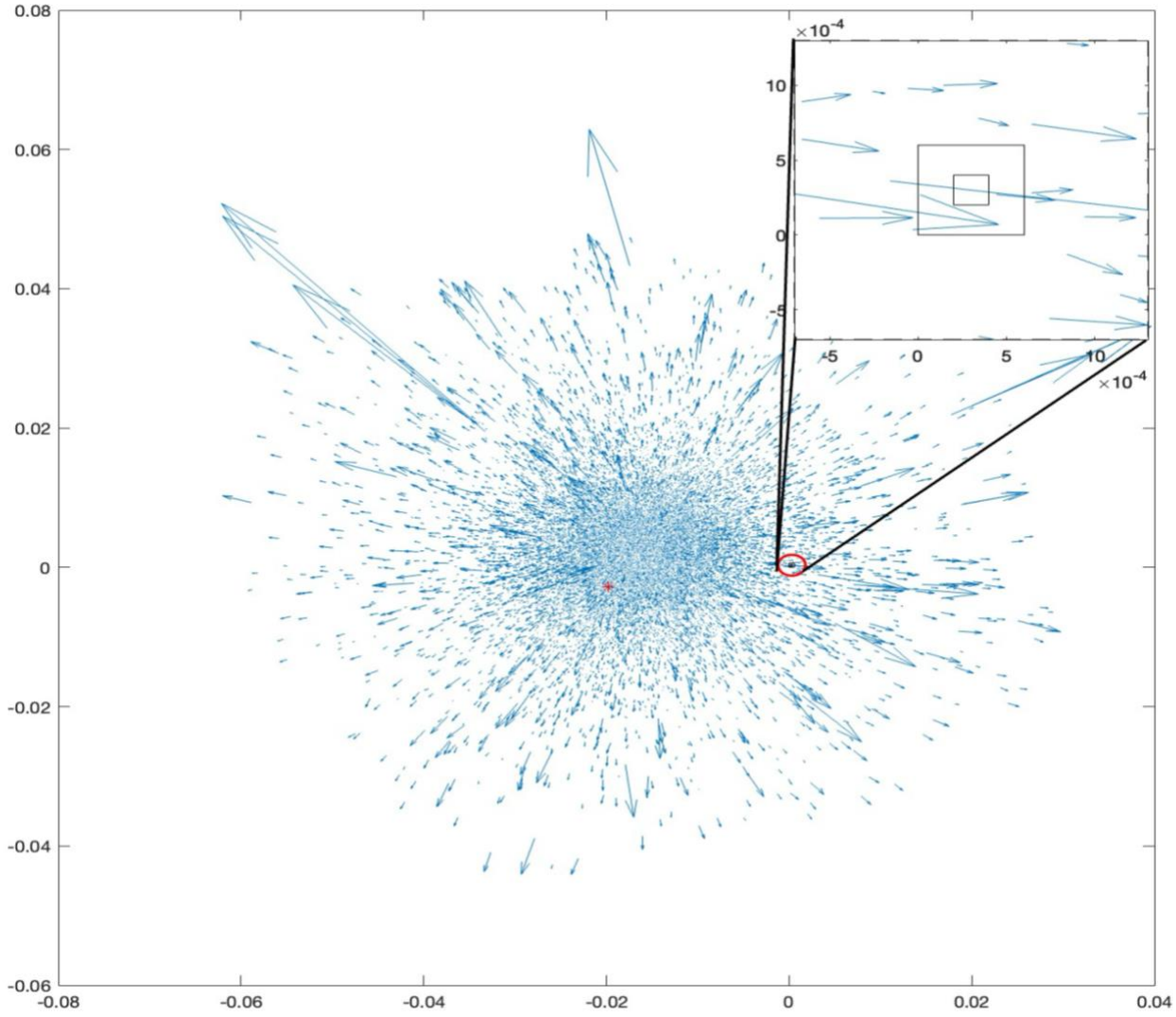


Fig 2.2 Particle distribution of the dataset B

### *2.2.2 Spray Gun Characteristics*

The spray gun is defined by its initial position and velocity. The gun traverses the substrate in a sweeping motion, altering its position with each pass. The spray gun moves incrementally along the X-axis:

$$X_g = X_g + sign \cdot 1.0 \times 10^{-6} \qquad \text{[eq. 1]}$$

When the gun reaches a boundary ($X_g > 15\ mm$ or $X_g < -20\ mm$), direction reverses.

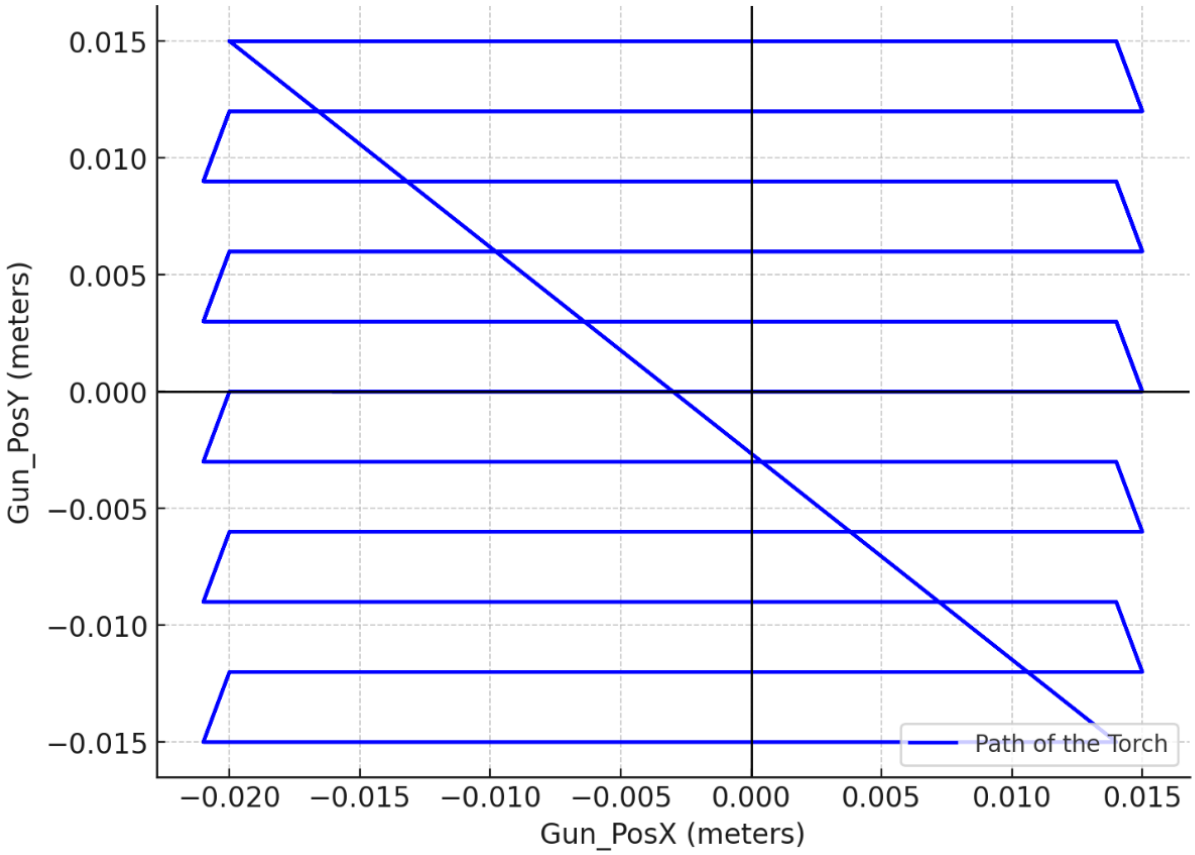


Fig. 2.3 Gun sweeping motion

### *2.2.3 Substrate Definition*

The substrate is initialised with a predefined roughness value to account for surface irregularities. A spatial grid is defined over the substrate to track deposited particles. In section 4.3, many different substrates have been taken into consideration for the purposes of this study.

## 2.3 Structured Point Generation for 3D Rough Surface Modelling

This section describes the computational approach used to generate a substrate using a structured 3D grid of discrete points representing a rough surface. The algorithm ensures an even (or uneven) distribution of points while considering the effects of surface roughness and layer-wise stacking. The structured point generation algorithm is implemented in MATLAB and designed to simulate a surface composed of spherical elements, considering:

- Base of the pyramids representing the asperities (`base`);
- Height of the aforementioned pyramids (`Sub_Rough`);
- Size of the spheres that make up the asperities (`Sub_Sphere_Size`).

The structured point generation follows a layered, row-wise, and column-wise approach. The computational domain is initialised with:

- Number of layers of spheres on top of one-another inside any asperity (`k_num`);

$$k_{num} = \left\lfloor \frac{\sqrt{\left(\frac{base - Sub\_Sphere\_Size}{2} \cdot \sqrt{2}\right)^2 + (Sub\_Rough - Sub\_Sphere\_Size)^2}}{Sub\_Sphere\_Size} \right\rfloor + 2 \quad \text{[eq. 2]}$$

- Layer-to-layer spacing to ensure only one sphere occupies the top layer (`k_dis`);

$$k_{dis} = \frac{\sqrt{\left(\frac{base - Sub\_Sphere\_Size}{2} \cdot \sqrt{2}\right)^2 + (Sub\_Rough - Sub\_Sphere\_Size)^2}}{k_{num} - 1} \quad \text{[eq. 3]}$$

- Angular inclination of the faces of the pyramids w.r.t. its base, i.e. how steep the pyramid is (`alpha`).

$$\alpha = \tan^{-1}\left(\frac{Sub\_Rough - Sub\_Sphere\_Size}{\left(\frac{base - Sub\_Sphere\_Size}{2} \cdot \sqrt{2}\right)}\right) \quad \text{[eq. 4]}$$

Further, for each layer, the algorithm computes:

- Number of rows of spheres for that layer (`j_num`);
- Row-wise spacing determined from the available width (`j_dis`);
- Column-wise spacing as the layers grow (`i_dis`).

A structured nested loop iterates through rows (`j`) and columns (`i`), with special handling of boundary rows (`j=1`, `j=j_num`) to maintain structure, ensuring evenly spaced spherical elements at each layer.

## 2.4 Particle Trajectory Estimation

The particles' landing positions are estimated using kinematic equations:

$$X_{land} = X_p + U_p \cdot \left| \frac{100 \times 10^{-6}}{W_p} \right| \qquad \text{[eq. 5]}$$

$$Y_{land} = Y_p + V_p \cdot \left| \frac{100 \times 10^{-6}}{W_p} \right| \qquad \text{[eq. 6]}$$

A randomness metric is computed to quantify deposition uniformity:

$$R = \frac{\Sigma(d_{min} \times N_{parcel})}{\Sigma N_{parcel}} \times \frac{1}{2} \qquad \text{[eq. 7]}$$

A while-loop iterates over multiple spray passes, continuously updating the system. A sub-function, `ProbableImpact` (more on it in section 3.1), determines which particles are likely to land on the substrate. For each impacting particle, its velocity components $(U_p, V_p, W_p)$ are extracted, positions $(X_p, Y_p, Z_p)$ are retrieved, and the spreading condition is checked based on temperature. This data is passed to another sub-function, `ImpactDiagnosis` (more on it in section 3.2), which decides whether a particle adheres to the substrate or bounces off.

# Chapter 3: **IMPLEMENTATION**

## 3.1 Computational Approach for Droplet Deposition Modelling

This chapter details the computational approach utilised for simulating the deposition and dispersion of droplets in a suspension plasma spray (SPS) environment. The numerical framework models the kinematic behavior of injected droplets, evaluates their spatial distribution, and incorporates probabilistic sampling methods to ensure realistic dispersion characteristics. The computational methodology consists of the following sequential steps:

- Determination of particles' landing locations;
- Filtration of particles in the deposition region;
- Computation of local droplets' statistics;
- Application of weighted sampling for droplets' selection;
- Introduction of random perturbations to droplets' positions.

The governing equations and numerical implementation details for each step are discussed subsequently.

### *3.1.1 Droplet Landing Position Calculation*

The position at which each droplet lands in the XY-plane is computed as:

$$X_{land} = X_p + U_p \cdot \left| \frac{Gun\_Pos_Z - Z_{mean}}{W_p} \right| \qquad \text{[eq. 8]}$$

$$Y_{land} = Y_p + V_p \cdot \left| \frac{Gun\_Pos_Z - Z_{mean}}{W_p} \right| \qquad \text{[eq. 9]}$$

This formulation accounts for the relative vertical displacement of the injection source, allowing for realistic trajectory estimation.

### *3.1.2 Domain Filtering*

Only droplets that land within the deposition region are considered:

$$Lines2 = Temp\_Array[(Sub\_Min\_X \leq X_{land} \leq Sub\_Max\_X) \wedge (Sub\_Min\_Y \leq Y_{land} \leq Sub\_Max\_Y)] \qquad \text{[eq. 10]}$$

Droplets outside the defined region are excluded from further calculations.

### *3.1.3 Local Droplet Statistics*

For the subset of droplets within the deposition region, the following properties are computed:

The volume-weighted mean droplet diameter is calculated as

$$D_{ave} = \sqrt[3]{\frac{\sum(N_p \cdot {d_p}^3)}{\sum N_p}} \qquad \text{[eq. 11]}$$

The total injected droplet volume per unit time is

$$Vol_{inj} = \frac{\sum\left[N_p \cdot \frac{4}{3}\pi\left(\frac{d_p}{2}\right)^3\right]}{\Delta t_{rep}} \qquad \text{[eq. 12]}$$

The number of droplets expected per deposition location is

$$ParPerLoc = \left\lfloor \frac{Vol\_inj}{\frac{4}{3}\pi\left(\frac{D_{ave}}{2}\right)^3} \right\rfloor \qquad \text{[eq. 13]}$$

### *3.1.4 Weighted Sampling of Droplets*

To accurately model droplet behavior, a probability-weighted random sampling is applied. Larger droplets, having a greater volume contribution, have a higher probability of being selected. The probability weight assigned to each droplet is given by

$$Weight = \frac{N_p \cdot \frac{4}{3}\pi\left(\frac{d_p}{2}\right)^3}{\sum\left[N_p \cdot \frac{4}{3}\pi\left(\frac{d_p}{2}\right)^3\right]} \qquad \text{[eq. 14]}$$

The droplets are randomly sampled using these weights.

### *3.1.5 Randomised Spatial Perturbations*

To account for turbulence and stochastic dispersion, the final droplet positions are randomly perturbed:

$$X_p = X_p + (-1 + rand() \times 2) \times R \qquad \text{[eq. 15]}$$

$$Y_p = Y_p + (-1 + rand() \times 2) \times R \qquad \text{[eq. 16]}$$

where $(-1 + rand() \times 2)$ is the perturbation term, which generates a random displacement in the range [–1, 1].

The described methodology is a physically consistent computational approach to model the deposition of droplets in a suspension plasma spraying (SPS) environment. The combination of volume-weighted sampling, and randomised perturbations ensures accurate representation of spray deposition patterns while maintaining computational efficiency.

## 3.2 Computational Algorithm for Inter-droplet Interactions Modelling

This section outlines the numerical procedure employed to simulate the interactions of individual droplets within a plasma spray plume with a dynamically evolving coating surface. The simulation is conducted within a discretised spatial domain, wherein such interactions with existing surface morphology are resolved using a deterministic, geometry-based impact model. To initiate the deposition process, the expected landing zone in the XY-plane is determined by extrapolating the trajectory until the droplet reaches $Z = 0$, or intersects with a previously deposited particle. The influence width in X and Y directions is calculated as:

$$\Delta X = \frac{D_s + D_{max}}{2\sin\left(\tan^{-1}\left|\frac{V_v}{U_v}\right|\right)} \quad \text{[eq. 17]}$$

$$\Delta Y = \frac{D_s + D_{max}}{2\cos\left(\tan^{-1}\left|\frac{V_v}{U_v}\right|\right)} \quad \text{[eq. 18]}$$

The particles previously deposited in the identified grid are queried from the spatial memory structure `Hub{}`. Each entry contains the positions, and diameters of earlier particles; the extracted values include $X_{surf}$, $Y_{surf}$, $Z_{surf}$, and $D_{surf}$. Particles close to the trajectory line are filtered using an elliptical proximity threshold:

$$\left|X_{surf} - \hat{X}(Z)\right| < \Delta X \quad \text{[eq. 19]}$$

$$\left|Y_{surf} - \hat{Y}(Z)\right| < \Delta Y \quad \text{[eq. 20]}$$

To determine the first point of contact, the trajectory is treated as a parametric line intersecting a field of spheres, representing previously deposited particles. If a valid intersection is found, the corresponding impact point is computed, following which the new droplet is added to the grid square corresponding to its impact coordinates.

If no collision is detected with a previous particle, the droplet is projected to land directly on the substrate. The landing location is computed by tracing the trajectory to the

substrate surface, and a similar logic is followed to insert the droplet into the `Hub` data structure and update counters. Each successful deposition updates the following global values:

- $Z_{max}$ : maximum coating height;
- $D_{max}$ : maximum particle diameter recorded;
- `Total_Num`: total number of deposited particles;
- `Sphere_Vol`: volume of material deposited in deposition region;

A sub-function, `SubParticles` (more on it in section 3.3), may be called to simulate splat formation if spreading is enabled for a given particle depending on its temperature, as discussed subsequently.

## 3.3 Geometric Modelling of Droplet Spread to Simulate Splat Formation

This section presents the numerical implementation developed to simulate the deposition footprint of individual droplets during the Suspension Plasma Spraying (SPS) coating buildup process. The approach accounts for the kinematic trajectory of incoming particles, their impact deformation on the substrate, and the spatial distribution of deposited material on a discretised domain. The simulation employs an elliptical spreading model governed by the particle's physical and kinematic parameters.

Upon impact, a molten droplet deforms, and spreads into an elliptical footprint whose orientation, and dimensions depend on its incident velocity vector, and volume. The primary assumptions in the model include:

- The droplet flattens into an elliptical shape;
- The major axis aligns with in-plane projection of the particle's velocity vector;
- Volume is conserved during deformation.

The angles of impact with respect to the coordinate planes are computed as:

$$\alpha_1 = \tan^{-1}\left|{}^{W_v}/_{U_v}\right| \qquad \text{[eq. 21]}$$

$$\alpha_2 = \tan^{-1}\left|{}^{W_v}/_{V_v}\right| \qquad \text{[eq. 22]}$$

$$\gamma = \tan^{-1}\left| W_v / \sqrt{U_v^2 + V_v^2} \right| \qquad \text{[eq. 23]}$$

These angles define directionalities of droplets, and subsequent elliptical deformations.

The effective footprint is defined by two semi-axes $a$ and $b$, which are computed based on the droplet's diameter, $D_s$, and effective substrate height resolution, $D_{sub}$. Assuming the droplet's volume remains constant before, and after impact, the semi-axes can be computed as:

$$a = {}^{4}/_{3} \cdot \frac{(D_s/2)^3}{D_{sub} \cdot b} \qquad \text{[eq. 24]}$$

$$b = max\left(\sqrt{{}^{4}/_{3} \cdot \frac{(D_s/2)^3}{D_{sub}}} \cdot \sin\left(\frac{\gamma}{{}^{\pi}/_{2}}\right),\ \frac{D_{sub}}{2}\right) \qquad \text{[eq. 25]}$$

Note that these parameters define the radial extents of the major, and minor axes of the deformed droplet.

Existing deposits in the footprint region are retrieved from the data structure `Hub`, as discussed in section 2.6. Once the neighbourhood has been mapped, the deposition process is executed by tracing the droplet's spread across the elliptical footprint. This is performed in two phases: backward, and forward spreading from the impact center. Each of these phases has calculations pertaining to spine, and branch structures.

The spine corresponds to the principal axis of deformation aligned with the in-plane velocity direction. For both forward, and backward regions, the droplet is advanced stepwise using radius increments, $R_{imin}$ or $R_{imax}$. At each of these steps, the sub-function, `Sub_Impact` (more on it in section 3.4), is called to:

- Update position and droplet size due to step displacement;
- Identify the impacted grid cell index `val`;
- Append the new deposition data into `Hub{val}`.

At every spine point, symmetric branches are generated perpendicular to the direction of spine. For each branch index $j$, new positions are computed using radial increments $R_{jmin}(i)$ or $R_{jmax}(i)$, depending on whether the point lies in the backward, or forward half. Each branch simulation also calls `Sub_Impact`, checks for valid grid cell indices, and deposits data into the appropriate grid cell.

This framework allows for high-resolution modelling of coating buildup during SPS by simulating the detailed footprint of individual droplets, accounting for impact dynamics, spread geometry, and deposition logic. The resulting substrate evolves with each impact, enabling accumulation, surface roughness development, and thickness tracking throughout the coating process.

## 3.4 Impact Location Corrections using Projection, and Overlap Analyses

This section outlines the geometric refinement procedure used to compute the most physically valid impact location for an incoming droplet in a simulated Suspension Plasma Spraying (SPS) environment. The algorithm considers possible overlaps with existing surface particles and resolves the final impact coordinates using projection, rotational alignment, and circular intersection logic. To determine which particles on the substrate surface may influence the incoming droplet's trajectory or landing, a radial search distance is defined as:

$$D_{search} = D_{sub} + \frac{D_{max}}{3} \qquad \text{[eq. 26]}$$

A projection plane is also defined in the XY-plane to estimate the likely area of droplet interaction. For each neighboring particle, a projection onto this plane is computed by calculating the perpendicular distance from the surface particle to the plane.

Further, a spherical overlap test is performed by comparing the radial distance between the droplet, and surface particle. If this radial distance is within their combined radii, a potential overlap is detected. A corrected impact point is computed in a rotated frame aligned with the local geometry, and flow direction.

For selecting the best-fit, among all possible locations, the point with the maximum height (z) is selected. If only one valid location is available, it is used directly. However, if no valid projection exists, a fallback strategy is employed; a circular projection is used to determine the XY-coordinates based on the droplet radius, and the distance from coating surface. The resulting impact location is solved analytically, ensuring the droplet lands realistically within the geometric constraints of the coating surface.

## 3.5 Summary

This chapter described the numerical modelling methodology for multi-pass particle deposition in a thermal spray simulation. Key elements include particle trajectory estimation, gun movement simulation, impact diagnosis and spreading behaviour, layer-by-layer deposition modelling, and dynamic surface height regulation.

Fig. 3.1 delineates all steps of the procedure in the form of a flowchart.

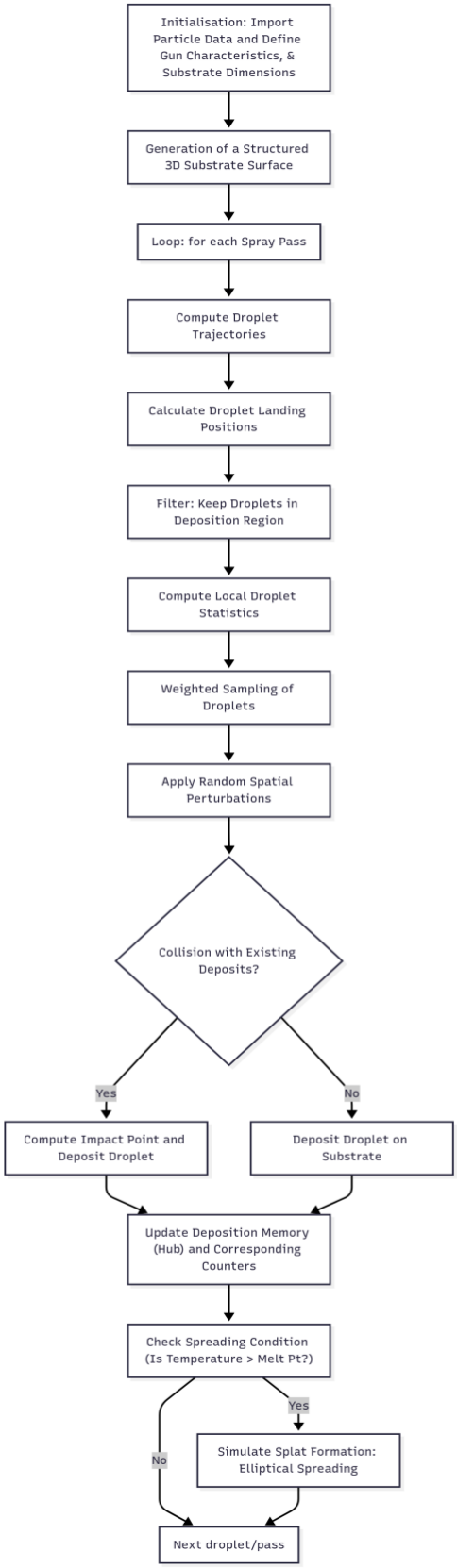


Fig. 3.1 A flowchart for the computational methodology employed by the model

# Chapter 4: **PARAMETRIC ANALYSES**

## 4.1 Introduction

Suspension Plasma Spraying (SPS) has emerged as a versatile technique for depositing yttria-stabilized zirconia (YSZ) thermal barrier coatings with tailored microstructures. Unlike conventional plasma spraying, SPS uses a fine suspension of YSZ particles, enabling the formation of columnar structures akin to those from electron-beam physical vapor deposition (EB-PVD) while retaining the flexibility of spray processing. The resulting coatings can exhibit strain-tolerant inter-columnar gaps and micron-scale porosity – features that lower thermal conductivity and enhance thermal cycling durability in gas-turbine applications. Indeed, SPS offers the possibility of producing coatings with a range of microstructures, from columnar or vertically cracked architectures to fully dense or porous deposits, by appropriate adjustment of process parameters. The present chapter focuses on how key deposition parameters influence the YSZ coating microstructure in SPS, using a 3D numerical simulation as a tool to isolate each effect. Four primary parameters are investigated: (1) the particle velocity distribution, (2) the inter-peak distance of substrate asperities, (3) the torch traverse velocity, and (4) the deposition time interval per simulation update ($\Delta t_{rep}$). Each parameter controls a distinct facet of the SPS deposition process:

- Particle velocity distribution (i.e. the in-flight particle speed components) determines the momentum and directionality of impacting droplets, which in turn dictates the mode of layer buildup. Higher particle velocities produce a more collimated, line-of-sight flux of droplets that can "punch through" the surrounding gas and impact the substrate with near-normal incidence;
- The inter-peak distance on the substrate – essentially the spacing between surface asperities – controls initial nucleation sites for these columns. A closely packed peak spacing (fine roughness) means many potential nucleation points, resulting in numerous thin columns or even a quasi-continuous layer with only micro-cracks;
- The torch traverse velocity (spray gun scanning speed) governs the dwell time and material flux on each area of the substrate. At a slow scan speed (long dwell), a large amount of molten material and plasma heat is delivered per unit area, promoting extensive deposit buildup and higher local substrate temperatures;
- Finally, the representative time interval $\Delta t_{rep}$ in the simulations – essentially the time window of particle impacts accumulated before updating the growing film – influences

the apparent structure by controlling temporal resolution. A small $\Delta t_{rep}$ (short time slices) captures the fine-scale column nucleation and growth competition faithfully, whereas a larger $\Delta t_{rep}$ aggregates many sequential impacts at once, effectively smoothing out transient features.

Two different SPS datasets (referred to as Dataset A and Dataset B) are analysed in this chapter to ensure the observed effects are robust under different spray conditions. These datasets correspond to distinct plasma torch settings: Dataset A employs a higher-enthalpy plasma jet (245 slpm Ar–$H_2$ gas at 100 kW, 75 mm stand-off distance) compared to Dataset B (200 slpm Ar–$N_2$–$H_2$ at 90 kW, 100 mm standoff distance). Relative to Dataset B, the more intense, closer-range plume in Dataset A accelerates and heats the suspension droplets more aggressively, so particles arrive hotter and more fully molten on the substrate. By comparing results from these two datasets, the chapter evaluates how differences in plasma gas composition, power, and stand-off distance modulate the influence of each parameter on the coating microstructure. This comparative approach highlights any shifts in behaviour and strengthens the generality of the conclusions.

In the following sections, the effects of each parameter are presented and discussed in turn, with an emphasis on the evolution of coating morphology under varying conditions. Throughout these results, side-by-side comparisons between the Dataset A and Dataset B are made to underline how baseline spray parameters can amplify or mitigate microstructural trends. By providing this contextual analysis, the chapter sets the stage for a comprehensive discussion on optimising SPS process parameters to achieve desired coating structures, bridging modelling insights with established SPS knowledge.

## 4.2 Particle Velocity Distribution

In this section, we study the impact of increasing the velocities of particles on the final coating morphology, i.e. we study how a coating evolves as we raise the rates at which the particles travel. Particles may have many different velocities and, thus, for the purposes of this study, we multiply the x-component, and y-component of each particle velocity by certain factors. Specifically, we use factors of one, two, three, four, five, and ten, represented as (1u, 1v), (2u, 2v), (3u, 3v), (4u, 4v), (5u, 5v), and (10u, 10v) respectively, wherein u, and v are the x-, and y-components of the velocity of any given particle. Figures 4.1 – 4.4 illustrate how the YSZ bondcoat morphology evolves as the in-flight particle velocity distribution increases.

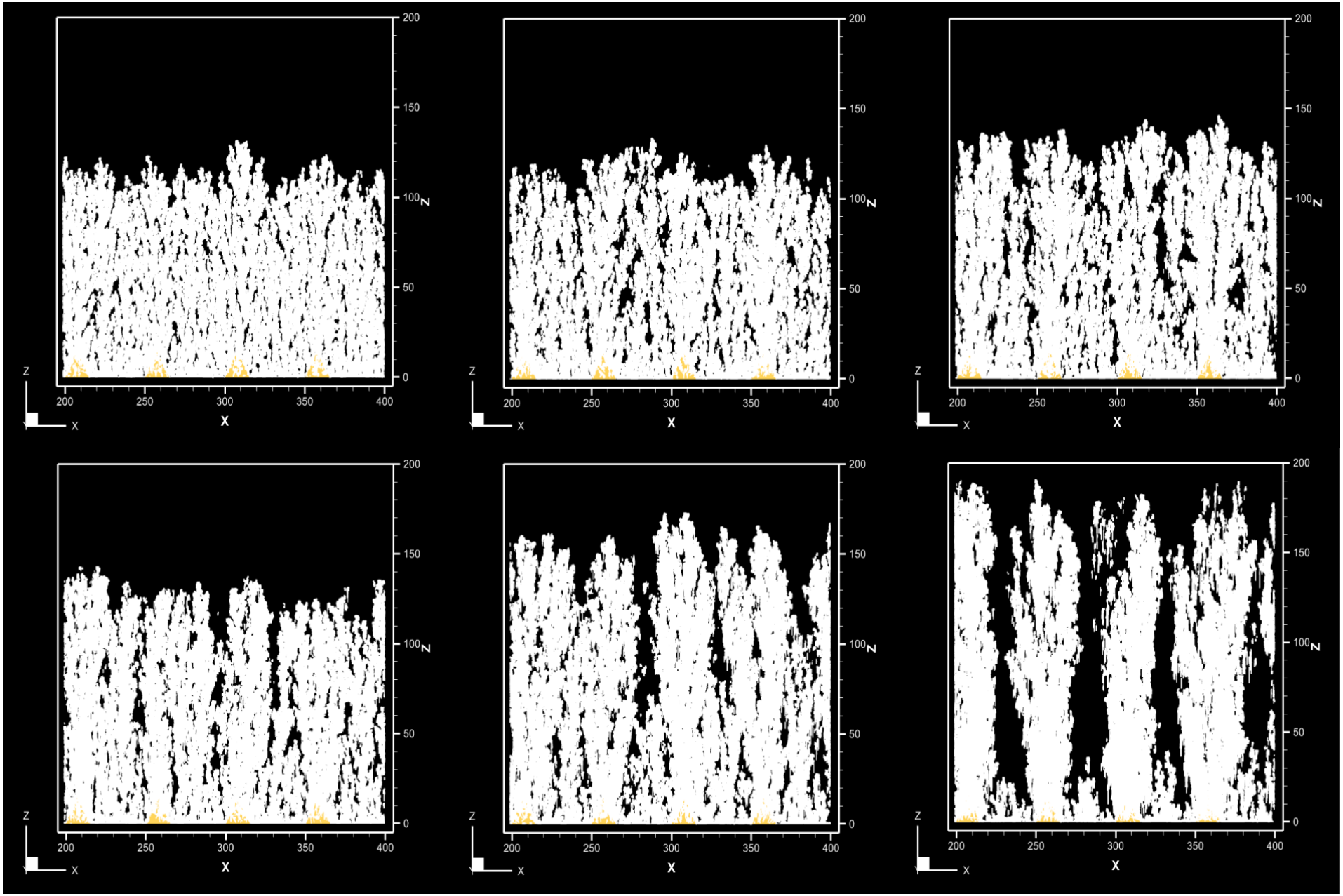


Fig. 4.1 From top, left to right: Surface morphologies of the XZ sections for dataset A with particle distributions of [a] (1u, 1v) $m.s^{-1}$, [b] (2u, 2v) $m.s^{-1}$, [c] (3u, 3v) $m.s^{-1}$, [d] (4u, 4v) $m.s^{-1}$, [e] (5u, 5v) $m.s^{-1}$, and [f] (10u, 10v) $m.s^{-1}$.

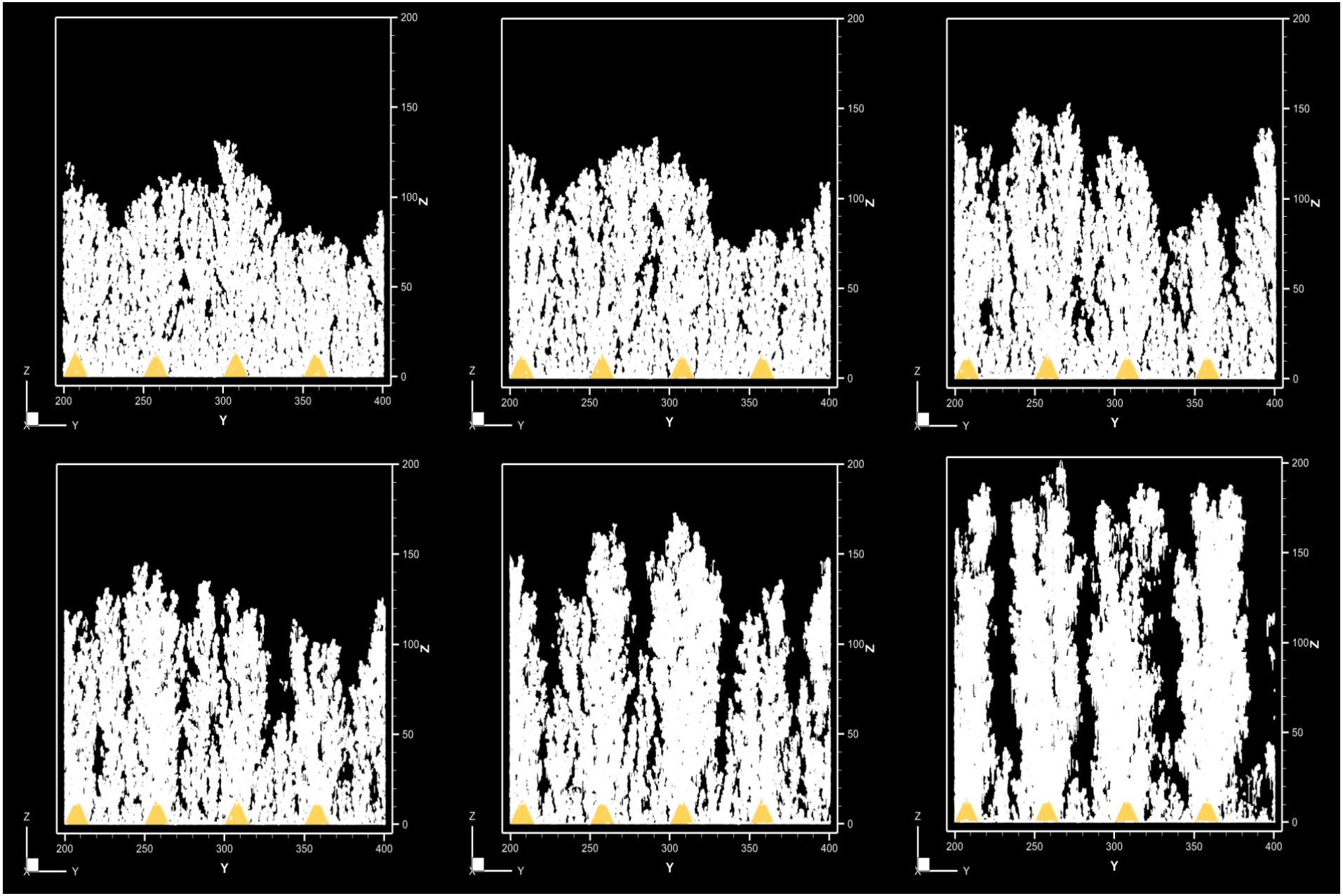


Fig. 4.2 From top, left to right: Surface morphologies of the YZ sections for dataset A with particle distributions of: [a] (1u, 1v) $m.s^{-1}$, [b] (2u, 2v) $m.s^{-1}$, [c] (3u, 3v) $m.s^{-1}$, [d] (4u, 4v) $m.s^{-1}$, [e] (5u, 5v) $m.s^{-1}$, and [f] (10u, 10v) $m.s^{-1}$.

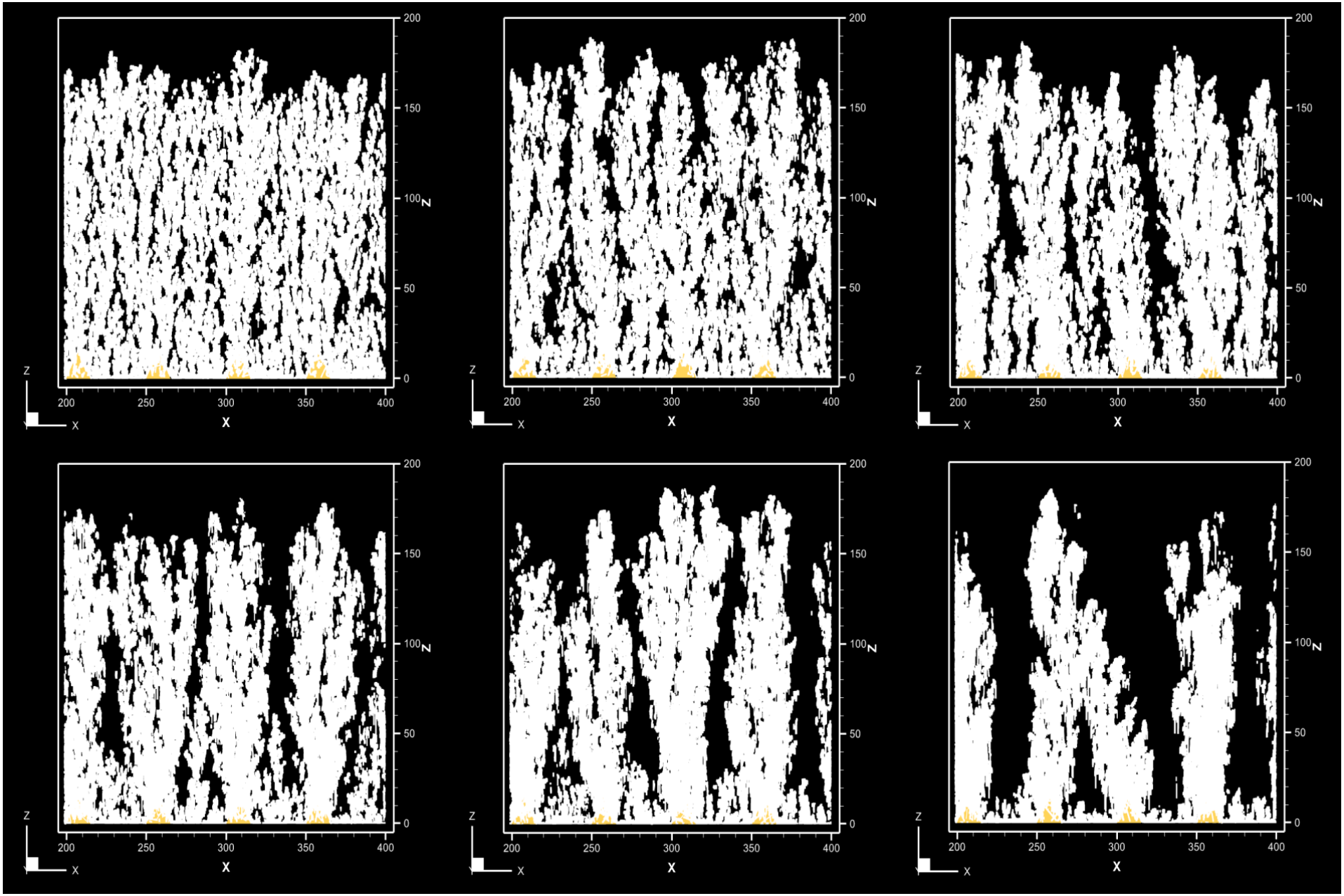


Fig. 4.3 From top, left to right: Surface morphologies of the XZ sections for dataset B with particle distributions of: [a] (1u, 1v) $m.s^{-1}$, [b] (2u, 2v) $m.s^{-1}$, [c] (3u, 3v) $m.s^{-1}$, [d] (4u, 4v) $m.s^{-1}$, [e] (5u, 5v) $m.s^{-1}$, and [f] (10u, 10v) $m.s^{-1}$.

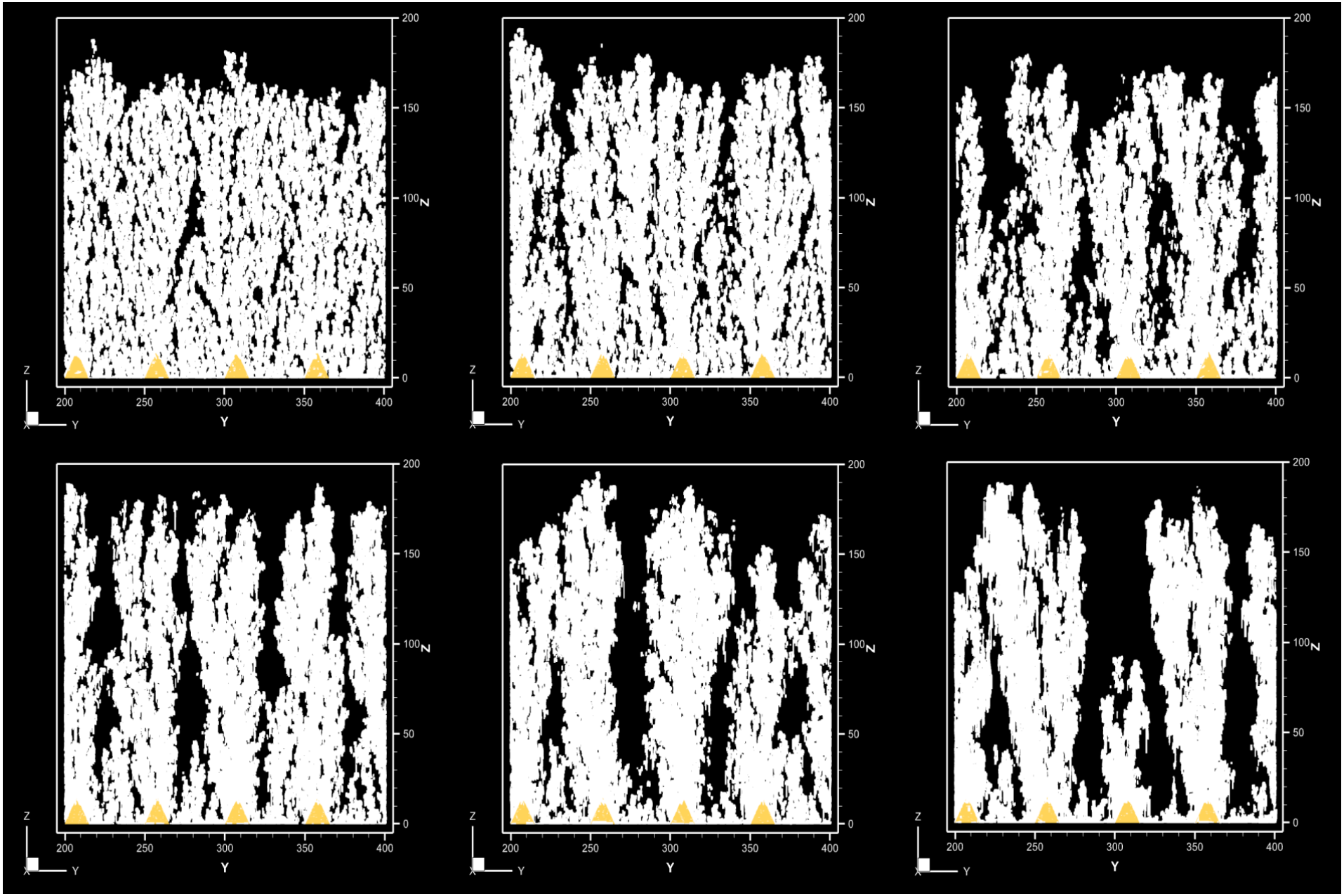


Fig. 4.4 From top, left to right: Surface morphologies of the YZ sections for dataset B with particle distributions of: [a] (1u, 1v) $m.s^{-1}$, [b] (2u, 2v) $m.s^{-1}$, [c] (3u, 3v) $m.s^{-1}$, [d] (4u, 4v) $m.s^{-1}$, [e] (5u, 5v) $m.s^{-1}$, and [f] (10u, 10v) $m.s^{-1}$.

Increasing the particle velocity in an axial suspension plasma spray has a pronounced impact on coating growth mechanisms, promoting a transition from a mixed/lamellar morphology toward a columnar architecture. In the given Axial III SPS conditions, a tenfold boost in particle speed effectively makes deposition more line-of-sight and directional. High-velocity particles carry greater momentum normal to the substrate, enabling them to punch through the decelerating plasma gas near the surface. This directed flux means that impacting droplets tend to hit substrate asperities head-on with less lateral dispersion. The result is an enhanced "shadowing effect," where growing protrusions shield neighbouring areas from incoming particles. Consequently, material preferentially accumulates into separated vertical growths (columns) instead of forming a continuous lamella, leaving characteristic inter-columnar gaps. In essence, faster particles deposit in a more beam-like fashion, laying down columnar features much like a vapor-jet process, rather than the spread-out splats of a slower spray. The influence of particle velocity is intimately tied to particle size, and phase state upon impact. Higher injection speeds promote more vigorous droplet atomisation, producing finer particle fragments that arrive at the substrate. These sub-micron particles possess low inertia (Stokes numbers $\ll 1$), so they are easily diverted by the plasma flow in the near-surface boundary layer. Instead of impinging perpendicularly and fully flattening, they tend to glide in at shallow angles while still molten or semi-molten. Such glancing impacts, combined with rapid solidification of the tiny droplets, mean that particles "stick" atop surface high points without spreading far, building up columnar deposits layer by layer. By contrast, larger or slower particles with higher momentum strike more orthogonally and form wide splats, filling in valleys and yielding a dense lamellar structure. The net outcome is that elevating the particle impact velocity biases the SPS process toward the columnar growth mode observed in the XZ/YZ cross-sections. This explanation is supported by numerical models and simulations: for example, Saito et al. (2018) found that only particles above a critical velocity (achieved at higher plasma currents) could overcome gas entrainment and deposit centrally, whereas slower ones were deflected away. Likewise, Monte Carlo–type coating simulations capture column formation when particle flux is strongly directional, invoking the same shadowing and asperity-catching mechanism (Azar 2018).

In summary, increasing particle velocity in axial SPS intensifies the kinetic and geometric conditions (high momentum normal impacts, fine droplet fragmentation, and shallow-angle deposition) that favour columnar microstructure development. At low velocities, particles arrive at the substrate with insufficient momentum and increased lateral dispersion, leading to a more isotropic deposition, and filled-in valleys — characteristic of

a denser, splat-dominated structure. However, with increasing particle velocities, the impinging droplets strike the substrate more directionally, enhancing normal impact momentum and reducing spread. This beam-like deposition promotes the "shadowing effect," whereby protrusions on the substrate surface capture incoming particles, shielding adjacent valleys and leading to vertically segregated growth. The columns produced under these high-velocity conditions are marked by well-separated, strain-tolerant feathery structures, akin in form to EB-PVD TBCs, confirming that careful control of in-flight particle dynamics can tailor the coating morphology as desired. Thus, controlled modulation of particle velocity and its distribution directly governs the evolution of columnar microstructures in SPS, offering a tuneable pathway to optimise thermal barrier coatings for desired performance attributes.

## 4.3 Interpeak Distances of Substrate Asperities

In this section, we study the influence of increasing the distances between subsequent peaks of asperities on the resulting coating microstructure, i.e. we examine how a coating evolves as we reduce the roughness of a substrate. For this study, we raise the interpeak distances of surface asperities across 5 μm, 15 μm, 25 μm, 35 μm, 50 μm, and infinity, wherein an interpeak distance of infinity signifies a smooth surface with no asperities. Figures 4.5 – 4.8 illustrate how the YSZ coating microstructure evolves as the interpeak distance between consecutive asperities increases.

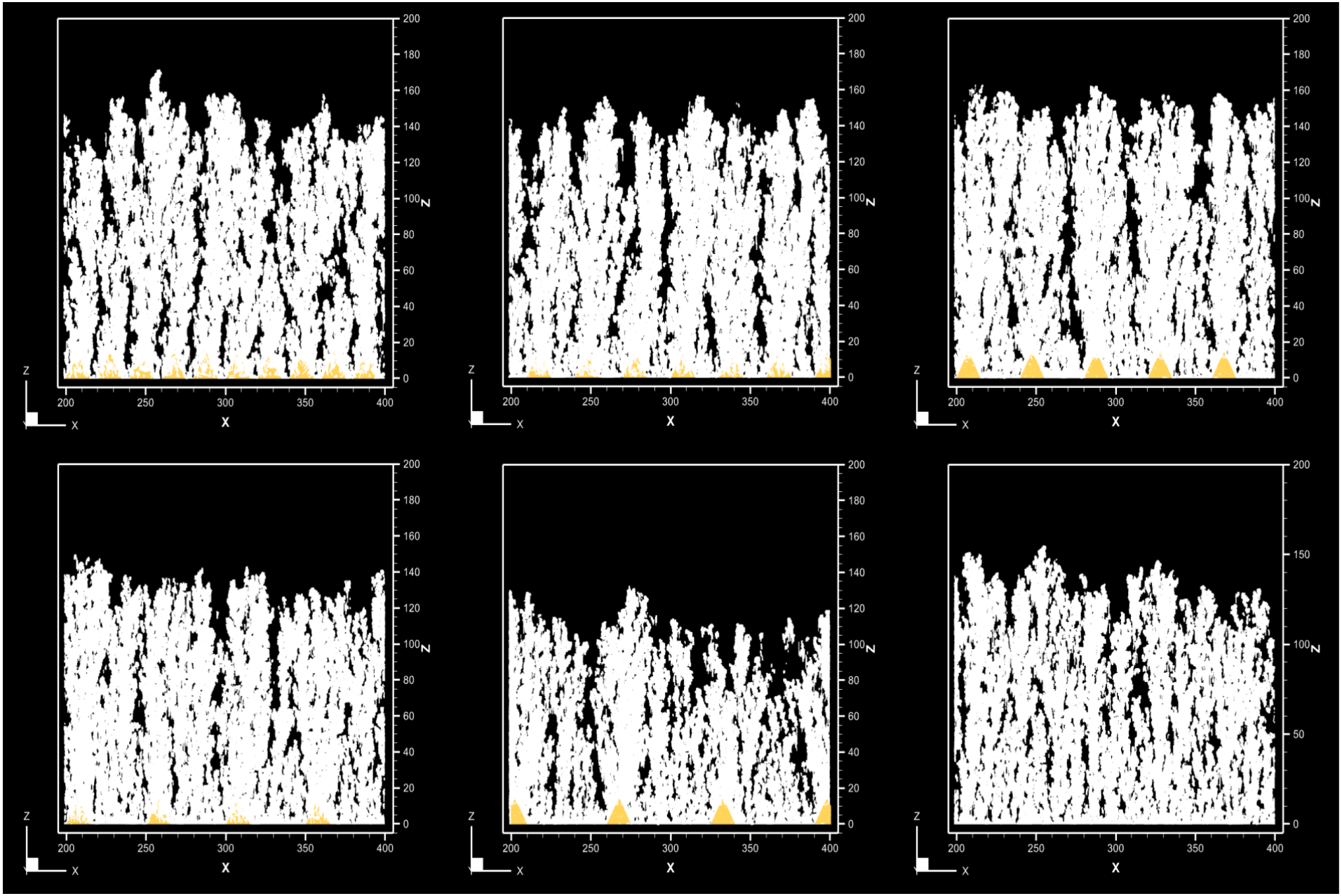


Fig. 4.5 From top, left to right: Surface morphologies of the XZ sections for dataset A with interpeak distances of [a] 5 μm, [b] 15 μm, [c] 25 μm, [d] 35 μm, [e] 50 μm, and [f] a smooth substrate.

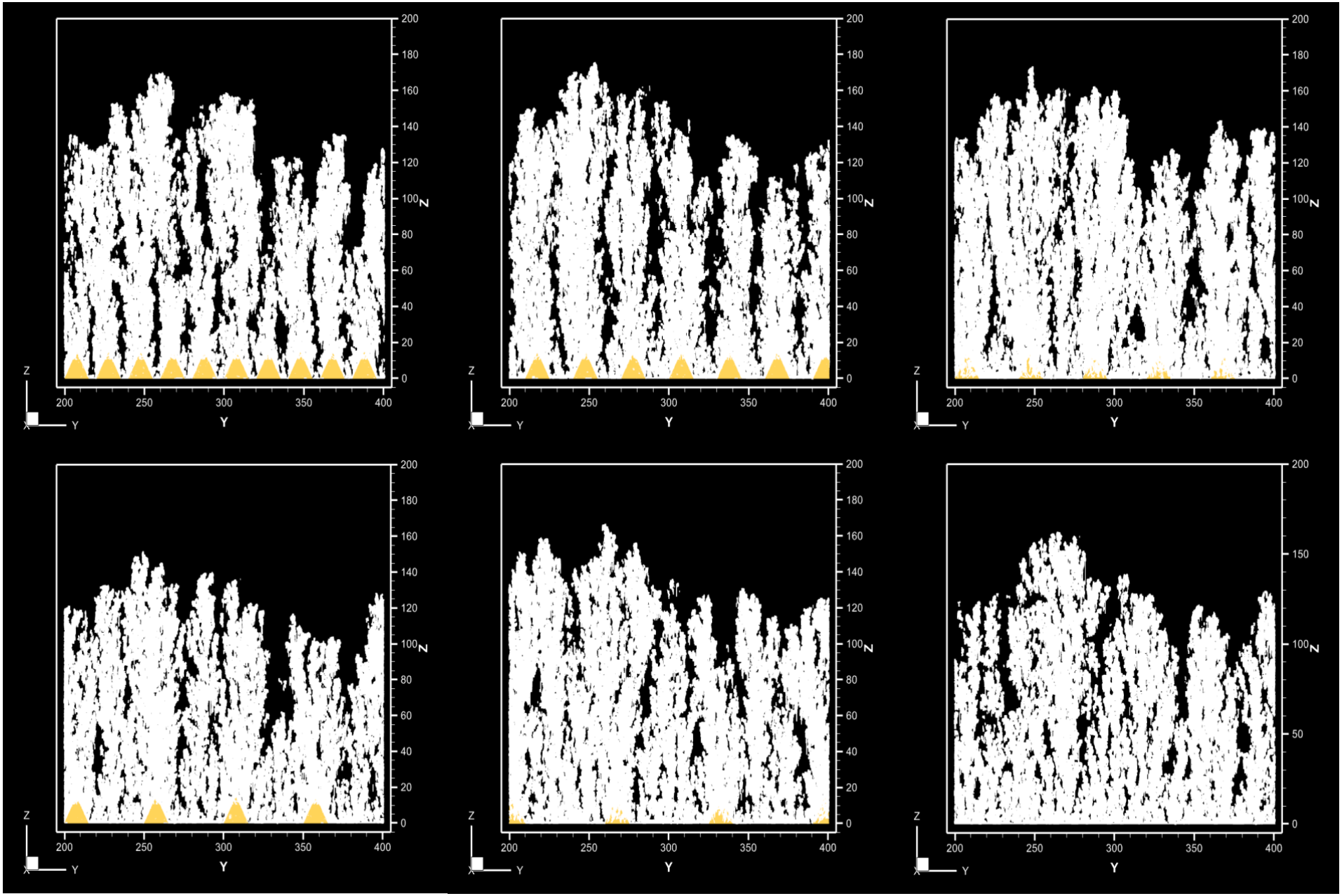


Fig. 4.6 From top, left to right: Surface morphologies of the YZ sections for dataset A with interpeak distances of [a] 5 μm, [b] 15 μm, [c] 25 μm, [d] 35 μm, [e] 50 μm, and [f] a smooth substrate.

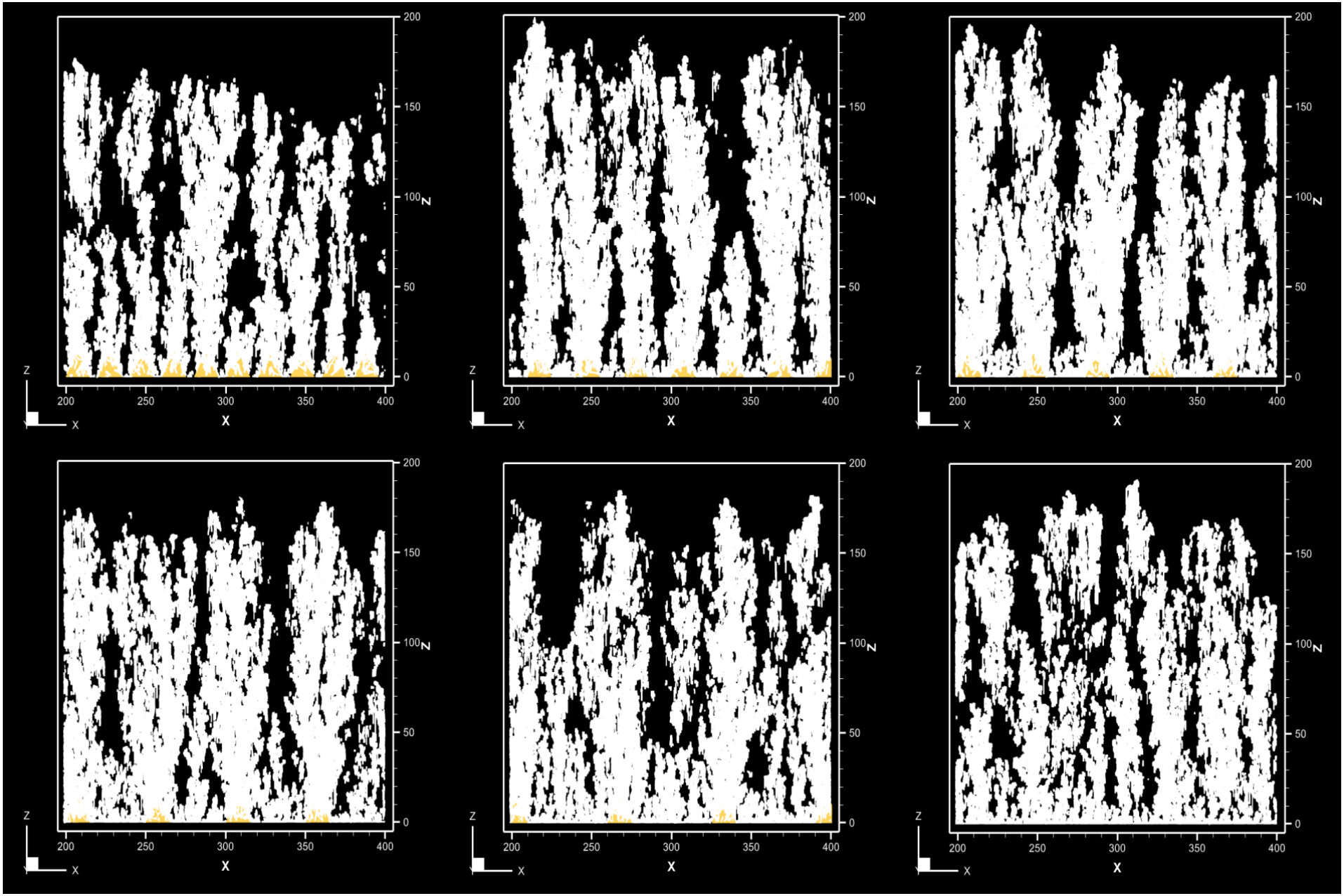


Fig. 4.7 From top, left to right: Surface morphologies of the XZ sections for dataset B with interpeak distances of [a] 5 μm, [b] 15 μm, [c] 25 μm, [d] 35 μm, [e] 50 μm, and [f] a smooth substrate.

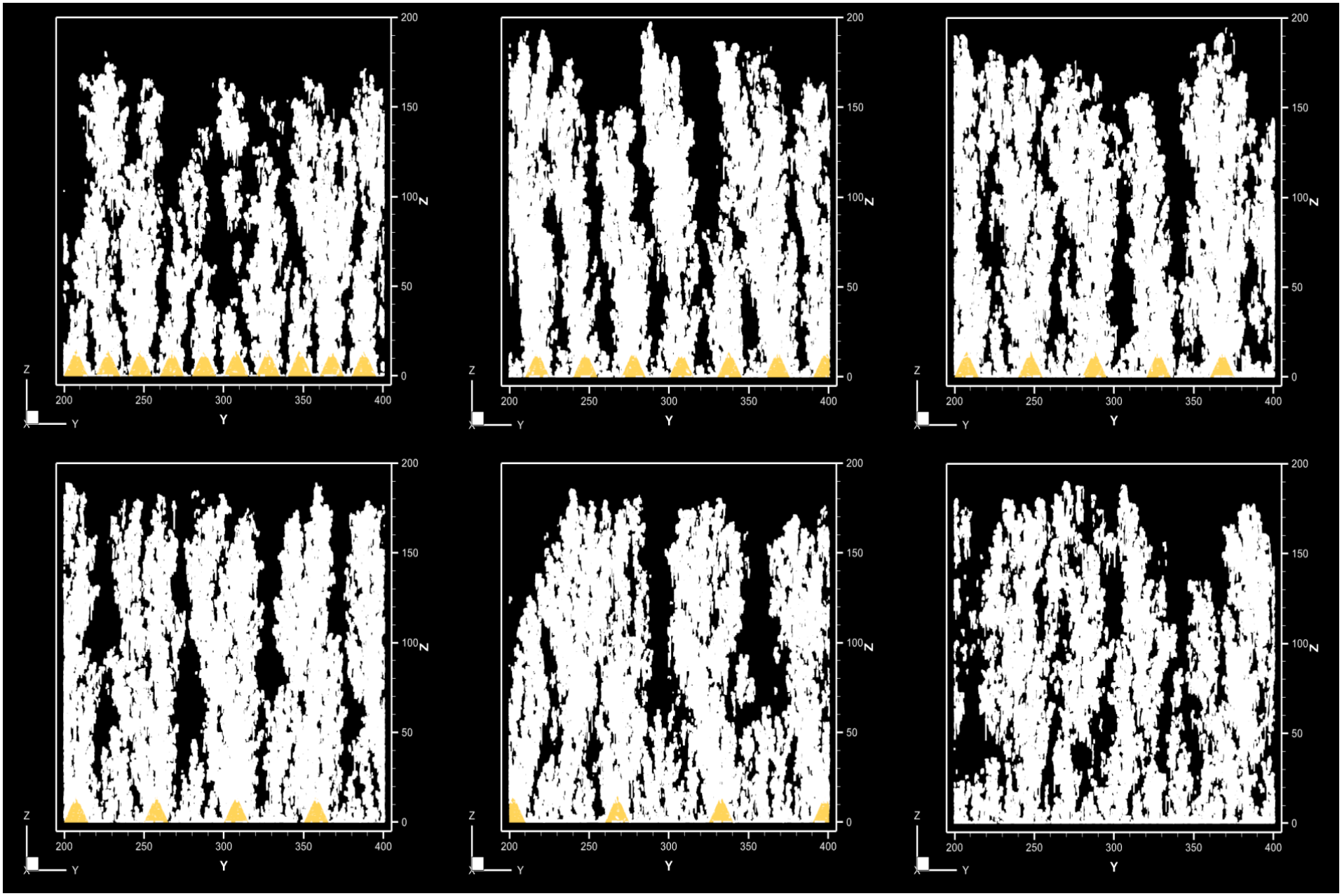


Fig. 4.8 From top, left to right: Surface morphologies of the YZ sections for dataset B with interpeak distances of [a] 5 μm, [b] 15 μm, [c] 25 μm, [d] 35 μm, [e] 50 μm, and [f] a smooth substrate.

Both Datasets A and B exhibit the same qualitative trend: as the inter-peak distance (asperity spacing) of the substrate increases, the SPS microstructure evolves from a relatively uniform, planar deposit toward a highly segmented, columnar architecture. At the smallest spacing (5 μm, or effectively smooth substrate), the coating initially forms many narrow, closely spaced columns. When the spacing increases to intermediate values (15–25 μm), moderate-size columns form atop peaks while modest voids appear between them. At the largest spacings (35–50 μm), the coating breaks up into a few well-defined, thick columns centered on each asperity, leaving broad inter-columnar void channels in the valleys. In other words, higher peak-to-peak distances yield larger column width, whereas closely spaced asperities produce many thin columns. This progression is driven by the shadowing effect: elevated peaks intercept incoming particles and shield their surroundings, so deposition concentrates on the crests and starves the valleys.

It is also important to note that Dataset A's high-energy spray conditions produce a fundamentally different coating morphology than Dataset B's milder settings. The Dataset A torch (100 kW, 245 slpm, 80% Ar – 20% $H_2$, 75 mm stand-off distance) creates a hotter, faster jet that breaks suspension droplets into finer fully-molten splats. As a result, Dataset A coatings develop a much finer, denser columnar network for every peak spacing tested. By contrast, Dataset B's weaker plume (90 kW, 200 slpm, 75% Ar – 10% $N_2$ – 15% $H_2$, 100 mm stand-off distance) often produced fewer columns and even lamellar layers on smooth regions. Thus, even small asperities drove column formation under Dataset A but were largely ignored by Dataset B's cooler jet. Moreover, because Dataset A fully melts most droplets, these columns contain almost no inherent microporosity; nearly all the porosity resides between columns as large vertical voids. In contrast, Dataset B's columns – when they form – contain more unresolved particles and small cracks inside them due to cooler splats. This reflects the underlying spray physics: Dataset A's intense jet creates vigorous shadowing even on moderate topography, whereas Dataset B's gentler, longer-flight plume only segments the coating strongly when the interpeak distances are large.

Mechanistically, these differences stem from the altered process parameters. Dataset A's higher plasma power and 20% $H_2$ content create a hotter, more focused flame with greater thermal flux; the shorter 75 mm stand-off also reduces quenching, so particles arrive hotter and more molten. This combination drives the spray into a "high-velocity" regime: particles have high inertia normal to the surface, so deposition is beam-like and less sensitive to topography. In contrast, Dataset B's lower power, $N_2$-diluted jet and 100 mm stand-off produce more cooling and a wider, cooler plume. Many droplets solidify partially

before impact, enhancing classic SPS shadowing: only peaks catch splats, and inter-peak valleys fill slowly. Ultimately, Dataset A's conditions bias the coating toward a dense, fine-columnar architecture with low intrinsic porosity, whereas Dataset B remains in a shadowing-dominated mode, yielding coarser, more porous columns.

In summary, despite differences in spray power and gas flow between Dataset A and Dataset B, the two datasets show consistent trends with substrate spacing: higher inter-peak distance yields fewer, larger columns with more open porosity, while smaller spacing gives many fine columns and a denser coating. The underlying shadowing mechanism and requirement for peak-based anchoring are the same in both cases, leading to comparable microstructural transitions and adhesion behaviour in the XZ and YZ cross-sections.

These insights guide process selection. In practice, tailoring interpeak distance and spray parameters allows one to "dial in" the desired morphology. Dataset A's conditions inherently favour a highly segmented columnar microstructure with abundant inter-column porosity – ideal for thermal barrier coatings, whereas Dataset B's conditions favour a more compact, lamellar-like coating – potentially better for erosion resistance or stiffness. Ensuring a sufficiently rough substrate for good adhesion, while choosing appropriate parameters will yield the target balance of columnarity, density, and durability.

## 4.4 Spray Gun Traverse Velocity

In this section, we study the effects of increasing the velocity of the plasma torch on the resultant coating morphology, i.e. we examine how a coating evolves as we raise the rates at which the torch traverses the substrate. For this study, we multiply the x-component, and y-component of the torch velocity by factors of one, two, four, eight, sixteen, and thirty-two, represented by 1 $m.s^{-1}$, 2 $m.s^{-1}$, 4 $m.s^{-1}$, 8 $m.s^{-1}$, 16 $m.s^{-1}$, and 32 $m.s^{-1}$ respectively. Figures 4.9 – 4.12 illustrate how the YSZ coating buildup evolves as gun velocity increases.

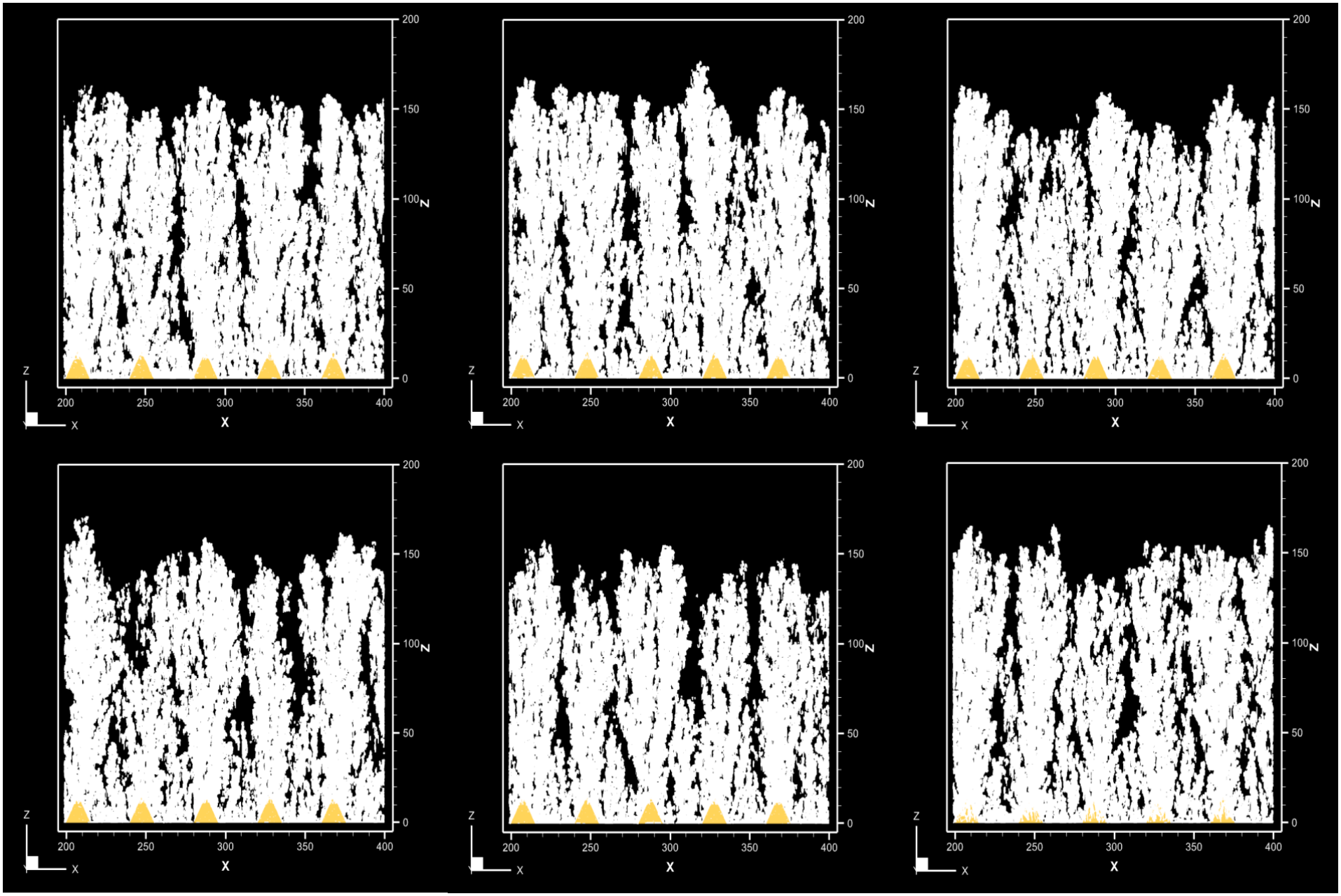


Fig. 4.9 From top, left to right: Surface morphologies of the XZ sections for dataset A with torch velocities of [a] 1 $m.s^{-1}$, [b] 2 $m.s^{-1}$, [c] 4 $m.s^{-1}$, [d] 8 $m.s^{-1}$, [e] 16 $m.s^{-1}$, and [f] 32 $m.s^{-1}$.

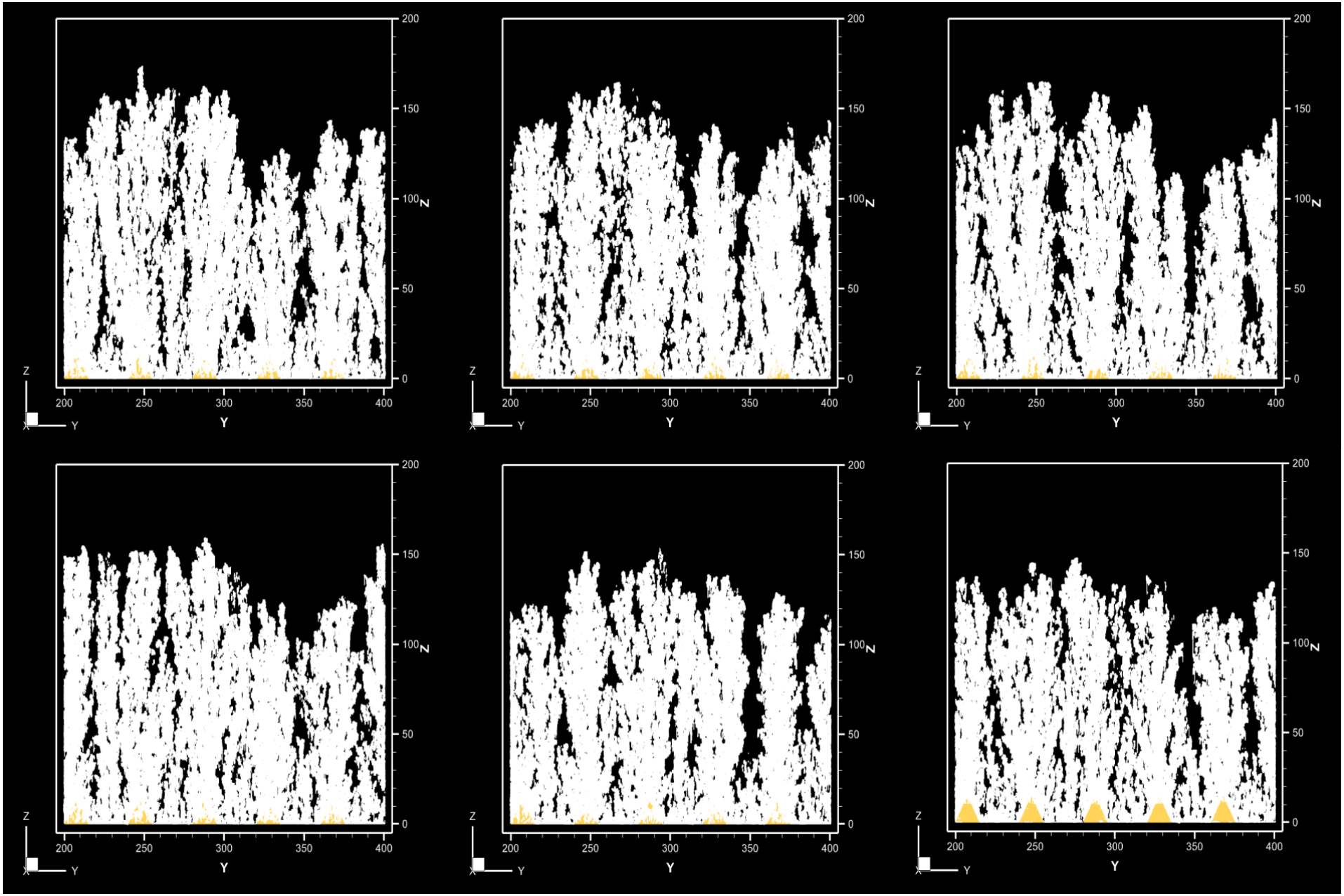


Fig. 4.10 From top, left to right: Surface morphologies of the YZ sections for dataset A with torch velocities of [a] 1 $m.s^{-1}$, [b] 2 $m.s^{-1}$, [c] 4 $m.s^{-1}$, [d] 8 $m.s^{-1}$, [e] 16 $m.s^{-1}$, and [f] 32 $m.s^{-1}$.

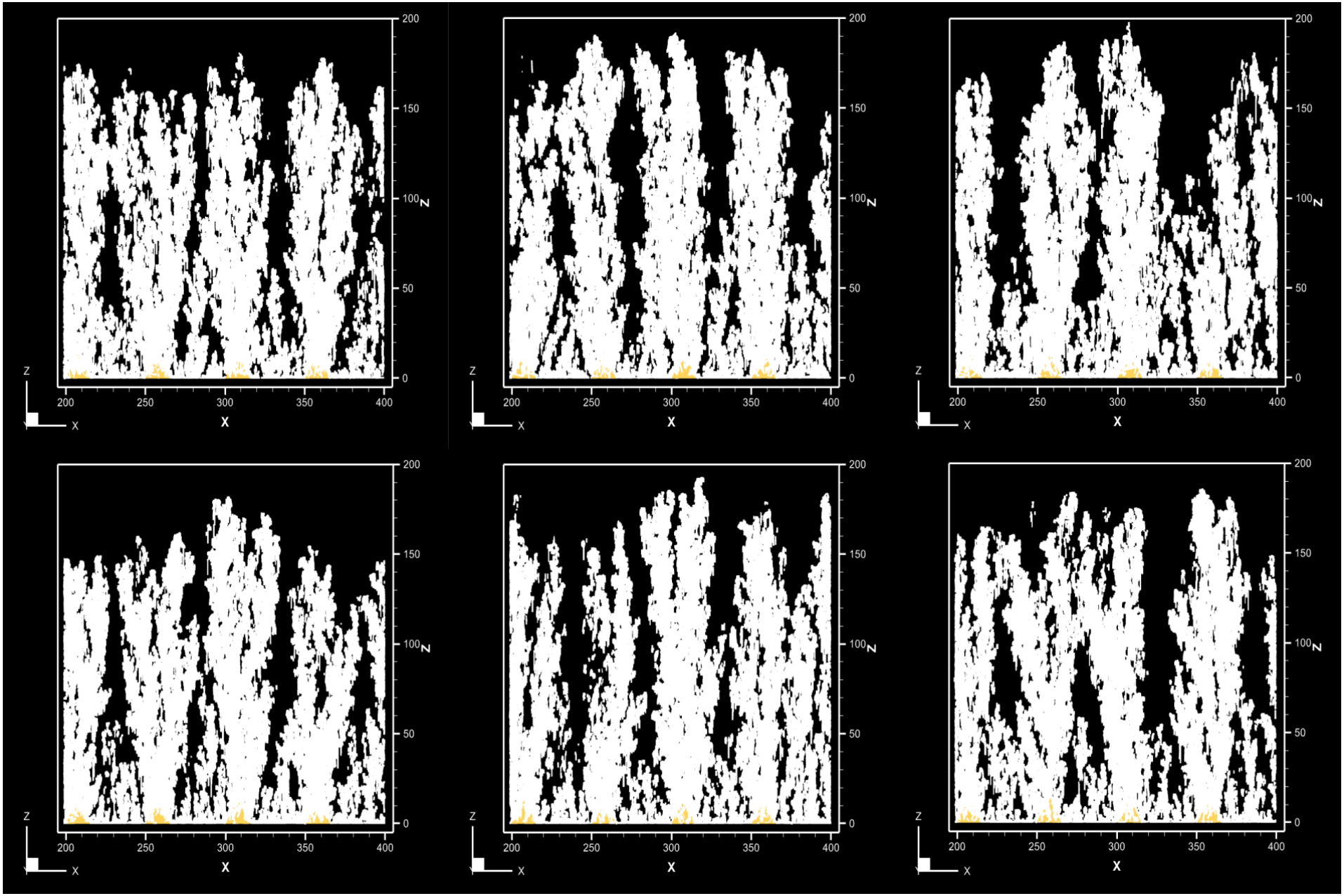


Fig. 4.11 From top, left to right: Surface morphologies of the XZ sections for dataset B with torch velocities of [a] 1 $m.s^{-1}$, [b] 2 $m.s^{-1}$, [c] 4 $m.s^{-1}$, [d] 8 $m.s^{-1}$, [e] 16 $m.s^{-1}$, and [f] 32 $m.s^{-1}$.

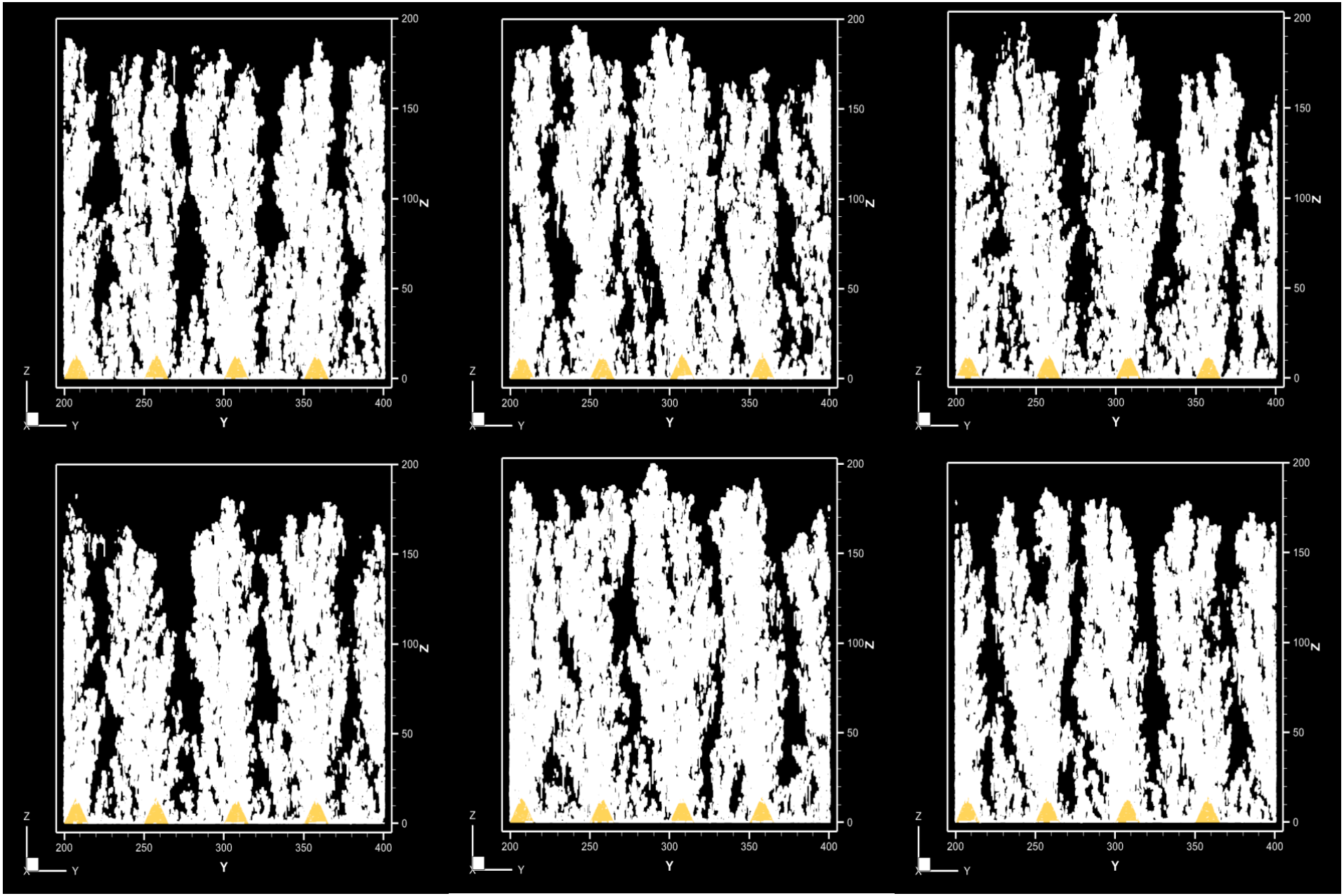


Fig. 4.12 From top, left to right: Surface morphologies of the YZ sections for dataset B with torch velocities of [a] 1 m.s$^{-1}$, [b] 2 m.s$^{-1}$, [c] 4 m.s$^{-1}$, [d] 8 m.s$^{-1}$, [e] 16 m.s$^{-1}$, and [f] 32 m.s$^{-1}$.

Both the Dataset A and Dataset B exhibit consistent trends in response to torch translation speed. As the torch scan rate increases (from 1 μm/μs through 32 μm/μs), the plasma jet and resulting coating evolve in similar ways in both cases. Particularly, faster traverse speeds stretch and weaken the jet, reducing the time the plasma and particles spend over any given area, whereas slower speeds concentrate the plume and increase local dwell time. In both datasets, the fine suspension droplets (which have low Stokes numbers) closely follow the plasma flow. As torch speed increases, the reduced residence time means many particles spend less time near the hot core and more time entrained in the spreading plume. The torch motion effectively adds a lateral component to the flow: particles tend to be carried forward by the moving jet, broadening the impact footprint. Both simulations show that at high speed, fewer particles solidify in flight or deposit behind the leading edge, so the resulting particle flux is more uniform across the scan. In contrast, at slow speeds the plasma "pours" more vertically onto one spot, and the classic shadowing effect becomes pronounced: fine droplets are deflected around asperities or early splats, building up thick columns on peaks. Importantly, because torch motion influences the flow everywhere, the relative effect of these particle–plume interactions remain similar: increased scan speed always shortens the flow–particle coupling time and spreads material more thinly, while slow scans always allow maximal heating and particle concentration at local spots.

The coating microstructure reflects these shared mechanics. Both Datasets A and B show that fast torch scans produce finer, more uniform coatings with higher porosity, whereas slow scans produce thicker, denser coatings with pronounced columnar/dendritic features. For example, as torch speed increases, both cases transition from heavy, high-relief columnar build-up to a thin, evenly covered layer with many fine columns and larger intercolumn gaps. Conversely, at the slowest speed (1 μm/μs), each pass deposits a large mass of molten material and heat, causing broad lamellae that later crack vertically (producing large columnar blocks). In both datasets, this yields low overall porosity (because splats coalesce) but poor thickness uniformity (with obvious ridges and layer lines). As torch speed increases, the per-pass deposit thins and splats cool faster, so coatings become more porous and planar. Both analyses concur that increasing torch velocity enhances columnar segmentation (more, narrower columns) and raises porosity, while slowing the torch yields a nearly continuous lamellar layer that only cracks to relieve stress. This is why, despite differences in their plasma power and gas composition, Dataset A and Dataset B share the same qualitative trend: slow scans give heavy, dense deposits (with later vertical cracks) and fast scans give sparse, fine-columnar deposits.

It is also imperative to note that Dataset A consistently produces denser, finer-columnar coatings than Dataset B, because the former's plasma is much hotter, and energetic. Dataset A's torch runs at 100 kW with pure Ar–$H_2$ at a 75 mm stand-off, whereas Dataset B uses 90 kW with a diluted Ar–$N_2$–$H_2$ mix at a 100 mm standoff. The higher gas flow and hydrogen content in Dataset A raise the plasma enthalpy and jet velocity, so particles arrive hotter, more molten, and with greater momentum. By contrast, Dataset B's cooler, broader plume (weaker power and $N_2$ dilution) decelerates particles more. Mechanistically, this means that even at high torch speeds Dataset A's particles remain fully molten and travel nearly normal to the substrate, whereas Dataset B's particles slow and begin to shadow and stack as columns. At slow traverse (~1 μm/μs), both setups deposit thick layers, but Dataset A's film is almost fully molten and can develop fine vertical cracks from thermal stress, whereas Dataset B builds broader columns with large voids. The strong heating in Dataset A leads to dense splat stacks with only micro-cracks, whereas Dataset B shows "cauliflower" columns and clear inter-column gaps. As speed increases (towards 32 μm/μs), Dataset A still yields appreciable thickness and mostly filled microstructure, thanks to its focused jet, whereas Dataset B's coating thins out dramatically and becomes highly porous. In effect, column density remains high in Dataset A (many fine columns) even at fast scans, but in Dataset B the columns thin and gaps widen.

In summary, both Dataset A and Dataset B exhibit the same fundamental response to torch velocity: slow torch speeds concentrate the plasma and particles, producing thick, dense deposits with strong columnar structure, whereas fast speeds stretch the jet and spread out the spray, yielding thinner, more uniform (yet more porous) coatings. These common trends – jet stretching, momentum redistribution by the moving torch, and variation of local residence time – underlie the coating outcomes in both cases, demonstrating that torch translation speed is a key control on the balance between columnar growth and planar filling in SPS. However, the torch-speed sensitivities of Datasets A and B stem directly from their process parameters. Dataset A's combination of higher power, hydrogen-rich gas, and short stand-off accelerates and heats particles to a greater degree, so the deposition remains energetic even under fast scans. By contrast, Dataset B's lower-enthalpy, nitrogen-diluted plume loses heat and momentum quickly with distance, so its coating morphology is highly sensitive to scan rate: fast traverses starve the coating of heat and material, while only very slow traverses allow enough buildup.

Thus, torch velocity is a powerful lever for SPS morphology. Balancing torch speed with plasma power, gas mix, and stand-off distance is essential to optimise deposition efficiency and coating quality:

- Use slower torch speeds for thick, low-porosity coatings – Lower traverse speeds dramatically increase material deposition per pass. This yields dense, well-bonded columnar layers;
- Use faster torch speeds for thinner, finer coatings – Higher traverse speeds shorten dwell time, thinning the deposit and cooling the substrate. This can improve adhesion via compressive stress, but increases porosity;
- Adjust plasma gas, and power to suit speed – A $H_2$-rich plasma boosts heat transfer, supporting higher torch speeds without loss of density. Conversely, if using slow scans, a small reduction in power can prevent overmelting;
- Optimise stand-off distance – Shorten the stand-off to keep particles hot upon impact and lengthen the stand-off to dissipate heat.

By strategically balancing torch velocity with plasma parameters, one can tailor deposition efficiency and microstructure.

## 4.5 Database Representative Time

In this section, we study the role of increasing the database representative time on the final coating microstructure, i.e. we explore how a coating evolves as we increase $\Delta t_{rep}$ values. For this study, we raise the representative times across 400 μs, 800 μs, 1200 μs, 1600 μs, and 2000 μs for the stronger Dataset A and across 200 μs, 400 μs, 600 μs, and 800 μs for the weaker Dataset B. Figures 4.13 – 4.16 illustrate how the YSZ coating morphology evolves as the database representative time increases.

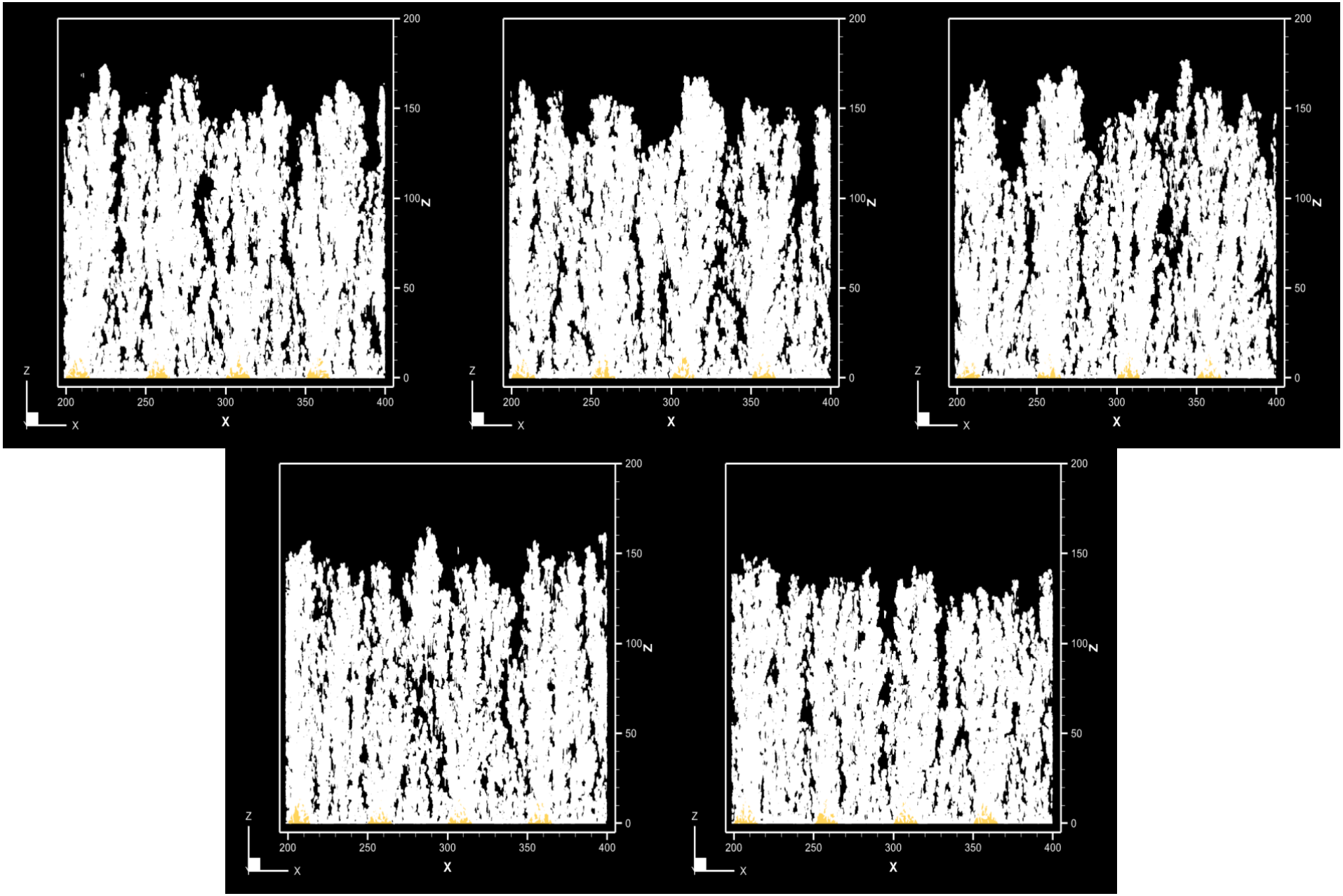


Fig. 4.13 From top, left to right: Surface morphologies of the XZ sections for dataset A with database representative times of [a] 400 μs, [b] 800 μs, [c] 1200 μs, [d] 1600 μs, and [e] 2000 μs.

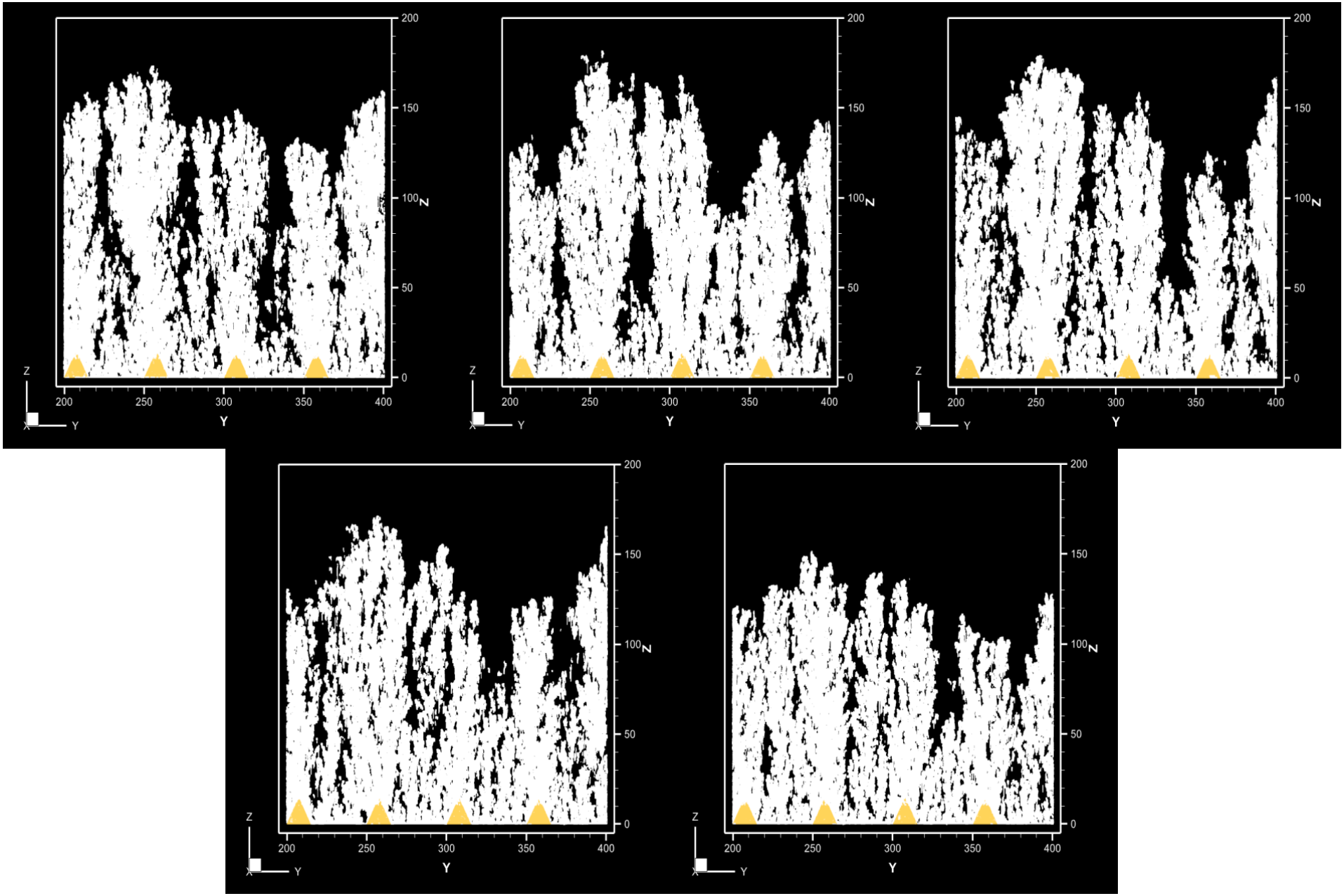


Fig. 4.14 From top, left to right: Surface morphologies of the YZ sections for dataset A with database representative times of [a] 400 μs, [b] 800 μs, [c] 1200 μs, [d] 1600 μs, and [e] 2000 μs.

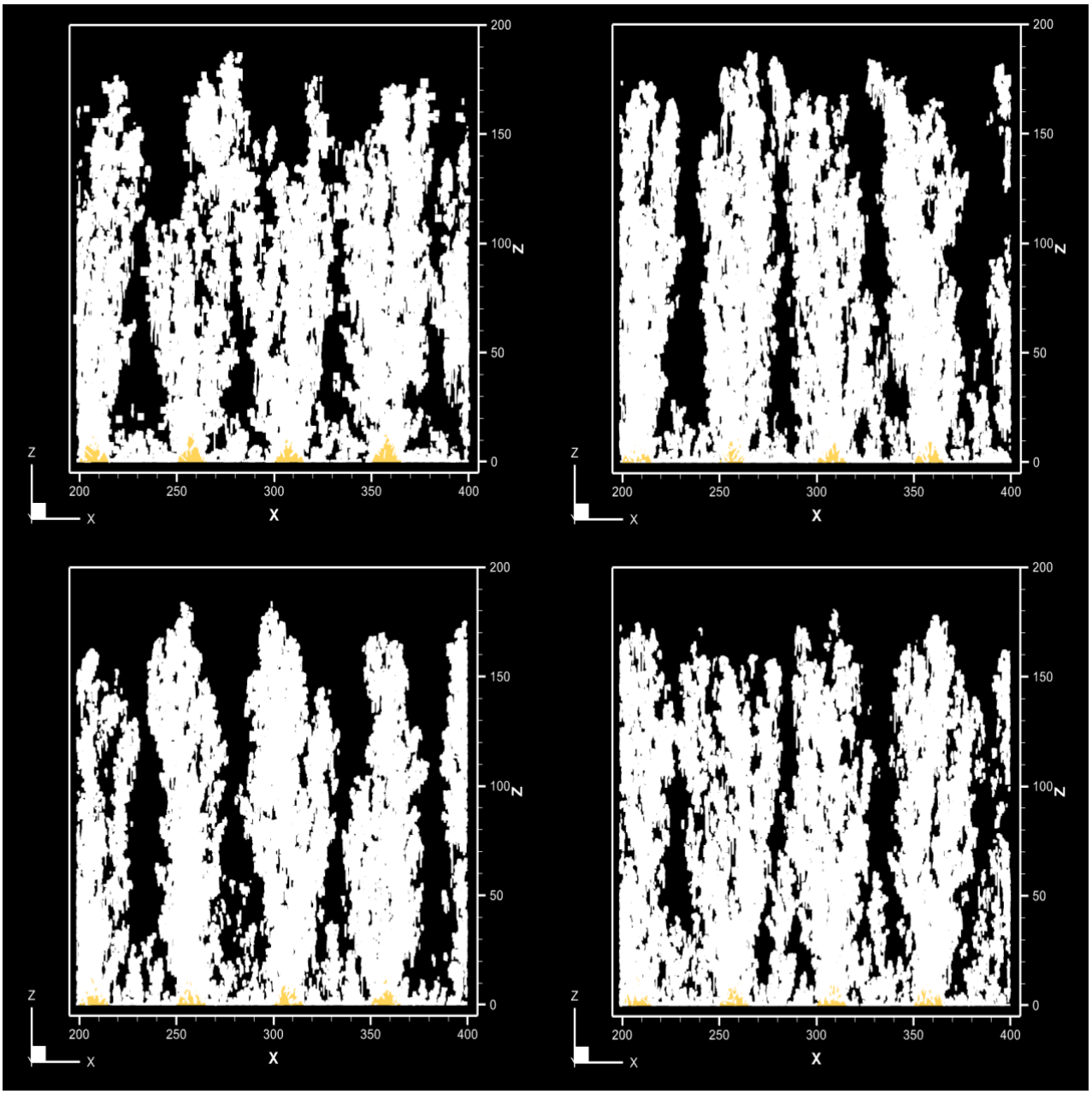


Fig. 4.15 From top, left to right: Surface morphologies of the XZ sections for dataset B with database representative times of [a] 200 μs, [b] 400 μs, [c] 600 μs, and [d] 800 μs.

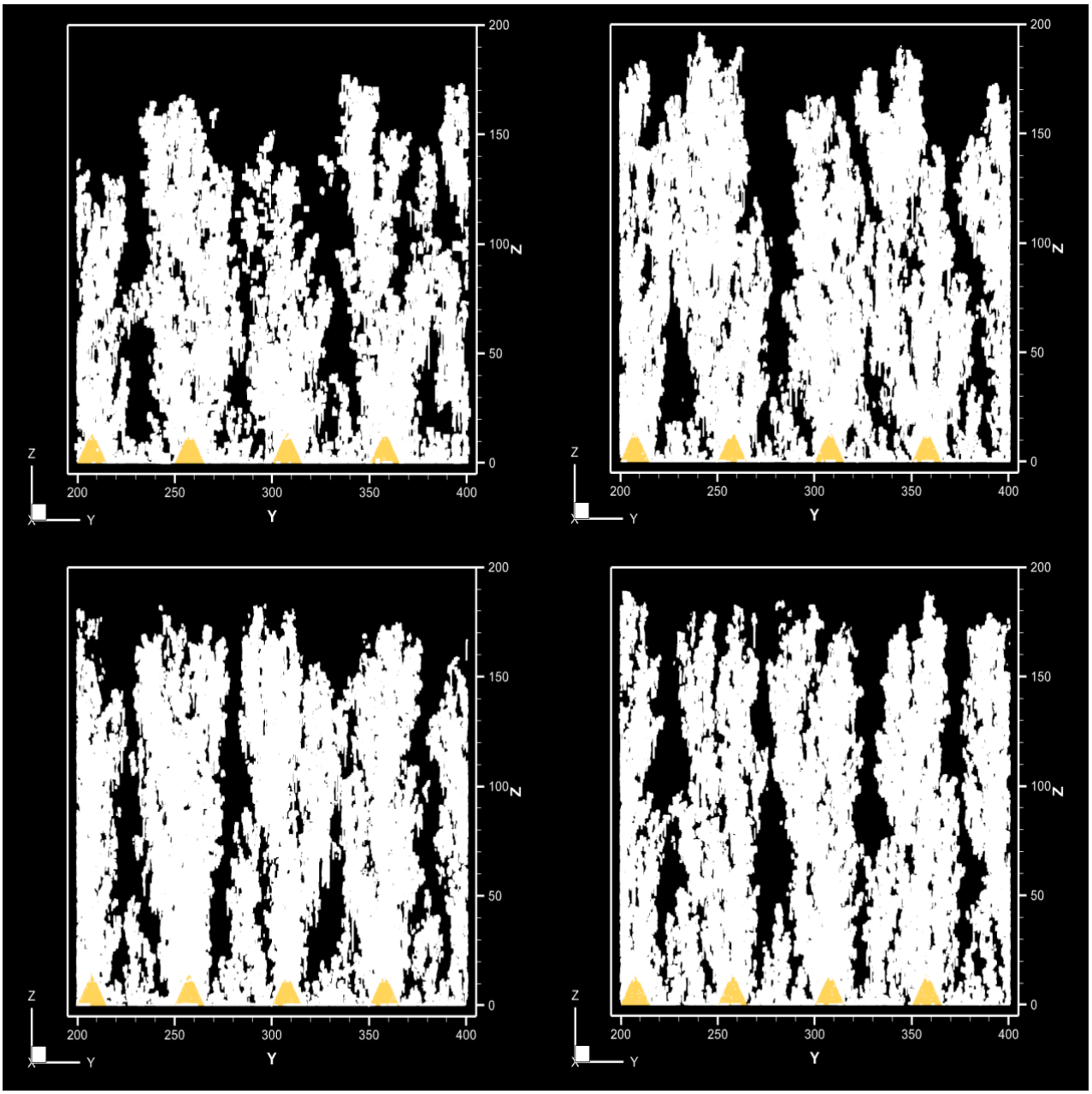


Fig. 4.16 From top, left to right: Surface morphologies of the YZ sections for dataset B with database representative times of [a] 200 μs, [b] 400 μs, [c] 600 μs, and [d] 800 μs.

Across both Datasets A and B, when $\Delta t_{rep}$ is small, i.e. when passes occur in rapid succession, the coating develops a highly segmented, columnar architecture with clear inter-column gaps. For example, at $\Delta t_{rep}$= 400 μs (Dataset A), the simulated coating shows fewer, thicker columns, whereas at $\Delta t_{rep}$= 2000 μs, it shows multiple, thinner columns. Likewise, at $\Delta t_{rep}$= 200 μs (Dataset B), the deposit is a network of thick columns with broad inter-columnar gaps, but at $\Delta t_{rep}$= 800 μs, though columns remain thick, we can also see some narrower, shorter columns emerging from between them.

In real-life scenarios, with short $\Delta t_{rep}$, subsequent spray passes land on a still-hot surface, so the substrate and existing deposit are reheated and heat accumulates between passes. This interpass heat accumulation effectively anneals the coating: adjacent splats and column segments undergo sintering and enhanced interlamellar bonding. Conversely, a long $\Delta t_{rep}$ allows the coating to cool significantly between passes. Each new splat arrives onto a relatively cold substrate, so heat is dissipated and the material solidifies almost independently. This cooling interval limits sintering: splats bond only as much as typical ambient cooling allows, and many small pores remain.

It is also essential to note that Dataset A's operating parameters produce a much hotter, higher enthalpy plume than those of Dataset B. With 100 kW power, 80% Ar – 20% $H_2$ gas and a short 75 mm stand-off, Dataset A delivers intense heat flux to the coating. In practice this means each pass deposits very hot, molten droplets and deposits substantial thermal energy, rapidly raising substrate temperature. By contrast, Dataset B's 90 kW 75% Ar – 10% $N_2$ – 15% $H_2$ plasma and a longer 100 mm spray distance produce a cooler, more diffuse jet. Its droplets have more time to cool or evaporate before impact, so Dataset B coatings retain larger pores. Mechanistically, short $\Delta t_{rep}$ acts like a very high local feed rate. Thus, material is piled on before cooling, virtually overwhelming the classical shadow growth.

In summary, both Dataset A and Dataset B exhibit the same $\Delta t_{rep}$-driven behaviour: shorter interpass times impose a higher thermal load that deepens columnar segmentation, and longer inter-pass times enhance cooling and sintering to fill in the microstructure. Therefore, the time interval between torch passes strongly dictates the SPS coating architecture. Fine temporal resolution (small $\Delta t_{rep}$) preserves the discrete droplet-by-droplet growth needed for classic columnar, porous microstructures. A shorter $\Delta t_{rep}$ of a few hundreds of μs yields fine, well separated columns and high inter-column porosity,

as each particle impact and "shadowing" event is captured. Conversely, a coarse temporal resolution (large $\Delta t_{rep}$) aggregates many splats into quasi-simultaneous deposits, effectively averaging the process. This suppresses the shadowing mechanism and promotes column coalescence: lateral bridging increases and relatively fewer pores remain.

Recommendations

- *Use fine-to-moderate* $\Delta t_{rep}$: A representative time step on the order of a few hundred microseconds is advised. For instance, $\Delta t_{rep} \approx 400$ µs maintains the distinct columnar segmentation in both datasets, preserving most microstructural detail.
- *Tailor* $\Delta t_{rep}$ *to spray regime*: Under Dataset A–like conditions (100 kW, Ar–$H_2$, 75 mm SOD), smaller $\Delta t_{rep}$ values should be used. Coarser steps could lose critical features. Dataset B–like milder conditions can tolerate somewhat larger $\Delta t_{rep}$ before accuracy suffers.
- *Balance accuracy and cost*: Larger $\Delta t_{rep}$ dramatically cuts computation (e.g. 800 µs steps use approximately four times fewer iterations than 200 µs), but the last gains come at steep fidelity loss. Aim for the smallest $\Delta t_{rep}$ that is still computationally feasible.

Finally, $\Delta t_{rep}$ must be chosen judiciously to capture key SPS phenomena. By aligning $\Delta t_{rep}$ with the spray parameters, one can reliably simulate the balance between density, and columnarity.

# Chapter 5: **CONCLUSION AND FUTURE SCOPE OF WORK**

The model developed by Ashtiani BK (2020) studied radial injection, assuming two different models, namely frozen, and flattened models, as illustrated in section 1.5. However, as they point out on pg. 64 (Ashtiani 2020), a comprehensive study could not be conducted, owing to a lack of diversity in CFD results.

The present study overcomes these limitations by making splat formation a function of particle temperature, effectively integrating both frozen, and flattened models into one. It examines the effects of four key process parameters, namely (i) interpeak distances between substrate asperities, (ii) particle distributions, (iii) spray gun velocity, and (iv) database representative times, thereby advising on ways to optimise the microstructural characteristics of SPS coating buildup.

Further, the current study contrasts two different CFD datasets of numerical simulations of the Mettech Axial III torch in ANSYS Fluent: a stronger, hotter, higher-enthalpy, Hydrogen-rich plume with a shorter stand-off distance, versus a weaker, cooler, lower-energy Nitrogen-diluted plume with a longer stand-off distance. Tecplot was used to generate the plots.

However, it is important to note that even this refined version of the previous model makes certain assumptions, which could be resolved in future iterations. First, the particles are assumed to follow straight-line trajectories from 100 microns above the substrate to its surface, thereby neglecting rebound effects. Second, the substrate itself is considered a tiny square of 600X600 $\mu m^2$. Third, the splat scale is treated geometrically — no thermal or fluid-based deformation models are used. Therefore, to improve the model, future iterations could focus on:

1. Making the particle trajectories a function of the mass of droplets, with lighter particles deflecting more readily, while heavier ones traversing straight lines;
2. Employing a Random function to randomly neglect a portion of the particles to simulate the effects of splashing, and rebounding;
3. Increasing the substrate area to a few thousand more square micrometres, say 1000X1000 $\mu m^2$;
4. Using heat transfer equations to calculate, and subsequently update the substrate temperature to simulate heat dissipation, and thermal losses. The results from database representative time already hold promise in direction of the same.

Moreover, like the previous ones, the current version also exaggerates the effects of shadowing, thus overestimating porosity. This may have to do with the fact that the model assumes the breaking down of droplets in shape of kites made up of smaller spheres to simulate the formation of splats. Thus, to address the exaggeration of shadow effects, and the overestimation of porosity, a new model of the splat formation needs to be developed. This work has shown that the current model is able to qualitatively capture some of the features of the coating build-up, but its accuracy is not yet sufficient to quantitatively study the effect of the operating parameters on the coating. An improved splat formation model should be able to offer this capability.

# Chapter 6: **BIBLIOGRAPHY**


1. Ahmady AR, Ekhlasi A, Nouri A, Nazarpak MH, Gong P, Solouk A (2023) High entropy alloy coatings for biomedical applications: a review. Smart Mater Manuf 1:100009.
   DOI: 10.1016/j.smmf.2022.100009
2. Al-Turaif H, Bousfield DW (2004) The influence of substrate absorbency on coating surface energy. Prog Org Coatings 49(1):62–68.
   DOI: 10.1016/j.porgcoat.2003.08.008
3. Alkathafi M, Younis A (2022) Electric arc thermal spray process using Zn coating for stainless steel thin wires. J Mater Sci Eng 10:2021.
   DOI: 10.4172/2169-0022.1000627
4. Arabgol Z, Vidaller MV, Assadi H, Gärtner F, Klassen T (2017) Influence of thermal properties and temperature of substrate on the quality of cold-sprayed deposits. Acta Mater 127:287–301.
   DOI: 10.1016/j.actamat.2017.01.040
5. Arboleda JA, Serna CM, Cadavid E, Barrios AC, Vargas F, Toro A (2018) Effect of flame spray deposition parameters on the microstructure of Al2O3–13%TiO2 coatings applied onto 7075 aluminum alloy. Mater Res 21(5):e20180038.
   DOI: 10.1590/1980-5373-MR-2018-0038
6. Armada S, Schmid R, Johnsen H, Espallargas N (2015) 8—Functionalized thermal spray coatings. In: Espallargas N (ed) Future development of thermal spray coatings. Woodhead Publishing, pp 207–228.
   DOI: 10.1016/B978-0-85709-769-9.00008-7
7. Ashokkumar M, Thirumalaikumarasamy D, Sonar T, Deepak S, Vignesh P, Anbarasu M (2022a) An overview of cold spray coating in additive manufacturing, component repairing and other engineering applications. J Mech Behav Mater 31(1):514–534.
   DOI: 10.1515/jmbm-2022-0056
8. Ashokkumar M, Thirumalaikumarasamy D, Sonar T, Deepak S, Vignesh P, Anbarasu M (2022b) Development of sustainable cold spray coatings and 3D additive manufacturing components for repair/manufacturing applications: a critical review. J Mech Behav Mater 31(1):514–534.
   DOI: 10.1515/jmbm-2022-0056
9. Ashtiani BK (2020) Development of a three-dimensional suspension plasma spray coating build-up model.

MASc Thesis
10. Azar SG (2018) Three-dimensional simulation of coating build-up in suspension plasma spray process
PhD Thesis, p. 3
11. Babu A, Dzhurinskiy D, Dautov S, Shornikov P (2023) Structure and electrochemical behavior of atmospheric plasma sprayed $Cr_3C_2$-NiCr cermet composite coatings. Int J Refract Metals Hard Mater 111:106105.
DOI: 10.1016/j.ijrmhm.2023.106105
12. Bai Y, Zhou S-J, Shi L, Ma W, Liu C-W (2018) Fabrication and characterization of suspension plasma-sprayed fluoridated hydroxyapatite coatings for biomedical applications. J Therm Spray Tech 27:1322–1332.
DOI: 10.1007/s11666-018-0747-6
13. Bar-Hen M, Etsion I (2017) Experimental study of the effect of coating thickness and substrate roughness on tool wear during turning. Tribol Int 110:341–347.
DOI: 10.1016/j.triboint.2016.11.011
14. Basak AK, Kurdi A, Radhika N, Arputharaj J, Prakash C, Pramanik A, Shankar S (2024a) Compressive mechanical properties of thermal sprayed AlCoCrFeNi high entropy alloy coating. J Alloys Compd 1003:175721.
DOI: 10.1016/j.jallcom.2024.175721
15. Basak AK, Radhika N, Prakash C, Pramanik A (2024b) Investigation on the microstructure and micro-mechanical properties of thermal-sprayed NiCoCrAlY high entropy alloy coating. Designs (Basel) 8(2):37.
DOI: 10.3390/designs8020037
16. Bensebaa F (2013) Chapter 4—Nanoparticle assembling and system integration. In: vol. 19, Bensebaa F (ed) Nanoparticle technologies, Interface science and technology, vol 19. Elsevier, pp 185–277.
DOI: 10.1016/B978-0-12-369550-5.00004-5
17. Bobzin K, Wietheger W, Knoch MA (2021) Development of thermal spray processes for depositing coatings on thermoplastics. J Therm Spray Technol 30(1):157–167.
DOI: 10.1007/s11666-020-01147-x
18. Boulos MI, Fauchais P, Heberlein JVR (2021) Thermal Spray Fundamentals: From Powder to Part.
DOI: 10.1007/978-3-030-70672-2
19. Brossard S (2010) Microstructural analysis of thermal spray coatings by electron microscopy.

PhD Thesis, p 376
20. Champagne VK Jr, Helfritch D, Leyman P, Grendahl S, Klotz B (2005) Interface material mixing formed by the deposition of copper on aluminum by means of the cold spray process. J Therm Spray Tech 14:330–334.
DOI: 10.1361/105996305X59332
21. Chen Q-Y, Peng X-Z, Yang G-J, Li C-X, Li C-J (2015) Characterization of plasma jet in plasma spray-physical vapor deposition of YSZ using a <80 kW shrouded torch based on optical emission spectroscopy. J Therm Spray Technol 24(6):1038–1045.
DOI: 10.1007/s11666-015-0248-9
22. Curry N, Leitner M, Körner K (2020) High-porosity thermal barrier coatings from high-power plasma spray equipment—processing, performance and economics. Coatings 10(10):957.
DOI: 10.3390/coatings10100957
23. Czupryński A (2019) Flame spraying of aluminum coatings reinforced with particles of carbonaceous materials as an alternative for laser cladding technologies. Materials 12(21).
DOI: 10.3390/ma12213467
24. DebRoy T, Wei HL, Zuback JS, Mukherjee T, Elmer JW, Milewski JO, Beese AM, Wilson-Heid A, De A, Zhang W (2018) Additive manufacturing of metallic components—process, structure and properties. Prog Mater Sci 92:112–224.
DOI: 10.1016/j.pmatsci.2017.10.001
25. Della Gatta R, Perna AS, Viscusi A, Pasquino G, Astarita A (2022) Cold spray deposition of metallic coatings on polymers: a review. J Mater Sci 57(1):27–57.
DOI: 10.1007/s10853-021-06561-2
26. DePalma K, Walluk M, Martin LP, Sisak K (2022) Investigation of mechanical properties of twin wire arc repair of cast iron components. J Therm Spray Technol 31(1):315–328.
DOI: 10.1007/s11666-021-01304-w
27. Dorfman MR (2018) Chapter 22—Thermal spray coatings. In: Kutz M (ed) Handbook of environmental degradation of materials. William Andrew Publishing, pp 469–488.
DOI: 10.1016/B978-0-323-52472-8.00023-X
28. Dorfman MR (2005) Chapter 20—Thermal spray coatings. In: Kutz M (ed) Handbook of environmental degradation of materials. William Andrew Publishing, Norwich, NY, pp 405–422.
DOI: 10.1016/B978-081551500-5.50022-7

29. Du Q, M'Hamdi M, Reiersen M, Hovig EW, Zhang K (2024) A fully kinetic phase diagram-coupled multicomponent columnar-to-equiaxed grain transition model with an application to additive manufacturing. Calphad 84:102642.
DOI: 10.1016/j.calphad.2023.102642
30. Dykhuizen RC, Smith MF (1998) Gas dynamic principles of cold spray. J Therm Spray Technol 7(2):205–212.
DOI: 10.1361/105996398770350945
31. Elewa RE, Afolalu SA, Fayomi OSI (2019) Protective impact of molten zinc coating sheets in contaminated environment-review. J Phys Conf Ser 1378(2).
DOI: 10.1088/1742-6596/1378/2/022071.
32. Elshalakany AB, Osman TA, Hoziefa W, Escuder AV, Amigó V (2019) Comparative study between high-velocity oxygen fuel and flame spraying using MCrAlY coats on a 304 stainless steel substrate. J Market Res 8(5):4253–4263.
DOI: 10.1016/j.jmrt.2019.07.035
33. Espallargas N (2015) 1—Introduction to thermal spray coatings. In: Espallargas N (ed) Future development of thermal spray coatings. Woodhead Publishing, pp 1–13.
DOI: 10.1016/B978-0-85709-769-9.00001-4
34. Fauchais P (2015) 2—Current status and future directions of thermal spray coatings and techniques. In: Espallargas N (ed) Future development of thermal spray coatings. Woodhead Publishing, pp 17–49.
DOI: 10.1016/B978-0-85709-769-9.00002-6
35. Fauchais P, Heberlein JVR, Boulos MI (2013) D.C. Plasma Spraying. Thermal spray fundamentals: from powder to part, 383–477.
DOI: 10.1007/978-0-387-68991-3_7
36. Fauchais P, Vardelle A (2012) Thermal sprayed coatings used against corrosion and corrosive wear. In: Advanced plasma spray applications, vol 1. InTech.
DOI: 10.5772/34448
37. Fauchais P, Montavon G, Bertrand G (2010) From powders to thermally sprayed coatings. J Therm Spray Technol 19(1):56–80.
DOI: 10.1007/s11666-009-9435-x
38. Fauchais P, Vardelle A (2007) Thermal spray coatings.
DOI: 10.1002/047134608X.W5923.pub2
39. Fauchais P (2004) Understanding plasma spraying. In: Journal of Physics D: Applied Physics 37(9):86-108.
DOI: 10.1088/0022-3727/37/9/R02

40. Fauchais P, Vardelle M (2003) How to improve the reliability and reproducibility of plasma sprayed coatings. In: Proceedings of Thermal Spray: Advancing the Science and Applying the Technology, Orlando, Florida
DOI: 10.31399/asm.cp.itsc2003p1165
41. Feuerstein A, Knapp J, Taylor T, Ashary A, Bolcavage A, Hitchman N (2008) Technical and economical aspects of current thermal barrier coating systems for gas turbine engines by thermal spray and EBPVD: a review. J Therm Spray Technol 17:199–213.
DOI: 10.1007/s11666-007-9148-y
42. Fu W, Chen Q-Y, Yang C, Yi D-L, Yao H-L, Wang H-T, Ji G-C, Wang F (2020) Microstructure and properties of high velocity oxygen fuel sprayed (WC-Co)-Ni coatings. Ceram Int 46(10, Part A):14940–14948.
DOI: 10.1016/j.ceramint.2020.03.021
43. Ganvir A, Curry N, Markocsan N, Nylén P, Toma F-L (2014) Comparative study of suspension plasma sprayed and suspension high velocity oxy-fuel sprayed YSZ thermal barrier coatings. Surface and Coatings Technology 268:70–76.
DOI: 10.1016/j.surfcoat.2014.11.054
44. Gaur A, Pandel U, Sharma S (2023) A study of investigating the effects of variables and assessing the efficiency of air plasma spray as a coating technique. Mater Today Proc.
DOI: 10.1016/j.matpr.2023.11.096
45. Gedzevicius I, Valiulis AV (2006) Analysis of wire arc spraying process variables on coatings properties. J Mater Process Technol 175(1):206–211.
DOI: 10.1016/j.jmatprotec.2005.04.019
46. Ghosh D (2020) A review of multi-material additive manufacturing and application to hypersonic and re-entry vehicle heat shielding.
DOI: 10.13140/RG.2.2.25111.39842
47. Gildersleeve EJ, Vaßen R (2023) Thermally sprayed functional coatings and multilayers: a selection of historical applications and potential pathways for future innovation. J Therm Spray Technol.
DOI: 10.1007/s11666-023-01587-1
48. Habib KA, Cano DL, Alvaro JAH, Serrano-Mira J, Llopis R, Moreno DL, Mohammed SS (2022) Effects of thermal spraying technique on the remelting behavior of NiCrBSi coatings. Surf Coatings Technol 444:128669.
DOI: 10.1016/j.surfcoat.2022.128669

49. Hardwicke CU, Lau Y-C (2013) Advances in thermal spray coatings for gas turbines and energy generation: a review. J Therm Spray Technol 22(5):564–576. DOI: 10.1007/s11666-013-9904-0
50. Hashmi AW, Mali HS, Meena A, Saxena KK, Ahmad S, Agrawal MK, Sagbas B, Puerta APV, Khan MI (2023) A comprehensive review on surface post-treatments for freeform surfaces of bio-implants. J Market Res 23:4866–4908. DOI: 10.1016/j.jmrt.2023.02.007
51. Hauer M, Banaschik R, Kroemmer W, Henkel K-M (2019) Variation of heat input and its influence on residual stresses and coating properties in arc spraying with different gas mixtures. J Therm Spray Technol 28(1):40–52. DOI: 10.1007/s11666-018-0806-z
52. Holmberg K, Matthews ABTTS (1994) Chapter 4 Tribological properties of coatings. In: Coatings tribology, vol 28. Elsevier. DOI: 10.1016/S0167-8922(08)70754-5
53. Horiuchi S, Terasaki N, Miyamae T (2024) Introduction—interfaces in adhesion and adhesive bonding. In: Horiuchi S, Terasaki N, Miyamae T (eds) Interfacial phenomena in adhesion and adhesive bonding. Springer Nature Singapore, Singapore, pp 1–15. DOI: 10.1007/978-981-99-4456-9_1
54. Horner AL, Hall AC, McCloskey JF (2015) The effect of process parameters on twin wire arc spray pattern shape. Coatings 5(2):115–123. DOI: 10.3390/coatings5020115
55. Hu H, Mao L, Xiao J, Sun G, Liao H, Zhang C (2023) Effect of hydrogen flow rate on microstructure and tribological properties of plasma-sprayed $Cr_2O_3$-65%TiO2 composite coatings. Tribol Int 189:108939. DOI: 10.1016/j.triboint.2023.108939
56. Hui R, Wang Z, Kesler O, Rose L, Jankovic J, Yick S, Maric R, Ghosh D (2007) Thermal plasma spraying for SOFCs: Applications, potential advantages, and challenges. Tribol Int 189:108939. DOI: 10.1016/j.jpowsour.2007.03.075
57. Irissou E, Poirier D, Vo P, Cojocaru CV, Aghasibeig M, Yue S (2022) How to unleash the remarkable potential of cold spray: a perspective. J Therm Spray Technol 31(4):908–919. DOI: 10.1007/s11666-022-01363-7

58. Jadidi M, Moghtadernejad S, Dolatabadi A (2015) A comprehensive review on fluid dynamics and transport of suspension/liquid droplets and particles in High-Velocity Oxygen-Fuel (HVOF) thermal spray. Coatings 5(4):576-645.
DOI: 10.3390/coatings5040576
59. Janisson JS, Meillot E, Vardelle A, Coudert J-F, Pateyron B, and Fauchais P (1998) Plasma spraying using Ar-He-$H_2$ gas mixtures. In: Proceedings of the 15th International Thermal Spray Conference, Nice, France.
DOI: 10.31399/asm.cp.itsc1998p0803
60. Jiang J, Hou W, Feng X, Shen Y (2023) Microstructure and properties of Cr–$AlSi_{12}$ composite coatings pre-coated on Ti–6Al–4V alloy substrate via mechanical alloying and subsequent laser cladding treatment. Mater Chem Phys 305:127928.
DOI: 10.1016/j.matchemphys.2023.127928
61. Jose SA, John M, Menezes PL (2022) Cermet systems: synthesis, properties, and applications. Ceramics 5(2):210-236.
DOI: 10.3390/ceramics5020018
62. Kant S, Kumar M, Chawla V, Singh S (2020) Study of high temperature oxidation behaviour of wire arc sprayed coatings. Mater Today Proc 21:1741–1748.
DOI: 10.1016/j.matpr.2020.01.226
63. Karthikeyan J (2007) 4—The advantages and disadvantages of the cold spray coating process. In: Champagne et al (ed) Woodhead publishing series in metals and surface engineering. Woodhead Publishing, pp 62–71.
DOI: 10.1533/9781845693787.1.62
64. Kassner H, Siegert R, Hathiramani D, Vassen R, Stoever D (2007) Application of suspension plasma spraying (SPS) for manufacture of ceramic coatings. J Therm Spray Technol 17(1):115–123.
DOI: 10.1007/s11666-007-9144-2
65. Kim D-Y, Park J-J, Lee J-G, Kim D, Tark SJ, Ahn S, Yun JH, Gwak J, Yoon KH, Chandra S, Yoon SS (2013) Cold spray deposition of copper electrodes on silicon and glass substrates. J Therm Spray Technol 22(7):1092–1102.
DOI: 10.1007/s11666-013-9953-4
66. Klinkov SV, Kosarev VF, Shikalov VS (2019) Influence of nozzle velocity and powder feed rate on the coating mass and deposition efficiency in cold spraying. Surf Coatings Technol 367:231–243.
DOI: 10.1016/j.surfcoat.2019.04.004

67. Kumar K, Kumar S, Gill HS (2023) Role of surface modification techniques to prevent failure of components subjected to the fireside of boilers. J Fail Anal Prev 23(1):1–15. DOI: 10.1007/s11668-022-01556-w
68. Kumar S (2022) Influence of processing conditions on the mechanical, tribological and fatigue performance of cold spray coating: a review. Surf Eng 38:1–42. DOI: 10.1080/02670844.2022.2073424
69. Kumar S, Kumar R (2021) Influence of processing conditions on the properties of thermal sprayed coating: a review. Surf Eng 37(11):1339–1372. DOI: 10.1080/02670844.2021.1967024
70. Kumar R, Kumar S (2018) Thermal spray coating: a study. Int J Eng Sci Res Technol 7(3). https:// doi.org/10.5281/zenodo.1207005
71. Lal D, Sampath S (2023) Offset bending for interfacial toughness of plasma sprayed ceramic coatings. Surf Coat Technol 469:129786. DOI: 10.1016/j.surfcoat.2023.129786
72. Li C-J, Luo X-T, Dong X-Y, Zhang L, Li C-X (2022) Recent research advances in plasma spraying of bulk-like dense metal coatings with metallurgically bonded lamellae. J Therm Spray Technol 31(1):5–27. DOI: 10.1007/s11666-022-01327-x
73. Li H, Qian X, Xu C, Huang S, Zhu C, Jiang X, Shao L, Hou L (2017) Hierarchical porous $Co_9S_8$/nitrogen-doped carbon@$MoS_2$ polyhedrons as pH universal electrocatalysts for highly efficient hydrogen evolution reaction. ACS Appl Mater Interfaces 9(34):28394–28405. DOI: 10.1021/acsami.7b06384
74. Li W-Y, Zhang C, Guo XP, Zhang G, Liao HL, Li C-J, Coddet C (2008) Effect of standoff distance on coating deposition characteristics in cold spraying. Materials & Design 29(2):297–304. DOI: 10.1016/j.matdes.2007.02.005
75. Li C-J, Li W-Y, Liao H (2006) Examination of the critical velocity for deposition of particles in cold spraying. J Therm Spray Technol 15(2):212–222. DOI: 10.1361/105996306X108093
76. Liao C-J, Lin F-H, Chen K-S, Sun J-S (1999) Thermal decomposition and reconstitution of hydroxyapatite in air atmosphere. Biomaterials 20(19):1807–1813. DOI: 10.1016/S0142-9612(99)00076-9

77. Lima RS, Marple BR (2005) Superior performance of high-velocity oxyfuel-sprayed nanostructured TiO2 in comparison to air plasma-sprayed conventional $Al_2O_3$-13$TiO_2$. J Therm Spray Technol 14(3):397–404.
DOI: 10.1361/105996305X59413
78. Majumdar JD (2015) Thermal and cold spraying technology in manufacturing. In: Nee AYC (ed) Handbook of manufacturing engineering and technology. Springer London, London, pp 2805– 2850.
DOI: 10.1007/978-1-4471-4670-4_31
79. Ma X, Ruggiero P (2018) Practical aspects of suspension plasma spray for thermal barrier coatings on potential gas turbine components. J Therm Spray Technol 27(4):591–602.
DOI: 10.1007/s11666-018-0700-8
80. Martin J, Maizeray A, Tousch CDS, Marcos G, Czerwiec T, Henrion G (2023) A new strategy to prepare alumina-zirconia composite or multilayered coatings by combining cold-spray deposition and plasma electrolytic oxidation. Mater Today Commun 36:106676.
DOI: 10.1016/j.mtcomm.2023.106676
81. Mauer G, Moreau C (2022) Process diagnostics and control in thermal spray. J Therm Spray Technol 31(4):818–828.
DOI: 10.1007/s11666-022-01341-z
82. Meeß J, Anasenzl M, Ossenbrink R, Michailov V (2022) Influence of particle velocities on adhesion strength of cold spray inner diameter coatings. J Therm Spray Technol 31(7):2025–2038.
DOI: 10.1007/s11666-022-01439-4
83. Mehta A, Vasudev H, Thakur L (2024) Applications of numerical modelling techniques in thermal spray coatings: a comprehensive review. Int J Interact des Manuf 18(6):3525–3545.
DOI: 10.1007/s12008-023-01511-5
84. Menasri N, Zergane S, Aimeur N, Saci A (2022) Experimental investigation on the coating of nickel-base super alloy using wire flame spraying. Acta Univ Sapientiae, Electr Mech Eng 14(1):28–39.
DOI: 10.2478/auseme-2022-0003
85. Meyer PJ, Hawley D (1991) LPPS production systems. In: Proceedings of 4th National Thermal Spray Conference, Pittsburgh, Pennsylvania.

86. Narayanan TSNS, Kim J, Jeong HE, Park HW (2020) Enhancement of the surface properties of selective laser melted maraging steel by large pulsed electron-beam irradiation. Addit Manuf 33:101125.
DOI: 10.1016/j.addma.2020.101125
87. Neo RG, Wu K, Tan SC, Zhou W (2022) Effect of spray distance and powder feed rate on particle velocity in cold spray processes. Metals 12(1):75.
DOI: 10.3390/met12010075
88. Nikam S, Wu H, Harkin R, Quinn J, Lupoi R, Yin S, McFadden S (2022) On the application of the anisotropic enhanced thermal conductivity approach to thermal modelling of laser-based powder bed fusion processes. Addit Manuf 55:102870.
DOI: 10.1016/j.addma.2022.102870
89. Nurisna Z, Anggoro S, Mujtahid HN (2022) Physical and mechanical properties of twin-wire arc spray and wire flame spray coating on carbon steel surface. In: Broad exposure to science and technology II, Materials Science Forum, vol 1057. Trans Tech Publications Ltd, pp 235–239.
DOI: 10.4028/p-z698i0
90. Odhiambo JG, Li W, Zhao Y, Li C (2019) Porosity and its significance in plasma-sprayed coatings. Coatings 9(7).
DOI: 10.3390/coatings9070460
91. Oksa M, Turunen E, Suhonen T, Varis T, Hannula S-P (2011) Optimization and characterization of high velocity oxy-fuel sprayed coatings: techniques, materials, and applications. Coatings 1(1):17-52.
DOI: 10.3390/coatings1010017
92. Panchal H, Amin S (2016) A review on thermal spray coating processes. Int J Curr Trends Eng Res (IJCTER) 2:556–563.
93. Pathanatecha W (2019) A study of various parameters affecting adhesion of coatings to metal substrates.
94. Phiri RR, Oladijo OP, Maledi N, Akinlabi ET (2018) Effect of coating thickness on wear performance of inconel 625 coating. IOP Conf Ser Mater Sci Eng 423(1).
DOI: 10.1088/1757-899X/423/1/012159
95. Pourang K, Moreau C, Dolatabadi A (2016) Effect of substrate and its shape on in-flight particle characteristics in suspension plasma spraying. J Therm Spray Tech 25:44–54.
DOI: 10.1007/s11666-015-0342-z

96. Poza P, Garrido-Maneiro MÁ (2022) Cold-sprayed coatings: Microstructure, mechanical properties, and wear behaviour. Prog Mater Sci 123:100839. DOI: 10.1016/j.pmatsci.2021.100839
97. Remesh K, Ng HW, Yu SCM (2003) Influence of process parameters on the deposition footprint in plasma-spray coating. J Therm Spray Technol 12(3):377–392. DOI: 10.1361/105996303770348258
98. Rodriguez RMHP, Paredes RSC, Wido SH, Calixto A (2007) Comparison of aluminium coatings deposited by flame spray and by electric arc spray. Surf Coat Technol 202(1):172–179. DOI: 10.1016/j.surfcoat.2007.05.067
99. Saharkhiz R, Valefi Z, Mirjani M, Mirak A (2023) Comprehensive study on the effect of HVOF processing parameters and particle size on high-temperature properties of NiCoCrAlYTa coatings. Surf Coat Technol 473:129951. DOI: 10.1016/j.surfcoat.2023.129951
100. Saito H, Suzuki T, Fujino T, Suzuki M (2018) Numerical Simulation of Suspension Plasma Spraying with Axial Injection. Materials Transactions 59(11):1791-1797. DOI: 10.2320/matertrans.T-M2018842
101. Salama HE, Aziz MSA, Alsehli M (2019) Carboxymethyl cellulose/sodium alginate/chitosan biguanidine hydrochloride ternary system for edible coatings. Int J Biol Macromol 139:614–620. DOI: 10.1016/j.ijbiomac.2019.08.008
102. Sankaran S (2015) Preparation and characterization of lanthanum zirconate by atmospheric plasma spray coatings.
103. Satish C, Kumar KV, Prasad S, Kiran PS, Rahman OSA, Singh P, Indupuri S, Shrivastava R, Pandey SM, Keshri AK (2023) Effect of $Al_2O_3$ and $MoS_2$ reinforcement on microstructure, mechanical, and wear properties of plasma sprayed aluminium hybrid composite coating. Mater Today Commun 36:106640. DOI: 10.1016/j.mtcomm.2023.106640
104. Schmidt T, Assadi H, Gärtner F, Richter H, Stoltenhoff T, Kreye H, Klassen T (2009) From particle acceleration to impact and bonding in cold spraying. J Therm Spray Technol 18(5):794–808. DOI: 10.1007/s11666-009-9357-7
105. Schmidt T, Gaertner F, Kreye H (2006) New developments in cold spray based on higher gas and particle temperatures. J Therm Spray Technol 15(4):488–494. DOI: 10.1361/105996306X147144

106. Seiji Kuroda Jin Kawakita MW, Katanoda H (2008) Warm spraying—a novel coating process based on high-velocity impact of solid particles. Sci Technol Adv Mater 9(3):33002.
DOI: 10.1088/1468-6996/9/3/033002
107. Sharma A, Vijendra B, Ito K, Kohama K, Ramji M, Sai B (2017a) A new process for design and manufacture of tailor-made functionally graded composites through friction stir additive manufacturing. J Manuf Process 26.
DOI: 10.1016/j.jmapro.2017.02.007
108. Singh S, Kumar S, Prakash C, Khanna V (2025) Thermal Spray Coatings: Fundamentals and Applications. In: Advanced Structured Materials, vol 232.
DOI: 10.1007/978-981-96-3472-9
109. Singh H, Ang A, Matthews S (2019) Thermal Spray for Extreme Environments. J Therm Spray Tech 28:1339–1345.
DOI: 10.1007/s11666-019-00929-2
110. Song Z, Li H (2022) Plasma spraying with wire feeding: a facile route to enhance the coating-substrate interfacial metallurgical bonding. Coatings 12(5).
DOI: 10.3390/coatings12050615
111. Su J, Zhou W, Wang H, Liu Y, Qing Y, Luo F, Zhu D, Zhou L (2016) Effect of critical plasma spray parameters on microstructure and microwave absorption property of $Ti_3SiC_2$/cordierite coatings. J Therm Spray Technol 25(4):639–649.
DOI: 10.1007/s11666-016-0401-0
112. Tejero-Martin D, Rezvani Rad M, McDonald A, Hussain T (2019) Beyond traditional coatings: a review on thermal-sprayed functional and smart coatings. J Therm Spray Technol 28(4):598– 644.
DOI: 10.1007/s11666-019-00857-1
113. Tillmann W, Vogli E, Baumann I, Matthaeus G, Ostrowski T (2008) Influence of the HVOF gas composition on the thermal spraying of WC-Co submicron powders (−8 + 1 μm) to produce superfine structured cermet coatings. J Therm Spray Technol 17(5):924–932.
DOI: 10.1007/s11666-008-9234-9
114. Vignesh S, Shanmugam K, Balasubramanian V, Sridhar K (2017) Identifying the optimal HVOF spray parameters to attain minimum porosity and maximum hardness in iron based amorphous metallic coatings. Def Technol 13.
DOI: 10.1016/j.dt.2017.03.001

115. Villafuerte J (2011) In: Czerwinski F (ed) Corrosion protection of magnesium by cold spray, Chap 9. IntechOpen, Rijeka.
DOI: 10.5772/13985
116. Viswanathan V, Katiyar NK, Goel G, Matthews A, Goel S (2021) Role of thermal spray in combating climate change. Emergent Mater 4(6):1515–1529.
DOI: 10.1007/s42247-021-00307-1
117. Voisey K (2010) Sprayed coatings. In: Shreir's corrosion.
DOI: 10.1016/B978-044452787-5.00139-6
118. Warcaba M, Kowalski K, Kopia A, Moskalewicz T (2021) Impact of surface topography, chemistry and properties on the adhesion of sodium alginate coatings electrophoretically deposited on titanium biomaterials. Metall Mater Trans A 52(10):4454–4467.
DOI: 10.1007/s11661-021-06397-0
119. Wentz (2009) Thermal spray process variability and methods of control
120. Xue M, Chen X, Ji X, Xie X, Chao Q, Fan G (2023) Effect of particle size distribution on the printing quality and tensile properties of Ti-6Al-4V alloy produced by LPBF process. Metals 13(3):604.
DOI: 10.3390/met13030604
121. Yang X, Jia J, Chen W, Yang G, Xin H, He N, Ma S (2022) Corrosive wear behaviour of HVOF-sprayed micro-nanostructured $Cr_3C_2$–NiCr cermet coatings under aqueous media. Ceram Int 48(11):15144–15151.
DOI: 10.1016/j.ceramint.2022.02.044
122. Yuan P, Zhang M, Wang X, Qi Y, Wang T, Zhao L, Cui C (2023) Effects of polylactic acid coating on properties of porous Zn scaffolds as degradable materials. Mater Charact 199:112852.
DOI: 10.1016/j.matchar.2023.112852
123. Zhang L, Liao X-J, Zhang S-L, Luo X-T, Li C-J (2021) Effect of powder particle size and spray parameters on the Ni/Al reaction during plasma spraying of Ni-Al composite powders. J Therm Spray Technol 30(1):181–195.
DOI: 10.1007/s11666-020-01150-2
124. Zhao X, Li C, Jiang H, Li S, Han X (2023) Mechanistic study on the influence of hydrogen fuel in high-velocity oxygen-fuel (HVOF) thermal spraying process. JOM.
DOI: 10.1007/s11837-023-06254-y
125. Zhou D, Vassen R (2023) 7—Thermal barrier coatings manufactured by suspension and solution precursor plasma spray—state of the art and recent progress. In: Guo H

(ed) Thermal barrier coatings, 2nd ed, Series in metals and surface engineering. Woodhead Publishing, pp 199–228.
DOI: 10.1016/B978-0-12-819027-2.00011-0

126. Zhu Q, Chua MH, Ong PJ, Lee JJC, Chin KLO, Wang S, Kai D, Ji R, Kong J, Dong Z, Xu J, Loh XJ (2022) Recent advances in nanotechnology-based functional coatings for the built environment. Mater Today Adv 15:100270.
DOI: 10.1016/j.mtadv.2022.100270